Two approaches for a simpler STED microscope using a dual-color laser or a single wavelength

Ancuţa Teodora Şcheul

UNIVERSITÉ DE GRENOBLE

THÈSE

Pour obtenir le grade de

DOCTEUR DE L'UNIVERSITÉ DE GRENOBLE

Spécialité : **Optique, Nanophysique**

Arrêté ministériel : 7 août 2006

Présentée par

Şcheul Ancuţa Teodora

Thèse dirigée par **Jean-Claude Vial**
et codirigée par **Irène Wang**

préparée au sein **du Laboratoire interdisciplinaire de Physique**
et de **l'Ecole Doctorale de Physique, Grenoble**

Two approaches for a simpler STED microscope using a dual-color laser or a single wavelength

Thèse soutenue publiquement le **22 Novembre 2013**,
devant le jury composé de :

Dominique Bourgeois
Directeur de Recherche CNRS,Institut de Biologie Structurale, Grenoble, Président

Sandrine Lévêque-Fort
Chargée de Recherche CNRS, Université Paris-Sud, Paris, Rapporteur

Mark Neil
Professeur Imperial College, London, Rapporteur

Simion Aştilean
Professeur Université Babeş-Bolyai, Cluj-Napoca, Examinateur

Jean-Claude Vial
Directeur de Recherche CNRS, Laboratoire interdisciplinaire de Physique, Grenoble, Directeur de thèse

Irène Wang
Ingénieur de Recherche CNRS, Laboratoire interdisciplinaire de Physique, Grenoble, Co-Directeur de thèse

Contents

Summary/Résumé

Stimulated emission depletion (STED) is a well-known super-resolution method. In a STED microscope, a doughnut-shaped beam is superimposed with the excitation beam and keeps the fluorophores in the periphery of the excitation spot in a dark state by stimulated emission, thus effectively improving the spatial resolution in a scanning configuration. This technique requires a complex setup since two laser beams, generally from different sources need to be perfectly aligned.
In this work we propose two STED configurations that will simplify the setup and reduce the total cost of such a system. The basic idea in both cases is to use the same laser source for both excitation and stimulated emission depletion.
In the first setup we have developed an original two-color source based on a microchip Nd-YAG laser. This microchip laser simultaneously delivers sub-ns pulses at two wavelengths, 355 nm (excitation) and 532 nm (depletion), which are generated by harmonic conversion from an Nd-YAG laser emission and offer the advantage of being intrinsically aligned and synchronized. Further work consisted in determining suitable dyes for this particular source. We have built a microscope setup based on this laser source and obtained images with an improved resolution. The confirmation of the reduction of the excitation volume is showed by Fluorescence Correlation Spectroscopy (FCS) measurements. However, the performance of this system is limited by chromatic aberrations. The combination of Selective Plane Illumination Microscopy (SPIM) with STED is considered.
In the second setup the chromatic aberrations are no longer a problem since the same wavelength is used for two photon excitation and one photon depletion. By playing on the duration of the pulse (thus the instantaneous intensity), one of these two processes can be favored. Fluorescence was excited by two photon absorption with a femtosecond pulse, then depleted by one photon stimulated emission with a stretched pulse. We used the Time Correlated Single Photon Counting (TCSPC) method to study the depletion efficiency of DCM dye in solution and numerical simulations show that this method can be applied to super-resolved microscopy. In the end we present the preliminary images obtained with a home-built Two-photon Single wavelength STED microscope and the resolution improvement obtained. Further improvements are to be made to the custom microscope.

La microscopie STED (stimulated emission depletion ou déplétion par émission stimulée) est une des méthodes les plus répandues de microscopie de super-résolution. Dans un microscope STED, un faisceau en anneau se superpose avec le faisceau d'excitation et éteint les fluorophores en périphérie du faisceau d'excitation par émission stimulée. Au centre de l'anneau, où le faisceau STED a une intensité nulle, la fluorescence reste intacte. Cette technique nécessite un montage complexe dans lequel deux faisceaux laser, en général issus de deux sources différentes, doivent être parfaitement alignés et superposés.
Dans ce travail de thèse, nous proposons deux configurations STED qui ont pour but de simplifier le montage et de réduire le coût total d'un tel système. L'idée de base dans les deux cas est d'utiliser la même source laser à la fois pour l'excitation et la déplétion par émission stimulée).
Dans la première configuration, nous avons développé une source bicolore originale basée sur un laser Nd-YAG microchip. Ce laser microchip délivre simultanément des impulsions sub-ns à deux longueurs d'onde, 355 nm (excitation) et 532 nm (déplétion), qui sont générés par conversion harmonique à partir d'une émission laser Nd-YAG et offrent l'avantage d'être intrinsèquement alignées et synchronisées. Afin de trouver des colorants appropriés pour cette source particulière, nous avons développé une méthode de caractérisation et testé différents colorants. Nous avons construit un microscope à partir de cette source laser et obtenu des images avec une résolution améliorée. La réduction du volume d'excitation a été confirmée par spectroscopie de corrélation de fluorescence (FCS). Cependant, les aberrations chromatiques des optiques utilisées limitent les performances du montage actuel. Une perspective prometteuse serait de combiner le STED à la microscopie à feuille de lumière (SPIM), plus tolérante des défauts d'achromatisme, et nous montrons les premiers résultats de cette approche.
Dans la seconde configuration, les aberrations chromatiques ne sont plus un problème puisqu' une seule longueur d'onde est utilisée pour l'excitation (par absorption à deux photons) et la déplétion. En jouant sur la durée de l'impulsion (et donc la valeur de l'intensité crête), un de ces deux procédés peut être favorisé. La fluorescence est excitée deux photons par une impulsion femtoseconde, puis est éteinte par émission stimulée à un photon avec une impulsion étirée. Nous avons utilisé une technique résolue en temps (Time-Correlated Single Photon Counting - TCSPC) pour étudier l'efficacité de déplétion du colorant DCM en solution. Les simulations numériques montrent que cette méthode peut être appliquée à la microscopie de super résolution. En fin de cette partie, nous présentons les premiéres images obtenues avec un microscope développé au laboratoire qui permet l'excitation à deux photons et la déplétion à un photon avec une seule longueur d'onde, ainsi que l'amélioration de la résolution observée.
Dans ce travail, nous avons donc mis en place expérimentalement, pour la première fois, deux concepts destinés à simplifier en utilisant deux sources laser originales.

Introduction

Light/optical microscopy, along with electron microscopy, is one of the most powerful microscopy techniques used in life sciences and material science. It is the only microscopy technique that can produce true color images. It is fast, and adaptable to all kinds of sample systems, from gas, to liquid, and to solid sample systems, in any shapes or geometries. It is an important tool in biology and one of its main advantage is that it can image live samples, whereas in the case of electronic microscopy the sample must be completely dry and observed under vacuum, making it impossible to observe living specimens. The main issue with optical microscopy is resolution. Ever since the German physicist Ernst Abbe suggested in 1873 [1] that there was a limit to the resolution achievable from a microscope, it was believed that the wavelength of light placed a practical limit of around 250 nanometres (nm) as the smallest distance between two features in a sample that could be resolved. This is a severe limitation since in biology there are many features of interest below 250 nm in size. As a consequence in the last decade a true revolution in optical microscopy has broken this diffraction limit barrier. The recently developed methods in fluorescence-based light microscopy that have bypassed the resolution limit imposed by diffraction are called super-resolution microscopy techniques.

One of the most known of super-resolution techniques is Stimulated emission depletion (STED) microscopy [2]. It was introduced by S.W Hell and al in 1994 and experimentally proven in 1999 [3]. In a STED microscope, a doughnut-shaped beam is superimposed with the excitation beam and keeps the fluorophores in the periphery of the excitation spot in a dark state by stimulated emission, thus effectively improving the spatial resolution in a scanning configuration. The basic idea of the working principle is relatively simple. Nevertheless, the practical implementation is complex and the cost of the setup is high.

The main purpose of the work presented in this doctoral thesis is to build an original STED setup that could be simpler and have a relatively low cost. The main difference between a confocal laser scanning microscope and a STED microscope is the second laser source which complicates the setup. Therefore, our idea was to use a single laser source for both excitation and stimulated emission depletion. For the practical implementation of this idea we have adopted two paths.

One was to use an original laser source based on a Q-switched Nd-YAG microchip

laser which undergoes harmonic conversion in nonlinear crystals to deliver two wavelengths (355 for excitation and 532 nm for stimulated emission depletion). The two pulses will be intrinsically synchronized and collinear. Basically, the optical setup will be the one of a confocal microscope with the same optical path for both beams. A key element of this configuration will be the beam shaping device conceived to create the doughnut shape on the 532 nm pulse and leave unaffected the 355 nm pulse. In the first part of the thesis we present the steps we made towards building a STED microscope based on this particular laser source. It was a challenge since not only the two wavelengths have a large spectral shift which can cause chromatic aberrations, also one of the wavelengths is in the UV range which is not common in confocal or STED microscopy. Also in the first part we describe the method we used for testing the fluorophores, we discuss the advantages and disadvantages of this particular setup and present the first microscopy results.
In the other approach that we present in the second part of the thesis we propose a configuration in which the same wavelength is used for two-photon excitation and one photon stimulated emission depletion. In our setup a femtosecond (fs) pulse excites the fluorophore by a two-photon process, while the stimulated depletion of the excited state, by means of a one-photon process, is accomplished by a temporally stretched laser pulse. The fs and the stretched pulses come from the same source, a Ti:Sa laser, and are at the same wavelength. This setup combines STED and two-photon excitation (TPE) microscopy and aims at bringing the higher resolution afforded by STED to any TPE microscope without having to add another laser source. We present the optical scheme we have built and experimental results in a dye solution as a proof of principle. The encouraging results obtained with this setup and together with the numerical calculations showed that this concept could be applied to super-resolved microscopy. The last part is dedicated to our work on building the image acquisition setup and the preliminary results we have obtained with it.

Chapter 1

Fluorescence and fluorescence microscopy

1.1 Introduction

Fluorescence is the emission of light by a system that has absorbed light or other electromagnetic radiation. The first observation of fluorescence was made by Bernardino de Sahagún in 1560. Generally the light emitted is at a longer wavelength than the absorbed light. The fluorescent probes are typically called fluorophores or chromophores. Fluorescence has many applications in spectroscopy, microscopy, biological detection and others. In order to better understand fluorescence we need to understand the interaction of the fluorophores with light. Therefore we will start this chapter with an introduction into the photophysics of fluorophores.
We will continue by introducing the fluorescence microscopy technique and its basic functioning principle. Fluorescence microscopy was developed by August Köhler (1866-1948) and Henry Siedentopf at Carl Zeiss AG in Jena and presented to the public on the occasion of a microscopy course at the botanical institute in Vienna in April 1908. Nowadays fluorescence illumination and observation is the most rapidly expanding microscopy technique employed, both in the medical and biological sciences. Recent technological developments have enabled fluorescence microscopy to keep pace with the increasing demands in biological and biomedical sciences. Among these are ultrasensitive cameras, laser illumination, confocal and multi-photon mi-

croscopy, digital image processing, new fluorophores and improvements in optical filters and beamsplitters.
Until now the main issue in fluorescence microscopy has been the attainable resolution, which is limited by diffraction [1]. We make an introduction to this problem and to the new techniques that have been developed to overcome this limit. These so called super-resolution techniques allow the capture of images with a higher resolution than the diffraction limit and allow the visualization of previously inaccessible nano-environments. We will focus on the Stimulated emission (STED) microscopy technique and present the main STED setups.
This chapter is a short insight into the basics of fluorescence and fluorescence microscopy methods.

1.2 Fluorophores

1.2.1 Basic photophysics and photochemistry of fluorophores

A fluorophore is a chemical compound that upon absorption of light emits light at a longer wavelength. The process of fluorescence is usually illustrated by the Jablonski diagram [4]. The Jablonski diagram (1.1) depicts the electronic states of a molecule and the transitions between them. The states are arranged vertically by energy and grouped horizontally by spin multiplicity. The horizontal lines represent eigenstates for that particular molecule. The bold horizontal lines represent the limits of electronic energy states. Within each electronic energy state are multiple vibrational energy levels. These vibrational energy states can include rotational energy levels, which are not usually represented in typical Jablonski diagrams.

In the Jablonski diagram in Fig. 1.1 we can observe the singlet ground state (S_0), in addition to the first (S_1) and second (S_2) excited singlet states. First, the molecule absorbs a photon (in the case of nonlinear absorption, two or more photons) and it is excited to a higher energy level. Only certain photons are absorbed, that is, the photons that have energies that correspond to the energy difference between the ground state and an excited state. Once the molecule is excited to higher energy levels it can relax through different mechanisms that can be divided into two categories: radiative or non-radiative.
The most important non-radiative processes are vibrational relaxation, internal conversion and intersystem crossing. Vibrational relaxation occurs when the energy transferred from the photon to the electron is given away to vibrational modes as

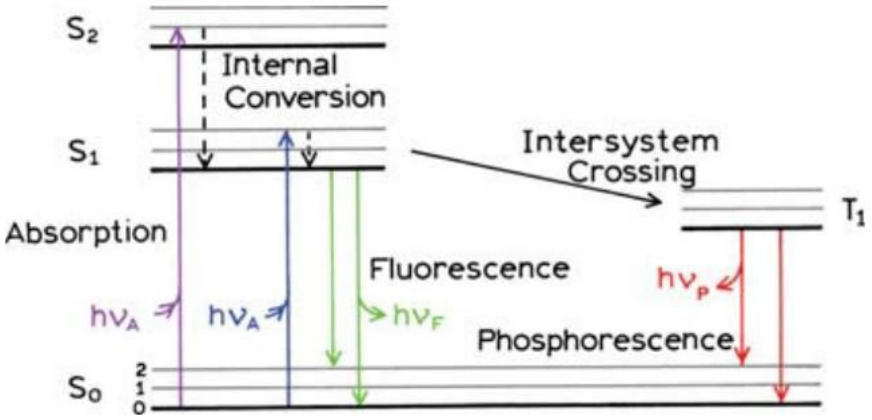

Figure 1.1: Typical Jablonski diagram of a fluorophore. Reproduced from "Principles of Fluorescence Spectroscopy" [5]

kinetic energy. This relaxation occurs between vibrational levels, so electrons will not change from one electronic level to another through this method. Internal conversion occurs if the vibrational levels of different electronic states overlap, and so the excited electron relaxes from a vibrational level in one electronic state to another vibrational level in a lower electronic state. Intersystem crossing is another non-radiative process involving a transition between two electronic states with different spin multiplicity, when an excited electron relaxes to a triplet state and the spin of the excited electron is reversed.
The relaxation of the electron to the ground state from a singlet excited state with the emission of a photon is the radiative process called fluorescence. The energy of the emitted photon matches the difference between the energy levels of the transition. Nevertheless, this energy is smaller than that of the excitation photons due to lost in internal conversion and vibrational relaxation.
The radiative decay from an excited triplet state back to a singlet state is known as phosphorescence.
It is to be noted that the duration of the processes described above determines the probability of the respective event to occur. Thus the faster the transition, the more likely it is to happen. In Table 1.1 are presented the typical duration of radiative and non-radiative processes [6].

There are numerous criteria to classify the types of fluorophores. In [7] they are classified in: organic dyes, biological fluorophores and quantum dots.
Organic dyes can be synthetic or natural. The synthetic dye, fluorescein was among the first dyes to be used in biological applications. Biological fluorophores can be

Transition	Duration (s)	Type
Absorption	10^{-15}	radiative
Vibrational relaxation	10^{-14}-10^{-11}	non-radiative
Internal conversion	10^{-14}-10^{-11}	non-radiative
Intersystem crossing	10^{-8}-10^{-3}	non-radiative
Fluorescence	10^{-9}-10^{-7}	radiative
Phosphorescence	10^{-4}-10^{-1}	radiative

Table 1.1: Timescales for radiative and non-radiative transitions in a molecule

endogenous (fluorescent proteins) and intrinsic (Nicotinamide adenine dinucleotide - NADH, tryptophan). Quantum dots are semiconductor objects of nanometric size (2-50 nm) that fluoresce at a wavelength depending on their size.

1.2.2 Properties of flurophores

Absorption and emission spectra

Electrons surrounding the atomic nucleus are arranged in a series of levels of increasing energy (Fig.1.1). Each element has its own distinct set of energy levels. This arrangement of energy levels is unique for every molecule and gives the molecule its specific properties.

The absorption spectrum represents the fraction of light absorbed by the material over a range of frequencies. As stated before, the absorption of a photon takes place under certain conditions. The absorption that occurs due to a transition between two states is referred to as an absorption line and a spectrum is typically composed of many lines.

In general terms the emission spectrum is the assembly of frequencies of electromagnetic radiation that is emitted when an electron makes a transition from a higher to a lower energy level. The energy of the emitted photon is equal to the energy difference between the two states. The energy differences between the bands in the emission spectrum will be similar to those in the absorption spectrum and frequently the emission spectrum can be approximated by a mirror image of the absorption spectrum.

Stimulated emission

Another type of photon-related electron transitions in an atom is stimulated emission. It is the process by which an excited molecular state interacting with an electromagnetic wave of a certain frequency, may drop to a lower energy level transferring its energy to that field. A photon created in this manner has the same phase,frequency,

polarization, and direction of travel as the photons of the incident wave. The process is identical in form to absorption in which the energy of an absorbed photon causes an identical but opposite transition: from the lower level to a higher energy level.
The absorption and emission (spontaneous and stimulated) of photons are described by Einstein's theory of absorption and emission kinetics in a thermal radiation field [8]. The relations between spontaneous emission A_{21}, stimulated emission B_{21} and absorption rate B_{12} in a two-level system (with g_1 and g_2 degeneracies) are:

$$\begin{aligned} g_1.B_{12} &= g_2.B_{21} \\ A_{21} &= 8\pi h\nu \frac{\nu^2}{(c/n)^3}.B_{21} \end{aligned} \tag{1.1}$$

In [9] the authors use Eq.1.1 to deduce the relationship between the absorption (σ_a) and stimulated emission (σ_e) cross-section :

$$\frac{\sigma_a}{\sigma_e} = \frac{g_2}{g_1} \tag{1.2}$$

Considering Eq.1.2 one would expect that for non-degenerate states, the cross-section for absorption and stimulated emission are equal. In a more general case, the values are in the same order of magnitude.

The Stokes shift

In the Jablonski diagram in Fig.1.1 we can observe that the energy of the emission is typically less than that of absorption. Fluorescence typically occurs at lower energies or longer wavelengths since the molecule undergoes vibrational relaxation before emitting a photon. This fact was observed for the first time by Sir. G. G. Stokes in 1852, and the distance between the maximum of absorption and emission is known as the Stokes shift. This phenomenon is important in fluorescence microscopy where it is desirable to separate the excitation wavelength from the fluorescence wavelength as best as possible. In Fig. 1.2 is shown the absorption and emission spectra of Fluorescein in Ethanol (the molecule structure is represented in the inset). We can clearly observe the Stokes shift. As it will be presented further in this work, in our applications the Stokes shift of a dye is of high importance.

Fluorescence quantum yield

The fluorescence quantum yield [10] is the ratio of photons absorbed to photons emitted through fluorescence. If we consider the radiative rate constant k_{rad} and the over-

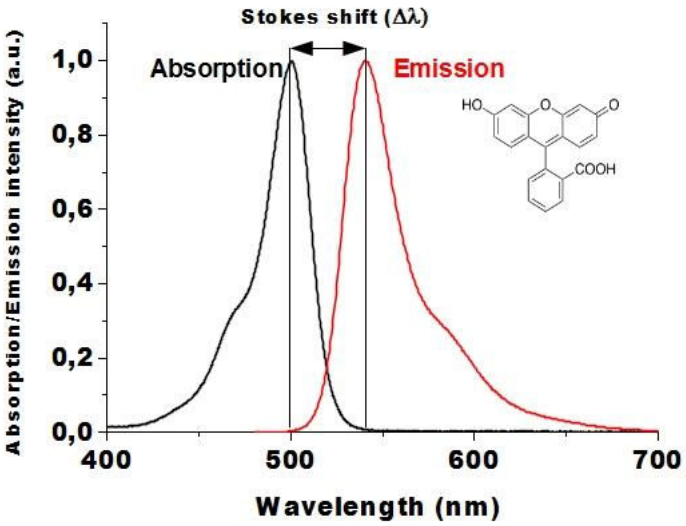

Figure 1.2: Example of a Stokes shift in Fluorescein. The molecular structure of Fluorescein is represented in the inset

all non-radiative rate k_{NR}, then the quantum yield, ϕ is the ratio of the radiative rate to the sum of all the rate of other processes [5]:

$$\phi = \frac{k_{rad}}{k_{rad} + k_{NR}} \tag{1.3}$$

The most used method for determining the quantum yield of a fluorescent species is the comparative method of Williams et al. [11] which involves the use of well characterized standard samples with known ϕ values. In general, a high quantum yield is desirable in all fluorescence imaging applications. For the fluorophores in the visible the quantum yield can reach 80%.

Fluorescence lifetime

Together with the quantum yield the fluorescence lifetime [12] represents one of the most important characteristics of a fluorophore. Fluorescence lifetime (τ) is defined as the time the fluorophore remains in the excited state before returning to the ground state. The typical values of fluorescence lifetimes of allowed transitions in organic molecules are around 10 ns. In [5], the fluorescence lifetime is the reverse of the sum of all the decay rates:

$$\tau = \frac{1}{k_{rad} + k_{NR}} \tag{1.4}$$

One of the most sensitive method for determining fluorescence lifetimes is the Time-Correlated-Single Photon Counting (TCSPC). This method will be detailed further in this work. The fluorescence lifetime is an intrinsic molecular property and generally independent of concentration and when measured with a TCSPC method it is not influenced by fluctuations in excitation source intensity.

Negative effects at the excitation of a molecule: photobleaching, photodegradation and thermal heating
Photobleaching renders a molecule irreversibly non-fluorescent. This phenomenon can be caused by photon-induced chemical damage or other modifications like the addition of radicals to double bonds the chromophore is based on. Studies of photobleaching on well known fluorophores such as fluorescein [13], [14] have been carried. Photobleaching results from multiple processes which, for most compounds, are not completely elucidated.
Photodamage in biological systems refers to damage caused by reactive oxygen species and free radicals formed from photoexcitation. These molecules are highly reactive and thus will interact with their immediate surroundings. This can cause irreversible damage, and often will end in cell or organism death over time.
When a high energy source excites a fluorescent system it can cause local heating that depends on the absorption of the environment (the fluorophore, and the solvent in the case of solutions) and the thermal conductivity. The effect can modify the refractive index, changing the propagation of light in the environment and detection of the optical signal, and eventually can also cause irreversible damage to the system.

1.3 Fluorescence microscopy

Fluorescence microscopy is the general term that refers to any microscope, from epifluorescence to confocal microscope, that uses fluorescence to obtain an image of the labeled sample. The first to have investigated fluorescence microscopy is August Köhler in 1904.

The working principle of a fluorescence microscope

Generally the studied sample is marked with a fluorophore that upon excitation with a high energy source such as a Xenon or Mercury arc-discharge lamp, absorbs light at a certain wavelength emitting at a longer wavelength. This fluorescent light can be separated from the surrounding radiation with filters designed for that specific wavelength allowing the observer to detect only what is fluorescing. The basic task of the fluorescence microscope is to let excitation light radiate the specimen and then sort out the much weaker emitted light from the image.

1.3.1 Main fluorescence microscopy techniques

Fluorescence transmission microscope

This first type of fluorescence microscopy used transmitted light. In this configuration the light passes through a filter (excitation filter) and subsequently is focused in the sample through a condenser. On the opposite side the fluorescence signal from the sample is collected through an objective and a filter (emission filter) that further selects only the fluorescent wavelengths. In this configuration any objective lens can be used as long as its NA is less than the condenser's. The disadvantages of this configuration are the fact that the sample has to be transparent, it is illuminated on a large area causing more photobleaching, very good filters are required and the condenser is hard to align. These days, the fluorescence microscopes with this configuration are not frequently used.

Epi-fluorescence microscope

In epi-fluorescence microscopy, the excitation light comes from above the specimen through the objective lens. The optical setup of this type of microscope is illustrated in Fig. 9.12. The important element that made this setup possible is the dichroic filter that can reflect the excitation wavelength and transmit the fluorescence (as in the setup in Fig.9.12) or the other way around.

This configuration has several advantages in comparison to the transmitted design. One is the fact that the high NA objectives are used at their full aperture, therefore the expected resolution is much better, and images are brighter at high magnification. Another advantage is the fact that with this setup it is easy to combine the fluorescent image with a transmitted light image of the specimen.

Confocal microscope

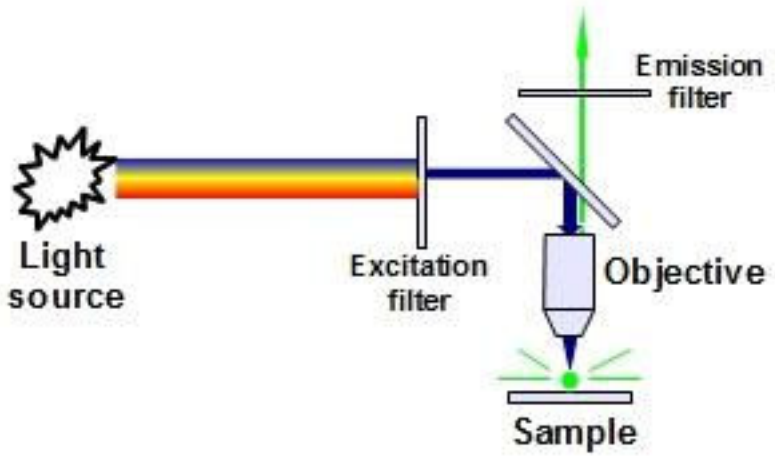

Figure 1.3: Optical scheme of a epi-fluorescence microscope.

The configurations mentioned above are suitable for thin samples, but in the case of thicker samples areas of the specimen above and below the focal plane still contribute to the image as "out of focus blur". This problem can be eliminated using a confocal configuration (Fig.1.4), described for the first time in a patent in 1957 by Marvin Minsky [15]. Confocal microscopy may be derived from conventional microscopy by double spatial filtering. The first filter ensures that, at a given instant, a single point of the field is illuminated. The second one ensures that light returned from the object may reach the detector only if it originates from this point. This spatial filtration successfully excludes out-of-focus emission from the final image and thus enables one to record sections that only include light from the focal plane and close to it. Taking a series of optical slices from different focus levels in the specimen generates a 3D data set.

The key element in a confocal scheme is the detection pinhole placed in a conjugated focal plane. Decreasing the size of the pinhole (up to the diameter of the Airy disk) can increase the sectioning, but if it is to small the signal can be to weak.
The drawback of a confocal detection is the fact that , it can only illuminate a single point at a time. This means that if we want to obtain information from the whole sample, one would need to raster scan the sample or excitation spot in order to assemble a full picture of the sample. Optical microscopes based on this principle are called confocal laser scanning (CLSM) microscopes [16].

Two-photon excitation microscope
Two-photon excitation (TPE) microscopy [17] is a special variant of scanning fluores-

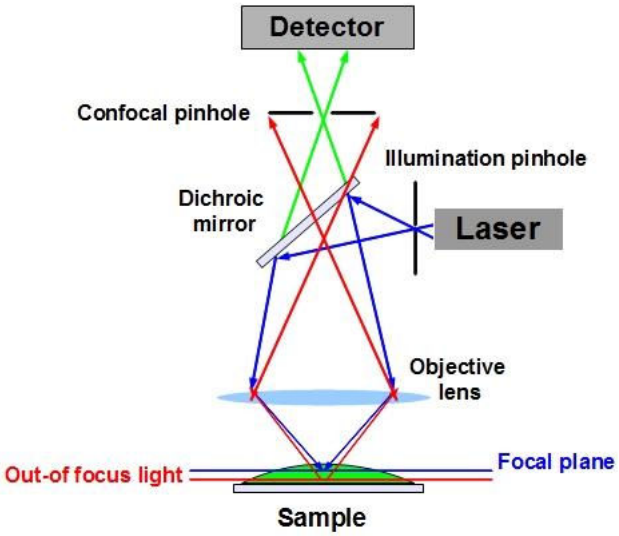

Figure 1.4: Principle of confocal microscopy

cence microscopy based on the two photon absorption process. In the present, it is a well-established microscopy technique with specific advantages such as imaging of living tissue up to a very high depth ($\approx$ 1 mm).
The concept of the two-photon absorption (TPA) process was first proposed in 1931 by Maria Göppert-Mayer in her doctoral dissertation on the theory of two-photon quantum transitions in atoms [18] and was demonstrated experimentally in 1961 by Franken [19]. Two-photon excitation is a nonlinear process related to the simultaneous absorption of two photons with a total energy equal to the energy gap between the ground state and the excited state [20]. In this case, the excitation of the fluorophores that emits in the visible takes place in the infrared spectral range. The Jablonski diagram of the two photon absorption process is represented in Fig.1.5.

Because two photons are absorbed during the excitation of the fluorophore, the probability for fluorescent emission from the fluorophores increases quadratically with the excitation intensity.
In laser scanning microscopy the first demonstration was made by Winfried Denk in the lab of Watt W. Webb at Cornell University in 1990 [17]. Since then an important number of applications and improvements of the method have been published, contributing to the advancement in different fields in biology [21] such as immunology [22] [23], oncology [24], neuroscience [25] and others.

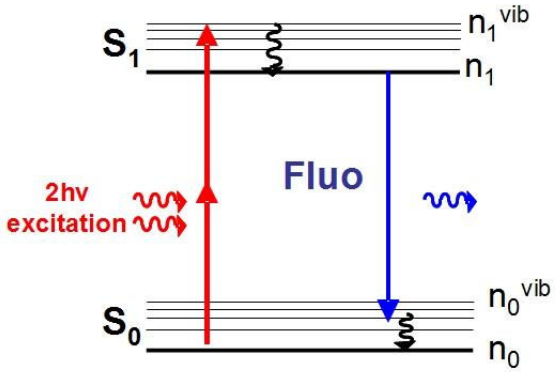

Figure 1.5: Jablonski diagram for the two photon absorption process

Due to the non-linear relationship between the light intensity and excitation efficiency, fluorescence is confined to the focal spot which leads to a reduction of phototoxicity and photo-bleaching outside the focal plane. Compared to confocal configuration, TPE microscopy does not need pinholes to perform 3D imaging, since there is no out-of-focus fluorescence which results in direct axial sectioning. This leads to more efficient light collection in scattering media. Another advantage of TPE microscopy for biological applications comes from using wavelengths in the NIR region, allowing deeper penetration in scattering tissues.
Since the invention of TPE microscopy, this technique has found applications in many diverse areas, ranging from the study of single molecules [26] to deep tissue imaging [27]. In the last years, TPE is starting to be used in clinical studies [28] and in industrial applications. It is a powerful technique: compared with confocal microscopy, it offers the advantages of deeper tissue penetration and less photodamage but has the disadvantage of slightly lower resolution. TPE microscopy is a promising technique that will continue to develop and benefit from developments in optical physics and optoelectronics.

1.3.2 The resolution problem and the new fluorescence microscopy techniques

Fluorescence microscopy and in particular confocal microscopy, is a central tool for life science investigations, allowing non-invasive in vivo observations. When light from a infinitely small point source is traveling through the objective lens of a microscope the size of its image is limited by diffraction [1]. The response of an imaging

system to a point source or point object is called a Point Spread Function (PSF).The image of an object can then be seen as a convolution of the true object and the PSF.

The spatial extension of the PSF determines the resolving power of the imaging system and thus plays a central role in microscopy. The dimensions of the PSF depend on two parameters: the wavelength, λ and the numerical aperture (NA) of the objective lens. The numerical aperture of an optical system is a dimensionless number that characterizes the range of angles over which the system can collect or focus light. The numerical aperture with respect to a point depends on the half-angle θ of the maximum cone of light that can enter or exit the lens (Fig. 1.6).

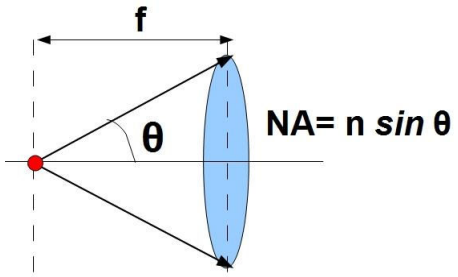

Figure 1.6: Numerical aperture of a lens

In a confocal microscope the PSF is defined as the product of the excitation PSF (due to diffraction, the exciting laser light from a point source is not focused to a point) and the detection PSF (the spatial distribution of the detection probability in the object plane) [29].

For the lateral distribution, the radius of the PSF is:

$$r_x = r_y = 0,61.\frac{\lambda}{NA} \tag{1.5}$$

And for the lateral distribution:

$$r_z = \frac{2n\lambda}{NA^2} \tag{1.6}$$

Therefore, when using visible light and knowing that the best objective lenses has a numerical aperture of NA ≈1.4, the limit is about 200 nm in the focal plane and 600

nm along the optical axis. Therefore, objects that are closer than 200 nm in the object plane and 600 nm on the axial axis cannot be distinguished and imaged as separate objects.

Another characteristic of an imaging system is the optical transfer function (OTF) which is the measure of the image sharpness that the system is capable of producing. It is determined by measuring the contrast in the image of a grid pattern of alternate black and white lines that are more and more closer (low to high spatial frequencies). Therefore it is a transmission measurement of the optical system in terms of spatial frequencies. The OTF is conventionally expressed as the normalized Fourier transform of the PSF, where normalization in this case means scaling so that the value at the zero frequency is 1. OTF describes the weight with which particular frequencies are transferred from the object to the image. It defines the extent to which spatial frequencies containing information about the specimen are lost, retained, attenuated, or phase-shifted during the imaging process . In particular, for high frequencies the OTF decreases to nearly zero and thus those high frequencies will not be present in the image, therefore features with small dimensions cannot be imaged-the resolution is limited.

It has been thought that this resolution limit could not be bypassed, but in the last years, several methods, so-called super resolution microscopy methods, emerged in order to break this limit. Roughly, we can classify these methods from the way they play with the fluorophore population: either by depleting it (Stimulated emission depletion -STED [3], ground state depletion - GSD [30], saturated pattern excitation microscopy-SPEM [31], saturated structured-illumination microscopy - SSIM [32]) or by discreting it (stochastic optical reconstruction microscopy - STORM [33], photoactivated localization microscopy PALM [34], fluorescence photoactivation localization microscopy FPALM [35]). In Table 1.2 are the typical resolutions obtained with the most known super-resolution techniques [36]. These techniques have all achieved improved lateral (x-y) resolution down to tens of nanometers, more than an order of magnitude beneath that imposed by the diffraction limit, but each method has a unique set of limitations.

In the case of PALM and related techniques (STORM and FPALM) the principle behind rests on a combination of imaging single fluorophores (single-molecule imaging) along with the controlled activation and sampling of sparse subsets of these labels in time. All three methods are based on the almost the same principle, but were originally published using different photoswitchable probes. These methods

are simple in both concept and instrumentation, requiring only a modified widefield fluorescence microscope (to conduct single-molecule imaging) and a suitable photoactivatable probe. The obtained spatial resolution is $\approx$ 10-20 nm and 60 nm for the axial resolution and the system is cheaper than other high resolution microscope. The main disadvantages are the long exposure times for one image (15-30 min) and the fact that computation is required - not direct imaging (different analysis software can output different result). Also they require that a very limited number of fluorescent molecules be activated in each cycle of imaging to minimize the number of overlapping fluorophores in each image. This places limits on labeling density and image acquisition speed with most configurations.
Compared to PALM, STED microscopy is faster achieving video-rate speeds in imaging live cells [37]. In STED microscopy there is no need of post-processing of data to obtain an image as in PALM, but the obtained resolution is poorer. One limitation when using stimulated emission depletion to quench the excited states is that the required powers to reach saturation may lead to excessive bleaching. In terms of costs, the STED setups are among the most expensive of the super-resolution techniques (if we consider the commercial setups).
Another emerging super-resolution technique is Structured Illumination Microscopy (SIM) [38, 39] in which the sample is illuminated with a series of sinusoidal striped patterns of high spatial frequency. The illumination patterns interact with the fluorescent probes in the sample to generate interference patterns know as Moiré fringes. By modulating the illumination pattern, collecting and reconstructing the subsequent images, super-resolution images showing a lateral resolution which is doubled and a better background rejection in the axial direction are obtained. Among the benefits of high resolution SIM are the widespread availability of dyes and fluorescent proteins for labeling specimens and the ease of conducting multicolor imaging. The primary drawback is the length of processing time (1 to 30 seconds) necessary to generate high resolution images. Moreover resulting images can be affected by artifacts if the post processing is not very carefully done. The gain in resolution is a factor of 2.

From the point of view of principle as well as instrumentation these new technologies are diverse and so are their opportunities and trade-offs for specific applications. Therefore, when choosing the best technology for a given problem, one has to match experimental requirements with technical performance.

In this work we will focus on STED microscopy. First we will present a general introduction to the working principle of this technique, the main advances and results

Acronym	Principle	XY-resolution (nm)	Main drawback
CLSM	Confocal laser scanning	180-250	Resolution limited by diffraction
SNOM, NSOM	Small aperture scanning (no lens)	20-120	No intracellular imaging
SIM (HELM, PEM) 3D-SIM	Moiré effect with structured illumination	100-130	Reconstruction bears risk of artifacts
SSIM (SPEM)	c effect with structured illumination	50	High excitation required; reconstruction bears risk of artifacts
STED/CW-STED	PSF shaping with saturated emission depletion	20-100	Complex instrumentation; photobleaching
PALM, FPALM, STORM, dSTORM, PALMIR	Photo-switching and localization of single molecules	20-50	Labeling density is critical; performs better on particles and filaments as on volume stains

Table 1.2: Confocal and super-resolution light microscopy methods: XY-resolution and the principle disadvantage

that have been obtained and our contribution to this method.

1.4 STED microscopy

1.4.1 Principle

The principle of STED was first described by Hell and Wichmann in 1994 [2]. In this technique two laser beams control and confine fluorescence emission in a spot that can be much smaller than the diffraction limit. The fluorophores are excited with a focused laser pulse, then a second red shifted pulse with a doughnut shape is sent to deplete the population of the excited state by stimulated emission. Therefore fluorescence can only be emitted in the very center of the excited volume, where the depletion beam has zero intensity. This effectively reduces the size of the PSF and increases spatial resolution.

The simplified Jablonski diagram of the excitation and STED process is presented in Fig.1.7.

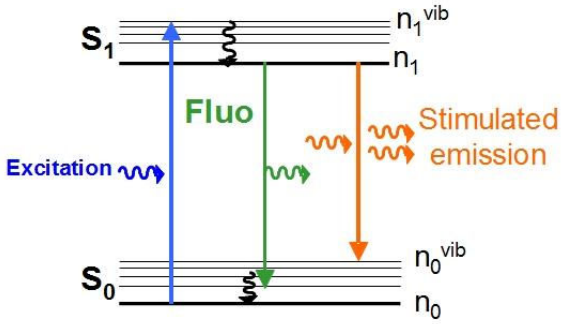

Figure 1.7: Energy levels and optical transitions involved in STED

As in confocal microscopy, the fluorophore is excited from S_0 to a higher vibrational level in S_1 by the focused laser generating a typical PSF in the focal plane. The difference in STED microscopy is that a second laser with the doughnut shape will stimulate the transition S_1 to S_0 (higher vibrational level of S_0) after the relaxation of the fluorophore to a lower vibrational level in S_1. The excitation wavelength is chosen to be as close as possible to the absorption maximum and the wavelength of the stimulated emission beam is tuned to the red edge of the emission spectrum of the fluorophore (the excitation cross section must be small at the STED wavelength, otherwise the STED light would also excite the dye, instead of only stimulating the S_1 to S_0 transition) (Fig.1.8).

In [40] it is underlined that STED depends strongly on the spectroscopic properties of the fluorophore being used. In this work the dynamic behavior of the energy states involved in the STED process is described by a system of four differential equations. Here pulsed lasers are considered for both excitation and depletion and a certain time-delay between excitation and STED pulses is assumed, to temporarily separate the excitation and STED beams (the quenching effect is more efficient if there is no re-absorption in the same time). Ideally, the STED laser beam should arrive at the sample when the electron has dropped though vibrational relaxation or intersystem crossing to a lower vibrational level in S_1. Also the excitation pulse width should be less than 1 ps thus ensuring a vanishing fluorescence decay during excitation and the pulse width of the STED laser should not be longer than the lifetime of the fluorophore. Considering these conditions and solving the equations it is showed that with increasing intensity of the STED beam, the excited state S_1 is more and more

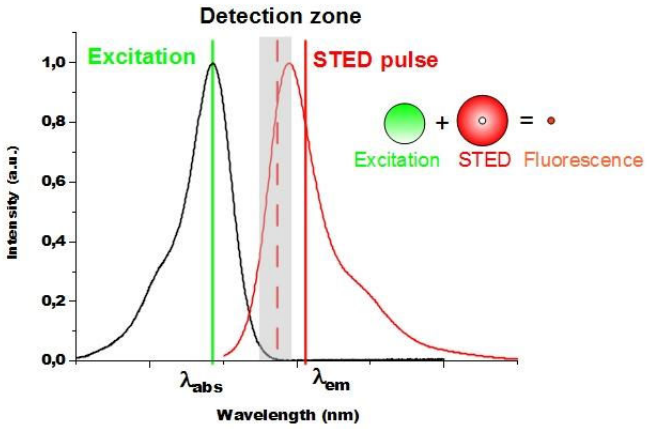

Figure 1.8: Absorption (black line) and emission (red line) of a typical fluorophore, the positions of the excitation and STED pulse and the detection spectral zone

likely depleted until reaching a saturation regime (non-linear), in which the population of the S_1 level is null. It will be showed later that the saturation of the depletion process reduces the width of the lateral main maximum, so that one can expect an increase in lateral resolution by stimulated emission.
In [41] this study is taken forward and if re-excitation is neglected than the population of the fluorescent state, N_1 is quenched accordingly to the following exponential law:

$$N_1 \propto exp^{-\tau\sigma I_{STED}} \tag{1.7}$$

where τ is the pulse duration of the STED beam, σ is the molecular cross section for stimulated emission, I_{STED} is the STED intensity. Therefore it can be observed that the fluorescence signal decreases exponentially as a function of the intensity of the STED beam.

So the question is how can fluorescence depletion be used for resolution enhancement and how can one estimate what resolution can we expect to obtain. As mentioned above, in STED microscopy, in order to use the stimulated emission for increasing the resolution of the microscope, the STED beam is shaped as a doughnut and is overlaid onto the excitation focus of Gaussian shape. Thus, the fluorophores are switched off via stimulated emission in the periphery of the excitation focus. Taking into account the exponential law for the depletion of the excited states, it has been

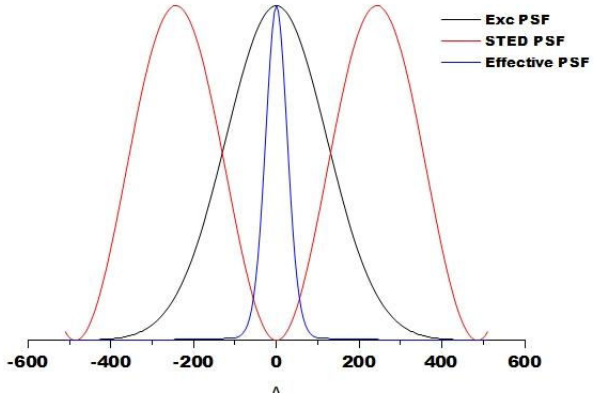

Figure 1.9: Normalized intensity profile of the excitation PSF (black line-Gaussian profile of the form $\exp(-2.x^2/\omega^2)$ where $\omega = \lambda/2NA$), STED PSF (red line- approximated to a standing wave: $sin^2(\pi.x.NA/\lambda)$) and the effective PSF (blue line) of a STED microscope using a exponential depletion efficiency (Eq.1.7).

showed [40] that by using the exponential depletion one can express the achievable resolution as a function of STED power. To model this technique, in [42], the excitation and the STED beam were supposed to have modulated intensity patterns at the maximum spatial frequency that can be transmitted by the microscope objective according to diffraction law. Therefore, the expressions of the normalized excitation probability (h_{exc}) and STED focal intensity (I_{STED}) are:

$$\begin{aligned} h_{exc} &= C\cos^2\frac{\pi.r.NA}{\lambda_{exc}} \\ I_{STED} &= I_{STED}^{max}.\sin^2\frac{\pi.r.NA}{\lambda_{STED}} \end{aligned} \tag{1.8}$$

where I_{STED}^{max} is the maximum value for I_{STED}. The probability to detect a photon after the population was depleted is $h=h_{exc}.exp^{-(\tau\sigma I_{STED})}$.

Using the exponential depletion given in Eq.1.7, the size of the fluorescence spot is:

$$\Delta x \cong 0{,}45\frac{\lambda}{NA\sqrt{1+I_{STED}^{max}/I_{sat}}} \tag{1.9}$$

where $I_{sat}=1/\sigma\tau$ is the STED intensity at which the fluorescence has dropped to 1/e of the initial value I_{STED}^{max}. When increasing STED illumination intensity, the spot

size decreases continuously. Therefore the spot size is not limited any more by diffraction. In theory, there is no limit to the achievable resolution. Nevertheless, in practice I_{STED} cannot be increased infinitely because of photodamage, limitations of the laser or if the zero intensity in the STED beam is not perfect the STED beam would inhibit even the center of the fluorescent spot, so that a compromise between resolution and signal has to be made.

1.4.2 STED microscopy setups

The typical STED microscope setup is illustrated in Fig.1.10. In a simplified manner we could say that a typical STED microscope is a two color confocal microscope. One wavelength is used for the excitation of the fluorophore. The second, the STED beam, passes through a beam shaping device that creates the doughnut like PSF that suppresses excited molecules in the outer parts of the excitation PSF.

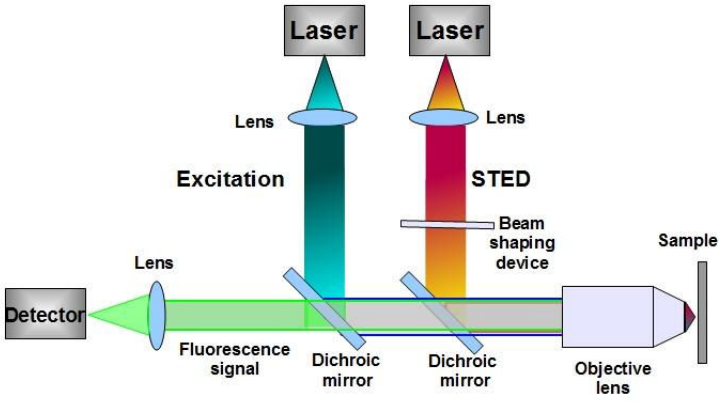

Figure 1.10: A simplified scheme of a typical setup. In addition to the confocal scheme of a CLSM has an additional optical path for the STED beam

Certainly, a STED microscope is more complicated than as presented above, and every setup has its specificity, advantages and drawbacks. A detailed presentation of all the published STED setups would be complex and long. In this thesis the main work was to develop two new approaches for STED microscopy, by implementing an original source in one case, and in the other to use a typical STED laser source in a innovative way. Therefore, we will attempt to make a classification of the setups based on the laser sources used in STED microscopes.

First, the STED setups can be divided in two categories: pulsed STED and continuous-wave (CW) STED depending on the type of the STED laser. Choosing between pulsed and CW STED depends mostly on the application. With pulsed STED a better resolution than with CW-STED can be obtained [43]. Nevertheless, in STED microscopy, working with pulsed laser is more complicated than with CW-lasers, since the pulses have to be synchronized. In other words, one has to ensure that every excitation pulse is immediately followed by a depletion pulse.

Pulsed laser STED setups

The first demonstration of STED microscopy was made with a Ti-Sapphire oscillator operating at 766 nm [3]. The beam was split in two: the first was frequency doubled to 383 nm and used for excitation (pulse duration 200 fs) and the pulses of the second one were stretched to 50 ps and was used for stimulated emission depletion. Since then, other versions and combinations based on Ti-Sapphire laser have been reported [44–47].

Other commonly used pulsed laser sources for STED microscopy are pulsed laser diodes [48]. These setups are less expensive than those based on Ti-Sapphire lasers, they demand minimal maintenance and the timing of the pulses is electronic. The use of the pulsed laser diodes broadens the choice of suitable dyes for STED microscopy.

Other interesting laser sources are the supercontinuum systems, based on a mode-locked fiber oscillator, fiber amplifier, and a photonic crystal fiber generating a broadband spectrum [49]. One of the first demonstration was made in [50] using microstructured optical fiber pomped by a Ti-Sapphire laser to obtain a tunable supercontinuum source. Since then the performance of the supercontinuum STED setups has improved with the advances of the laser sources and the arrival of commercially available sources [51–55]. These configurations are really appealing since the same laser source for both excitation and STED beam is used and therefore the different wavelengths are inherently synchronized. A disadvantage of these configurations is the power loss due to the selection of two or three narrow spectral windows from the supecontinuum spectrum.

There is a constant search for new laser sources that are more compact, at a lower price and yield higher power. There are reports of STED microscopes using mass-produced laser diodes [56], stimulated-Raman scattering sources [57], fiber lasers [58].

Continuous-wave STED

CW-STED setups [59] are more simple, but a higher power is required in order to obtain the same resolution. Higher depletion power in CW STED can result in more severe photobleaching. With the commercial TCS STED CW microscope (Leica Mi-

crosystems, Germany), CW-STED has become the most straightforward of the STED versions. Other versions report the combination of TPE with CW-STED [60], [61], achieving approximately 4-4,5 fold improvement in resolution in the radial direction over conventional TPE microscopy.
CW-STED beams simplify the implementation of STED microscopy, but the depletion beam is always on and would reduce the efficiency of fluorescence inhibition, yielding a poorer contrast, which affects the resolution improvement. Using gated detection [62] can improve the resolution in a CW-STED. In the next section we will present the working principle of gated detection and the practical implementation in a two STED configurations.

1.4.3 Experimental testing of two gated STED setups - internship at Nanobiophotonics

A solution to this problem is gated detection. Initial demonstrations of this method for increasing the resolution have been reported for pulsed laser where time gating is applied in offline analysis [50]. For CW-STED, in 2011 two investigations [63] [62] are revealing the benefit of using a gated fluorescence detection (gSTED) to improve further the resolution of CW-STED and/or to reduce the STED intensity in the sample for a given resolution.
In the configuration presented in [62] the authors used pulsed excitation and CW-STED and for gating they have used a fast electronic gate or offline analysis of TC-SPC data. They show that in the presence of STED the excited-state lifetime $\tau = 1/(k_{fl} + \sigma_{STED}.I_{STED})$ is shortened with increasing I_{STED}. In the doughnut shaped pattern the excited-state lifetime decreases away from the zero-intensity point [64]. Therefore recording photons after a duration T_g (after the excitation pulse), $T_g > \tau$ ensures that fluorescence is collected only from the center of the doughnut where the STED intensity is low and the fluorescence lifetime longer and rejects the photons from the periphery with short fluorescence lifetime increasing the on-off switching contrast which is important in obtaining super-resolution. As a result the effective area from which the fluorescence signal is registered is further confined. Recent work on gated STED [65] [66] [67] have shown that the resolution improvement obtained with a gated CW-STED setup is similar to that obtained with pulsed STED without the use of high powers as reported previously. The scheme of the working principle of gated STED is represented in Fig.1.11.

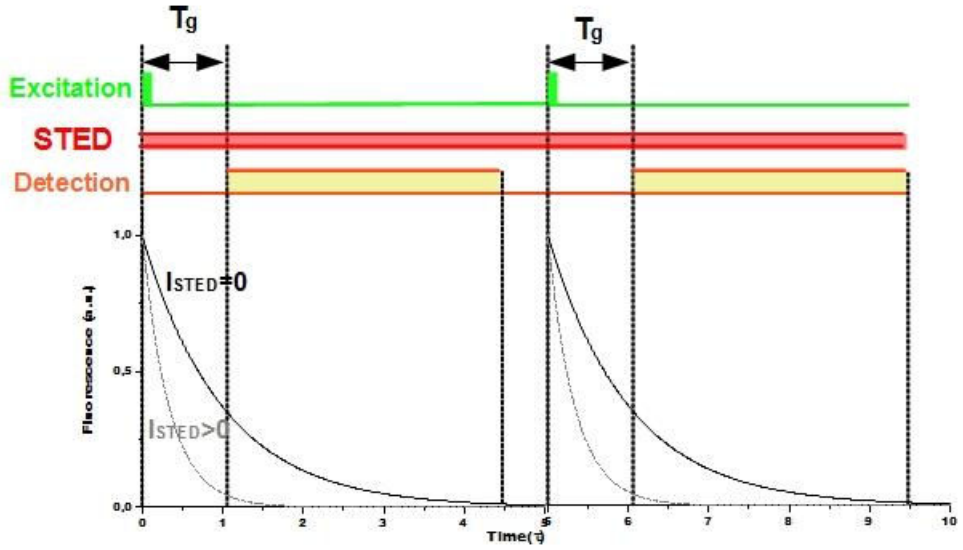

Figure 1.11: Principle of g-STED. Fluorescence lifetimes in the absence (I_{STED} = 0) and presence (I_{STED}>0) of the STED light with experimental time sequence

Here, we will present an example of super-resolution images obtained with the setup in [62]. The work was realized in the frame of a three months internship I have spent in the Department of NanoBiophotonics of Prof.Stefan Hell at the Max Planck Institute for Biophysical Chemistry in Göttingen.
The excitation was provided by a Picoquant picosecond diode laser at 510 nm (LDH-H-C-510, Wavelength 510 nm, Frequency: 80 MHz). The STED laser was a continuous fiber laser (MPB Communications Inc.) operating at 592 nm. The biological samples used were Vero cells with vimentin filaments tagged with yellow fluorescent protein Citrine. In Fig. 1.12 are the scanning images of vimentin filaments in the confocal, STED and gated STED mode. The size of the filament from the inset is 260 nm in the confocal image, 200 nm in the STED image and 160 nm in the gated STED image. We can clearly see that for the same STED power, we were able to obtain a resolution improvement in the STED gated configuration compared to the one without gated detection.

Another setup on which we used the gated detection is based on excitation at 532 nm provided by a Supercontinuum Fianiuim laser source (the wavelength was selected using an Acoustical Optical Tunable Filter-AOTF) and the STED beam was a continuous wave laser at 642 nm (MPB Communications Inc.). The most suitable dyes for this configuration were: Atto 532 and Alexa 546. In Fig.1.13 are presented

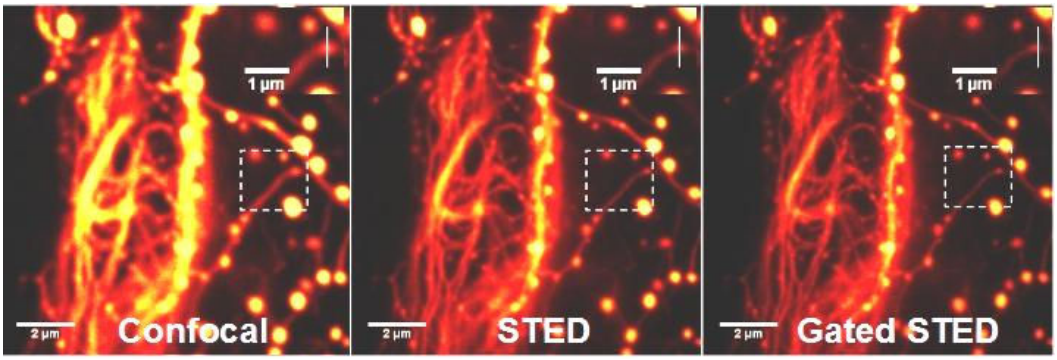

Figure 1.12: Vimentin fibers of Vero cells: confocal, not gated STED and gated STED. P_{exc}=0.75 μW, P_{STED}=80 mW

the confocal and gated-STED scanning images of vimentin filaments of Pkt cells. On the right hand side of the figure are the intensity profiles of filaments. With this setup we obtained a 50 nm resolution at a STED power of 400 mW.

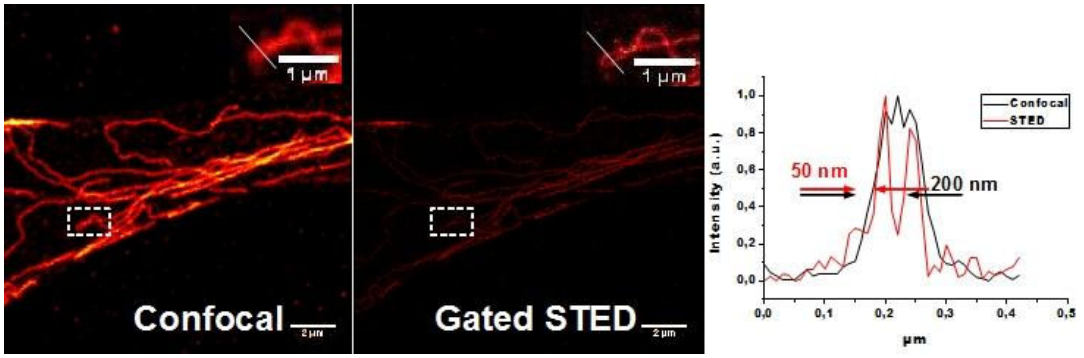

Figure 1.13: Ptk cells: confocal and gated STED images. Profiles of vimentin fibers presented in the inset (P_{STED}=400 mW)

1.4.4 Applications of STED microscopy

Since its first implementation, STED microscopy has seen many improvements, applications and combinations with other techniques and it is continuously evolving. The attainable resolution has increased gradually until reaching a minimum of 5.8 nm in the case of nitrogen vacancies in diamond [68]. It is a versatile method that can used a broad spectrum of fluorescent probes such as: immunostained samples [69], lithographic structures [70], fluorescent proteins [71] and quantum dots [72].
Nowadays STED microscopy is used in biology in the structural analysis of the cell: observation of cytoskeletal filaments [73], [59], [54], of human protein SNAP25 [74],

[75], mitochondrial proteins [76], [77].
An important aspect of STED microscopy is that it allows live cell imaging: detection of structures in mamalian cells [71], [78], of proteins in plant cell [79], of membrane lipids in combination with FCS [80], of dendritic spines [81], of yeast cells using fluorogen activating proteins [82], multicolor live-cell STED [83]. Video-rate imaging with STED has also been reported first for fluorescent beads [84] and after of synaptic vesicles [37] [85]. Recently Berning et al. demonstrated superresolution imaging in a living animal [86]. We can say that STED microscopy is an interesting tool in biology, and there is a high interest in the advancements, improvement and simplification of this technology.

Laser writing lithography is another field that is limited by diffraction in the achievable structure size as well as in structure resolution. In the last years, several studies have been dedicated to understanding and adapting the STED method to the field of sub-diffraction laser lithography. In 2009 two groups have published their approaches of a such a system. Fourkas and al. [87] introduced the Resolution Augmentation through Photo-Induced Deactivation (RAPID) lithography obtaining features of 40 nm size. In the same journal McLeod and al. [88] have introduced a lithography method based on a depletion mechanism named two-color photo-initiation / inhibition lithography (2PII). Since then, the interest in super-resolved lithography has gradually increased and different approaches and mechanisms have been published: Wegener et al. obtained a minimal lateral resolution of 175 nm [89], [90], [91] [92], Klar et al. report a 120 nm resolution and 55 nm structure size in [93] and the recent work of Harke et al. [94], [95] has contributed significantly to the understanding and optimization of the STED-laser lithography mechanism. Sub-micrometer features realized with laser lithography have found applications in diverse fields such as solar cell industry [96] [97], biological sensing [98] [99], lab-on-a-chip technology [100] and other. Therefore there is a constant concern in fabricating smaller features with a reduced cost and one important direction is diffraction-unlimited optical lithography.

STED microscopy is a powerful technique that is used in various fields. It has been discussed that STED microscopy is a complicated and difficult to handle method and that requires a strong expertise in optics. Therefore simplifications and cost reductions are welcome. In this work we will present two concepts that aim at making STED simpler, easier to use and cost effective. We believe that our approaches will enlarge the areas of application of STED microscopy.

Part I

Single source bicolor STED microscopy

Chapter 2

Principle

The concept and performances of STED microscopy were presented in the first chapter of this work. Although STED microscopy has reached resolutions down to a few tens of nanometers, its experimental implementation remains complex and the final system is quite complicated, since two beams generally from different sources have to be coupled into the microscope and perfectly aligned. Moreover, if pulsed lasers are used, additional electronic devices are needed to synchronize the pulses from both sources. It is to be noted that no synchronization is required when CW lasers are used. In the same time it has been shown that CW depletion is less efficient [59], so that a higher average power is required to achieve depletion. This is not desirable, since photobleaching, phototoxicity and heating are critical issues in STED microscopy using organic fluorophores especially when imaging biological samples.

In this chapter, we present our work on the development of a simple and compact STED microscope based on a single laser which delivers both the excitation and the STED beams. Our source is a Q-switched Nd-YAG microchip laser that uses harmonic generation to produce sub-nanosecond pulses at two wavelengths (355 nm and 532 nm). These two wavelengths have the advantage of being intrinsically synchronized and collinear since they are generated from the same fundamental beam, which simplifies the optical setup and electronic apparatus. Moreover the temporal characteristics (sub-nanosecond pulse duration and 150 kHz repetition rate) are particularly well-suited to STED microscopy since they allow efficient depletion while minimizing photobleaching [101].

2.1 Theory

In Figure 2.1 is represented the Jablonski diagram in the case of fluorescence STED microscopy (the same as in Fig.1.7). It is know from Section 1.2 that an excited fluorophore has three relaxation pathways to the ground state: spontaneous emission of fluorescence, non-radiative emission or stimulated emission induced by another photon with a wavelength that matches the energy gap between S_1 and a higher vibrational level of S_0 (Figure2.1).

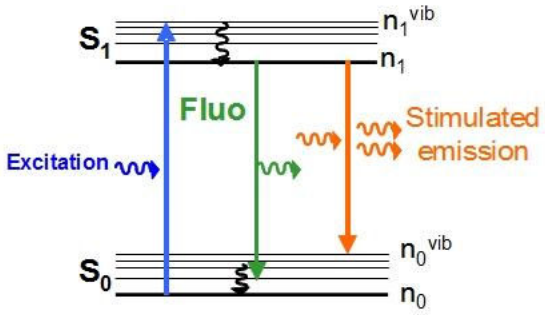

Figure 2.1: Simplified Jablonski diagram showing the electronic and vibrational energy levels of a fluorophore that are considered in the population evolution calculations.

The molecule is excited from the S_0 ground state to the higher vibrational levels of S_1 excited state by the absorption of one photon. The molecule then relaxes to the lower vibrational levels in excited singlet state S_1. By spontaneous emission and non-radiative emission the population in S_1 decays and fluorescence can be observed. In the case of STED microscopy, a second red shifted laser pulse induces stimulated emission and dumps the population in S_1 to the upper vibrational levels of S_0 before fluorescence emission can occur.
The analytical Equations 2.1 - 2.4 are describing these processes. In these equations, σ_{abs} and σ_{STED} are the absorption and the stimulated emission cross section respectively; τ_{rad} and τ_{NR} are the radiative and non radiative relaxation times of the emitting singlet state; τ_{vib} is the rapid vibrational relaxation time which is assumed to be the same for the ground state and the excited state. I and I_{STED} are the intensity of the excitation beam and the STED beam respectively.

$$\frac{dn_1^{vib}}{dt} = \sigma_{abs} I (n_0 - n_1^{vib}) - \frac{n_1^{vib}}{\tau_{vib}} \tag{2.1}$$

$$\frac{dn_1}{dt} = \sigma_{STED} I_{STED} (n_0^{vib} - n_1) - n_1 (\frac{1}{\tau_{rad}} + \frac{1}{\tau_{NR}}) + \frac{n_1^{vib}}{\tau_{vib}} \tag{2.2}$$

$$\frac{dn_0^{vib}}{dt} = \sigma_{STED} I_{STED} (n_1 - n_0^{vib}) + n_1 (\frac{1}{\tau_{rad}} + \frac{1}{\tau_{NR}}) - \frac{n_0^{vib}}{\tau_{vib}} \tag{2.3}$$

$$\frac{dn_0}{dt} = -\sigma_{abs} I (n_0 - n_1^{vib}) + \frac{n_0^{vib}}{\tau_{vib}} \tag{2.4}$$

As described in [40], from equation 2.2 we can say that for an efficient depletion by stimulated emission it is necessary that:

$$\begin{aligned} &\sigma_{STED} I_{STED} n_1 >> n_1 (\frac{1}{\tau_{rad}} + \frac{1}{\tau_{NR}}) \\ &\sigma_{STED} I_{STED} n_1 >> \frac{n_0^{vib}}{\tau_{vib}} \\ &\sigma_{STED} I_{STED} n_1 >> \sigma_{STED} I_{STED} n_0^{vib} \end{aligned} \tag{2.5}$$

In [40] it is suggested that in order to accomplish the first and second condition from Eq.2.5 the best option is to use pulsed lasers for excitation and stimulated emission. Furthermore, the STED pulse has to closely follow the excitation pulse in order to allow the vibrational relaxation from the higher excited levels. Also, in order to avoid spontaneous decay (radiative and non-radiative) it is suggested to have high intensities for the STED beam. As for the last condition, in order to keep the population in level n_0^{vib} low, the rate of stimulated emission has to be much slower than the vibrational decay. Therefore, the STED pulse has to be longer that the lifetime of the vibrational states ($\approx$ 1ps), in order to consider $n_0^{vib} \approx 0$.
If in Eq. 2.2 we consider $n_0^{vib} \approx 0$, for a certain STED pulse duration Δt the population in n_1 is quenched accordingly to:

$$n_1 \propto e^{-\sigma_{STED} I_{STED} \Delta t} \tag{2.6}$$

This exponential law is valid when the STED pulse is short compared to the excited-state lifetime and occurs after the end of the excitation pulse [102] which is the most common case when using femtosecond lasers. The laser we have used is a microchip Q-Switched YAG (or YVO4) Nd3+ with possible repetition rates of 10 to 150 kHz and sub-nanosecond pulse width. We believe that these temporal characteristics of the microchip lasers are particularly well-suited to STED microscopy since, as we will show further in this work, they could allow efficient depletion of organic dyes while minimizing photobleaching [103]. In our case the measured pulse widths of the excitation and STED beam are 0.62 ns and 0.73 ns respectively, and the top of the green pulse is slightly ahead of the UV pulse by 0.11 ns. Therefore, one may assume that the fluorescence quenching might have a different behavior than in previous cases. As a consequence, in the next section we present an analytical expression and the numerical simulations we have performed in order to investigate the stimulated emission depletion efficiency using the temporal properties of our laser and realistic fluorophore characteristics.

2.2 Continuous wave lasers versus nanosecond diode pumped solid state (DPSS) laser

An important parameter in fluorescence microscopy is the light source. Moreover, as mentioned in the beginning of this chapter, in STED microscopy the choice of light sources is more critical than in confocal microscopy. Beside the wavelength choice, one important question is whether to use CW or pulsed lasers. In STED microscopy the best resolution enhancement has been achieved using pulsed lasers systems [43]. Nevertheless, compared to CW-STED microscopes, STED microscopes based on pulsed lasers are considerably more complex. They require pulse synchronization between excitation and STED pulses and in some cases, pulse stretching. Timing adjustment is also required to ensure that the depletion pulse immediately follows the excitation pulse.
In the case of CW-STED the setup is greatly simplified since there is no need of syn-

chronization or pulse stretching. However, as mentioned earlier, to obtain similar resolution as with pulsed lasers three- to five-fold higher average depletion intensities are required.
This issue has been studied and solutions, such as time-gated detection systems [62] are leading to an increased resolution in CW-STED microscopes at lower power (more details in Section 1.4).
Herein, we compare our case with the one where a CW radiation is used for depletion at the same average power. We used a Q-Switched Nd-YAG at 1,06 μm, $\approx$1 ns pulse width, 20 kHz repetition rate. In the configuration described in detail in Section 4.1.1 we generate by second harmonic generation (SHG) and sum frequency (SFG), two temporally synchronized and collinear beams (532 and 355 nm). We will use the 355 nm beam for excitation and the 532 nm for depletion.
In order to better compare the depletion mechanism with pulsed and CW lasers, first we develop an analytical expression and further we perform numerical calculations using the coupled rate equations presented in the Section 2.1.

Comparative analytical description of stimulated emission depletion using nanosecond pulsed lasers and CW lasers

Considering Eq. 2.1 - 2.4 we will assume that the vibrational relaxation time τ_{vib} is very rapid compared to the pulse duration of the laser and the excited state relaxation times (τ_{rad} and τ_{NR}). Therefore, due to the rapid vibrational relaxation, the population n_1^{vib} will quickly arrive to an equilibrium and Eq.2.1 becomes:

$$\frac{dn_1^{vib}}{dt} = 0 = \sigma_{abs} I (n_0 - n_1^{vib}) - \frac{n_1^{vib}}{\tau_{vib}} \tag{2.7}$$

Therefore:

$$\frac{n_1^{vib}}{\tau_{vib}} = \sigma_{abs} I (n_0 - n_1^{vib}) \tag{2.8}$$

Using the expression from Eq. 2.8 in Eq.2.2 we obtain:

$$\frac{dn_1}{dt} = \sigma_{STED} I_{STED} (n_0^{vib} - n_1) - n_1 (\frac{1}{\tau_{rad}} + \frac{1}{\tau_{NR}}) + \sigma_{abs} I (n_0 - n_1^{vib}) \tag{2.9}$$

As a consequence, using Eq.2.8 we obtain the following expression for the population of n_1^{vib} at equilibrium :

$$n_1^{vib} = \frac{\sigma_{abs}.I.n_0}{\sigma_{abs}.I + 1/\tau_{vib}} \tag{2.10}$$

Making the same reasoning for the population in n_0^{vib} as we did for the population in n_1^{vib} at equilibrium we obtain:

$$n_0^{vib} = \frac{\sigma_{STED}.I_{STED}.n_1}{\sigma_{STED}.I_{STED} + 1/\tau_{vib}} \tag{2.11}$$

In a moderate excitation regime ($\sigma_{abs}.I << \frac{1}{\tau_{vib}}$) and a weak depletion regime ($\sigma_{STED}.I_{STED} << \frac{1}{\tau_{vib}}$), considering Eq.2.10 and 2.11, Eq.2.9 becomes (τ - lifetime of the excited state):

$$\frac{dn_1}{dt} = \sigma_{abs} I n_0 - \sigma_{STED} I_{STED} n_1 - \frac{n_1}{\tau} \tag{2.12}$$

For a pulse duration Δt , considering I and I_{STED} constant we obtain:

$$n_1 = \frac{\sigma_{abs} I n_0}{\sigma_{STED} I_{STED} + \frac{1}{\tau}} (1 - e^{-(\sigma_{STED} I_{STED} + 1/\tau)\Delta t}) \tag{2.13}$$

The intensity of fluorescence is proportional to n_1/τ and can be expressed as :

$$I_{fluo} = \frac{\sigma_{abs} I n_0}{1 + \sigma_{STED} I_{STED} \tau} (1 - e^{-(1+\sigma_{STED} I_{STED} \tau)\Delta t/\tau}) \tag{2.14}$$

If the depletion rate is higher than the spontaneous relaxation rate ($\sigma_{STED} I_{STED} >> 1/\tau$) we can express the fluorescence intensity from Eq. 2.14 as:

$$I_{fluo} = \frac{\sigma_{abs} I n_0}{1 + \sigma_{STED} I_{STED} \tau} \tag{2.15}$$

Equation 2.15 is also valid in the case of CW-STED ($\Delta t \to \infty$). We note that in

Eq.2.15 in the case of the pulsed laser, I_{STED} represents the peak power. When comparing with CW-STED we can conclude that the same depletion efficiency could be obtained, in the pulsed case, with a average power lower by a factor of $1/(f \cdot \Delta t)$ (Δt being the pulse duration and f the repetition rate of the laser).

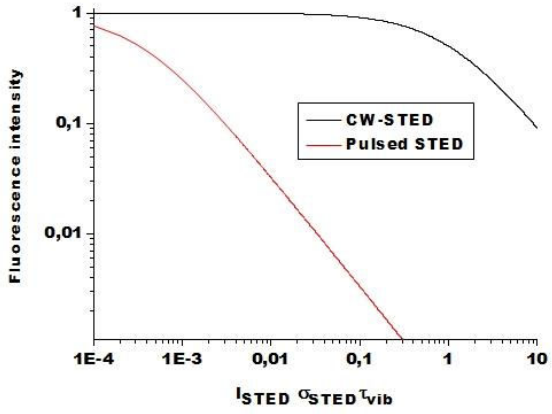

Figure 2.2: Graphic representation of normalized fluorescence emission quenching as a function of average STED intensity for ns-pulsed STED light (red line) as compared to CW STED (black line) obtained from Eq. 2.15. (The horizontal axis is scaled with the dimensionless quantity $I_{STED}\sigma_{STED}\tau_{vib}$)

In Fig.2.2 is represented the depletion efficiency of fluorescence as a function of the average STED intensity in the two cases of laser sources. We can clearly see that the nanosecond pulsed laser is more efficient that the CW laser at the same average intensity. This behavior does not follow the commonly mentioned exponential dependence for fluorescence quenching. As shown by the expression in Eq.2.15 we can say that in our case the fluorescence quenching follows a hyperbolic law. A similar hyperbolic expression has been obtained previously [104] in the case of CW STED (in a moderate depletion regime $I_{STED} < 10^3 I_{sat}$). It is not surprising that the same expression is valid for nanosecond pulses and CW-STED, since the pulse duration is long enough to allow a steady state in the excited state population.

In order to confirm the validity of the approximations made in the analytical part for our particular case of nanosecond pulsed lasers, when the STED pulse overlaps the excitation pulse and the pulse duration is close to the fluorescence lifetime, we have performed numerical simulations presented in the next section.

Numerical simulations of fluorescence quenching with CW lasers and nanosec-

ond pulsed lasers

The simulation is performed for total duration of 10 ns (we assume that complete relaxation has occurred 10 ns after the pulse) with a 0.2 ps time increment. The population in the four levels of interest were evolved according to the rate equations (Eq.2.1-2.4) The excitation and STED pulses were given a Gaussian temporal profile with a FWHM of 0.62 ns and 0.73 ns respectively, with the green pulse slightly ahead of the UV pulse by 0.11 ns (measured values). The fluorescence signal is considered proportional to the population n_1 integrated over the duration of the simulation. We have compared our case with the case where a CW radiation is used for depletion at the same average power. Fig.2.3 shows the normalized fluorescence emitted by a molecule as a function of the average STED intensity, using either our pulsed STED source (at 150 kHz repetition rate) or CW STED. In this calculation, the following values are used: $\sigma_{abs} = 2.10^{-17}$ cm^2 which is that of Coumarin 490 and $\sigma_{STED} = 10^{-17}$ cm^2 which is a realistic value.

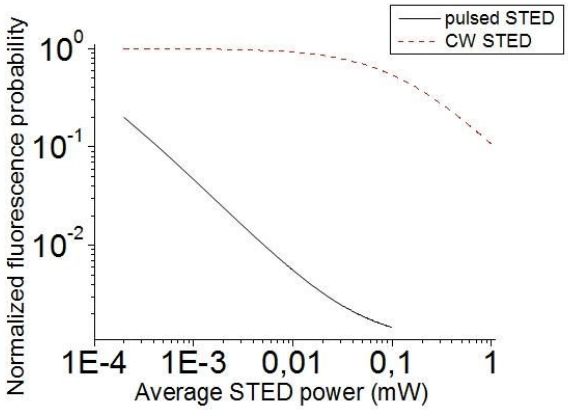

Figure 2.3: Normalized fluorescence emission probability as a function of average STED power for ns-pulsed STED light, such as delivered by the laser developed here, (solid line) as compared to CW STED (dashed line) obtained by the numerical simulations.

The results shown in Fig.2.3 confirm our findings from the previous paragraph. In agreement with the analytical expression of the previous paragraph, we observe that the depletion efficiency does not depend exponentially on the STED intensity as considered in many articles. In our case, this dependence appears close to a hyperbolic law (since it is linear with a -1 slope on a log-log scale) for moderate STED power: the fluorescence decreases faster at the beginning then it tends to plateau, compared to an exponential law. The middle portion of the curve can be correctly

fitted by the expression $1/(1 + I_{STED}/I_{sat})$ where I_{sat}, usually named saturation intensity, is by definition the STED intensity resulting in the inhibition of half the initial fluorescence emission. I_{sat} is of course inversely proportional to the stimulated emission cross-section σ_{STED} at the STED wavelength. When comparing the two curves of Fig.2.3, pulsed STED irradiation appears much more efficient than CW irradiation of the same average power. Indeed, the average saturation intensity (which is the value that causes half of the fluorescence to be depleted) is I_{sat}^{pulsed} =18 kW/cm^2 for pulsed STED, whereas it reaches I_{sat}^{CW} =37 MW/cm^2 for CW STED. A factor of 5.10^3 is found between the two cases. If, as argued above, the STED pulses are longer than the excited state lifetime so that the fluorophore feels a continuous irradiation during this time, the total effective energy that can be used for depletion would be proportional to the instantaneous intensity. Therefore, to obtain the same depletion efficiency in CW STED, the average power would need to be as high as the instantaneous power in the pulse. The ratio of instantaneous to the average power is expressed as $1/(\tau f)$ (with τ the pulse duration and f the repetition rate) which is around 10^4 for our laser, which is in rough agreement with the value (5.10^3) found from the simulation.

Considering the analytical interpretations and numerical simulations we have presented above, we can say that the nanosecond microchip Q-switched laser is an interesting alternative to femtosecond and CW laser in STED microscopy since they are considerably cheaper, compact, low repetition frequency and nanosecond pulse duration which minimize photobleaching and allow fluorescence quenching by stimulated emission depletion at relative low average powers.

Chapter 3

Dyes

In this chapter the adequacy of our laser source for depletion experiments is investigated in solutions of fluorescent dyes. This step is essential in our research since only a few studies have reported the use of blue dyes in STED microscopy [105] with pulsed lasers both for excitation and depletion. We have chosen a series of dyes which can be excited at 355 nm and have a large Stokes shift, in order to have a good stimulated emission cross section around 532 nm. In the first part of this section we have described the setup used for testing the dyes. In the second part we show the experimental and theoretical results on dyes from different families.

3.1 Experimental setup

One major issue in STED microscopy is the choice of dyes. In order to establish the most suitable dyes to use in our approach we have built a setup to test in solution the fluorescence quenching efficiency at 532 nm. The setup is presented in Figure 3.1. The laser used in this study is an earlier model of the one used in the numerical simulations and microscopy applications, which has a repetition rate of 20 kHz instead of 150 kHz, with the same pulse duration.

The output of the laser system is sent on a near-UV achromat of 12.5 mm focal length (Edmund Optics, York, UK) which focuses the beam into a spectrometer cell containing a dye solution. The power at 355 nm and 532 nm are controlled indepen-

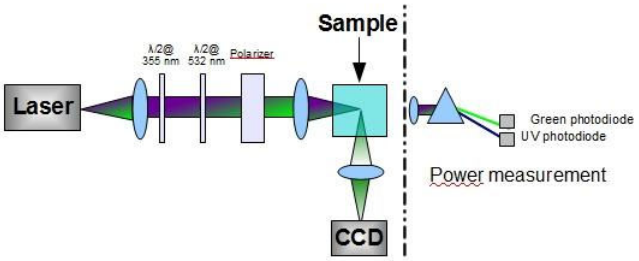

Figure 3.1: Experimental setup for dye testing

dently using chromatic half-wave plates followed by a polarizer. The first birefringent plate is half-wave at 355 nm (a retardation of $\lambda/2$ is introduced between the two axis) and wave at 532 nm (the retardation is multiple of λ), so that it rotates only the 355 nm light, whereas the second has a $\lambda/2$ retardation at 532 nm while it does not affect the 355 nm beam. Polarization plays an important role in the efficiency of stimulated emission. It is known that depletion efficiency by stimulated emission depends on the angle between the polarizations of the excitation and depletion [106]. The most efficient depletion is obtained if the polarizations are parallel [5]. Therefore, in all experiments described below the polarizations for the excitation and depletion beam were set in this configuration.

The sample consist of a 10 mm light path, four sides polished quartz cell containing the studied solution. The fluorescence emitted in the dye solution at 90° from the laser propagation direction was recorded by a CCD camera. Power calibration measurements were performed by splitting the two wavelengths by a glass prism and separately focusing each beam on a calibrated photodiode.

3.2 Blue dyes for single source dual wavelength STED

3.2.1 Method

Our approach was the following:
i) First we took a CCD image of the fluorescence trace when the power of the 532 nm beam was 0 W
ii) Secondly CCD images were acquired as we gradually increased the green power

(532 nm). The excitation (355 nm) power is kept very low (in the μW range) to avoid saturating the singlet transition
iii) The profiles integrated over the full width of the beam are extracted from the images.

Fig.3.2 depicts the fluorescence trace in a solution of Coumarin 490 in ethanol. Coumarin 490 is a common laser dye for blue operation [107]. The absorption and emission spectra of Coumarin 490 match the two operating wavelengths (as shown in the inset of Fig.3.2). When only the excitation beam at 355 nm is present, the profile is a slowly decaying line, since the laser beam is attenuated by absorption in the dye solution. When the 532 nm beam is unblocked, a sharp hole appears in the fluorescence image at the position of the beam focus as shown on the CCD image and the fluorescence profile reveals a dip corresponding to an almost complete extinction. This confirms that our laser source is capable of efficient fluorescence inhibition by stimulated emission.

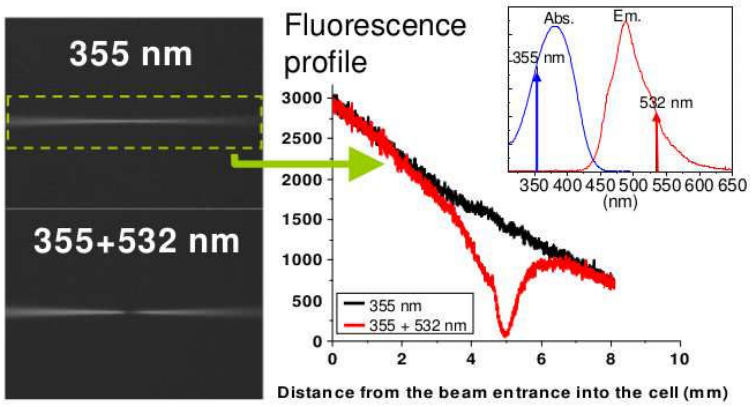

Figure 3.2: Images of the fluorescence trace when focusing into a solution of Coumarin 490 in ethanol (left-hand side) with the 355 nm beam (top) and both 355 nm and 532 nm beams (bottom). The integrated profile extracted from these images (right-hand side) shows almost complete fluorescence extinction. The normalized absorption and emission spectra of Coumarin 490 is shown in the inset.

3.2.2 Tested dyes for 355 nm excitation and 532 nm STED

A number of common dyes, which we will present in the following paragraphs, have suitable spectral properties for the 355 nm/532 nm wavelengths pair. Examples include laser dyes especially from the Coumarin family and Hoechst dyes which are widely used to stain the nucleus [108] in live or fixed cells since they are cell-

permeable and bind to DNA. Another compound of biological significance and possessing the adequate spectra is the reduced coenzyme NADH which is naturally present in all living cells.

Coumarin 490

Coumarin is a fragrant organic chemical compound in the benzopyrone chemical class, which is a colorless crystalline substance in its standard state. Coumarin derivatives are used in a wide range of applications, such as dye-sensitized solar cells (DSCs) and dye lasers, and have therefore attracted considerable research interest. Coumarin 490 (Exciton, USA) is presented as bright yellow crystalline needles and is an efficient laser dye for pulsed operation; tunable around 490 nm (absorption and emission spectra are presented in Fig. 3.3).

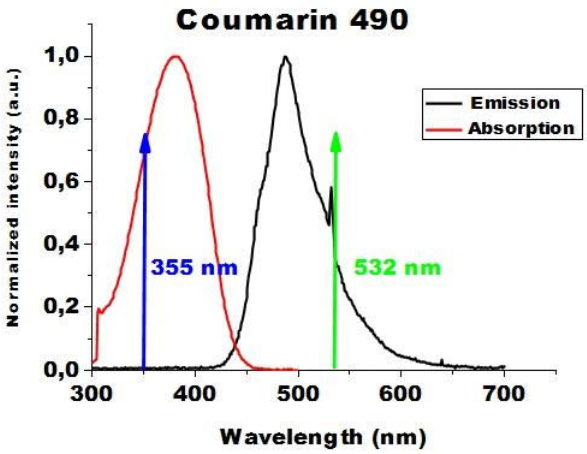

Figure 3.3: Normalized absorption and emission spectra of Coumarin 490 in Ethanol.

Hoescht 3342

Hoechst stains are part of a family of blue fluorescent dyes used to stain DNA that have multiple applications, such as sensitive detection of DNA in the presence of RNA in agarose [109], automated DNA determination [110], sensitive determination of cell number [111] and chromosome sorting [112]. They are excited by ultraviolet light at around 350 nm, and emit blue/cyan fluorescent light around an emission maximum at 461 nm. There is a considerable Stokes shift between the excitation and emission spectra that makes Hoechst dyes useful in experiments in which multiple fluorophores are used.

Hoechst dyes are soluble in water and in organic solvents such as dimethyl formamide or dimethyl sulfoxide. The absorption and emission spectra of Hoescht 3342 in water is shown in Fig. 3.4

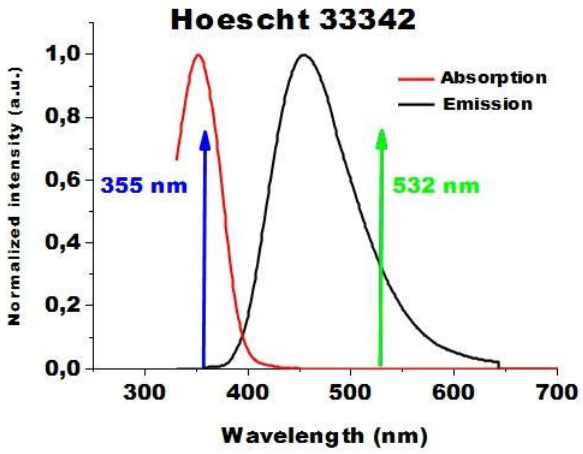

Figure 3.4: Normalized absorption and emission spectra of Hoescht 33342 in water.

BF3

BF3 is non-ionic blue fluorescent water-soluble chromophore developed by Frédéric Bolze and his team from Laboratoire de Biophotonique et Pharmacologie, Strasbourg, France [113]. It is a blue fluorescent chromophore developed for two-photon microscopy. An important characteristic is its water solubility, which is of high interest in imaging biological specimens. We considered this fluorophores to be interesting for our applications since it has a good brightness and high stability. The absorption and emission spectra are shown in Fig. 3.5. The chemical structure is represented in the inset.

NADH

NADH stands for "nicotinamide adenine dinucleotide (NAD) + hydrogen (H)". This coenzyme occurs naturally in the body and helps the functionality of enzymes in the body. In [114] it is stated that NADH plays an important role in cell death and various cellular functions including regulation of calcium homeostasis and gene expression. Its absorption and emission spectra in water are shown in Fig. 3.6 Fluorescence microscopy is widely used to characterize this coenzyme (oxidized or reduced, free or bound to proteins) as an indicator of the metabolic state of cells and

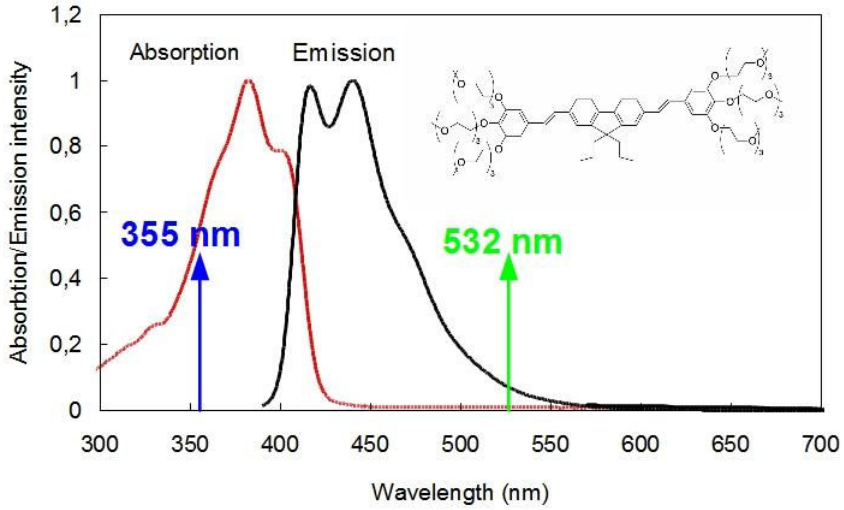

Figure 3.5: Normalized absorption and emission spectra of BF3 in Ethanol.

tissues [115], [116]. Therefore, it would be of biological interest to built a STED microscope with excitation around 350 nm for these studies on metabolism.

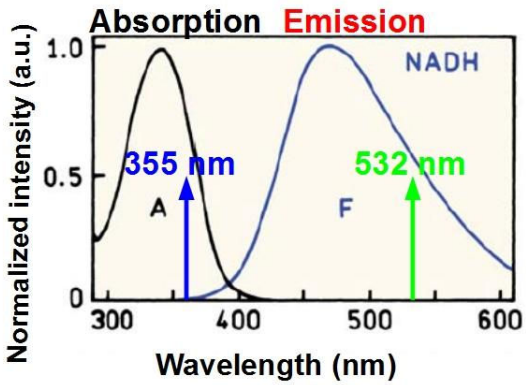

Figure 3.6: Normalized absorption and emission spectra of NADH in water.

3.2.3 Measured STED efficiency

Our purpose in this section is to evaluate and compare the ability of several suitable dyes to be stimulated at 532 nm. In order to extract useful quantities from the measured fluorescence profile, we used the following model: we assumed that the

excitation and depletion beams are Gaussian beams along the propagation axis (with the waist varying as a Lorentzian function).

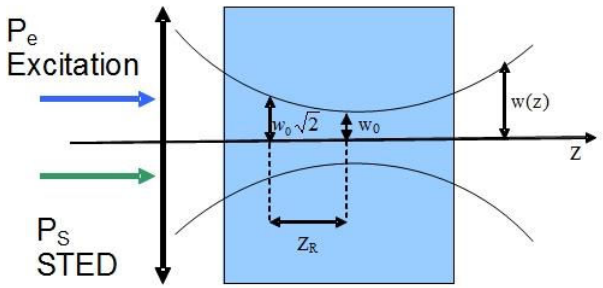

Figure 3.7: Gaussian beam width variation, w(z), as a function of z distance

Gaussian beams are characterized by the distribution of the intensity which can be expressed as a function of the axial and radial distances z and r=$\sqrt{x^2+y^2}$ and the beam power P:

$$I_{r,z} = \frac{2P}{\pi.w(z)^2}.e^{\frac{-2r^2}{w(z)}} \tag{3.1}$$

Within any transverse plane, the beam intensity assumes its peak value on the beam axis, and drops by the factor $1/e^2$ at the radial distance r = w(z) named the beam radius (also called the beam width). The dependence of the beam radius on z is governed by:

$$\mathrm{w}_z = \sqrt{\frac{\lambda Z_R}{\pi}} \cdot \sqrt{1+\frac{z^2}{Z_R^2}} \quad \text{where } Z_R = \frac{\pi w_0^2}{\lambda} \text{ is the Rayleigh length} \tag{3.2}$$

w(z) assumes its minimum value w_0 in the plane z = 0, called the beam waist. Thus w_0 is the waist radius.

For the sake of simplicity, we make the approximation of a constant intensity in a section with the radius equal to w(z) we then can express the surface of the section at z position as: S(z)=$\pi.w_z^2$. Using 3.2 we obtain:

$$S(z) = \lambda Z_R \cdot (1+\frac{z^2}{Z_R^2}) \tag{3.3}$$

Therefore, the mean intensity at an axial distance z from the beam waist, I(z), ob-

tained by dividing the total power (P) by the area within the radius w(z), S(z), can be expressed by:

$$I(z) = \frac{P}{S(z)} = \frac{P}{\lambda Z_R \cdot (1 + \frac{z^2}{Z_R^2})} \tag{3.4}$$

The fluorescence emission is proportional to the excitation intensity I_{exc} times the depletion factor. This last factor is assumed to depend on the STED intensity I_{STED} according to the empirical hyperbolic law given by the simulations (c.f. Chapter 2), so that the fluorescence signal F at position z is, with I_{sat} the saturation intensity (averaged over time):

$$F(z) \propto I_{exc}(z) \left(\frac{1}{1 + I_{STED}(z)/I_{sat}} \right) \tag{3.5}$$

Here we assumed that the STED beam completely covers the excitation beam, which is possible for a perfect alignment: if the waist size for 355 nm and 532 nm are similar (this is expected in the nonlinear crystal used for sum frequency generation), the 532 nm beam would be more divergent than the 355 nm beam, since Gaussian beam divergence scales with the wavelength, so that it can completely cover the 355 nm beam. The profile is then given by the expression $\frac{1}{1+\gamma}$, where $\gamma = I_{STED}(z)/I_{sat}$ stands for the depletion rate. An example of the evolution of the depletion dip as a function of γ is shown in Fig.3.8.

The fluorescence trace observed on the CCD is a sum of all the planes across the beam width. Since we want to make a comparison with the experimental profiles we have obtained by integrating the data in the rectangle, we have to calculate the fluorescence emission integrated over a whole xy section with z constant:

$$p(z) = \int\int F(z)dxdy \propto P_{exc} \left(\frac{1}{1 + I_{STED}(z)/I_{sat}} \right) \tag{3.6}$$

$$p(z) \propto \left(1 + \frac{P_{STED}}{I_{sat}\lambda Z_R \left(1 + \frac{z^2}{Z_R^2}\right)} \right)^{-1} \tag{3.7}$$

with P_{STED} the average power at 532 nm and Z_R the 532 nm beam Rayleigh range.

The fluorescence profiles obtained in Coumarin 490 solution at several STED powers are shown on Fig.3.9(a). The fitting function $(1 + \gamma/(1 + z^2/Z_R^2))^{-1}$ successfully

accounts for the growth and widening of the depletion dip as the 532 nm power increases. The parameter γ is obtained from the fit for each value of the STED (532 nm) power. Only powers typically ≤ 2 mW were considered, since our model is valid for moderate fluorescence inhibition (c.f.Chapter 2).

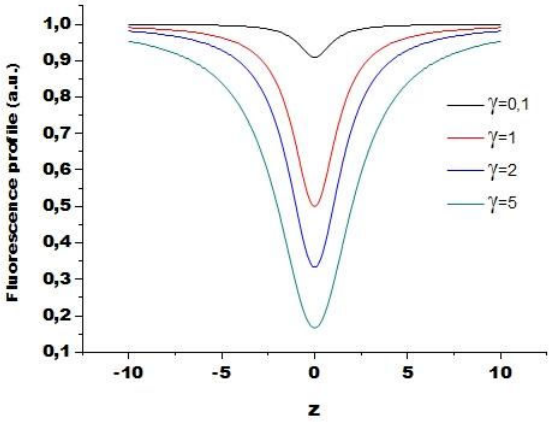

Figure 3.8: Examples of fitting function for different values of the γ parameter

γ should depend linearly on the STED power, as shown by Eq.3.7. Fig.3.9(b) confirms the validity of this model for moderate powers. The slope of this line is $(\lambda Z_R I_{sat})^{-1}$. Therefore an estimation of the (time-averaged) saturation intensity I_{sat}, which is by definition the STED intensity that inhibits half of the fluorescence emission, can be obtained for each compound. The value of I_{sat} indicates the ability of a molecule to be depleted efficiently with our laser: it takes into account the stimulated emission cross section at 532 nm, as well as temporal properties such as how well the pulse duration matches the excited state lifetime.

This method allows the comparison different compounds in a concentration-independent manner. The results we obtained for I_{sat} with Coumarin 490, Hoechst 3342, NADH and BF3 (non-commercial dye) are shown in Table 3.1. Unsurprisingly NADH is less efficient (I_{sat} is higher by a factor of two) than the other fluorophores which are quite similar. One possible reason is the high rate of non-radiative decay in NADH, resulting in an excited-state lifetime of only 0.4 ns [117]. Since our pulse duration is around 0.7 ns, only a fraction of the STED pulse energy is useful for depletion, so that the power has to be increased to obtain the same depletion effect.

The values measured for I_{sat} allow an estimation of the stimulated emission cross-section σ_{STED} if we use the usually admitted relation $I_{sat} = ln(2)h\nu_{STED}f/\sigma_{STED}$ [45] which has been derived for a STED pulse shorter than the fluorescence lifetime which

Compound	I_{sat} in kW/cm^2	σ_{STED} in cm^2
Coumarin 490	1.2	$4.7.10^{-17}$
Hoechst 3342	1.3	$4.3.10^{-17}$
BF3	0.98	$5.7.10^{-17}$
NADH	2.3	$2.4.10^{-17}$

Table 3.1: Experimental time-averaged saturation intensity for stimulation obtained with different compounds.

occurs after the end of the excitation pulse. Although it is not absolutely valid in our case as shown by the numerical simulations, it yields an approximate value of σ_{STED} for Coumarin 490, Hoescht 3342, BF3 and NADH (Table 3.1). In the case of Coumarin 490, $\sigma_{STED} = 4.10^{-18}$ cm^2. This value should be compared to the absorption cross-section of Coumarin 490 which is $\sigma_{abs} = 2.10^{-17}$ cm^2 at maximum. The estimated value of σ_{STED} is a little weak, probably due to imperfect overlapping of the two beams which made us underestimate the depletion efficiency. The order of magnitude of σ_{STED} can be correctly estimated, although the main interest of the present method is the ability to compare the STED efficiency of several dyes given the laser's specific spectral and temporal characteristics.
The obtained values in Table 3.1 show that at relative low powers we could obtain an efficient depletion proving that our laser source represents an interesting source for a simpler STED microscope.

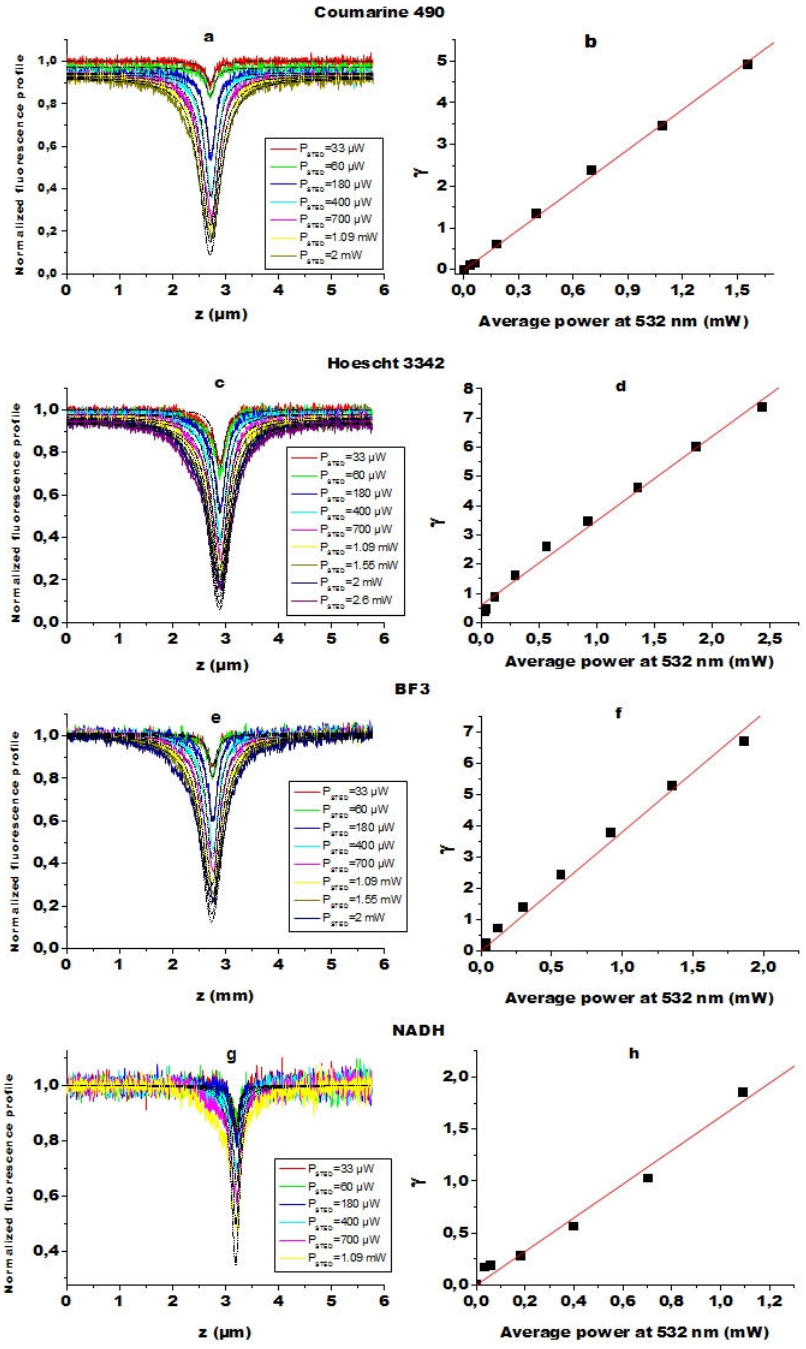

Figure 3.9: Measurement of depletion efficiency in solution: (a),(c),(e),(g) Normalized fluorescence profiles obtained in a solution of Coumarin 490, Hoescht 3342, BF3 and NADH respectively at different STED powers. The fit (solid black line) yields the value of γ according to the expression in the text. (b),(d),(f),(h) Plot of the parameter γ obtained from the fits as a function of the STED power for Coumarin 490, Hoescht 3342, BF3 and NADH.

Chapter 4

Experimental setup for microscopy

In the previous chapters we have explained the working principle of our version of STED microscope with a single laser source delivering two wavelengths. We underline the fact that such a configuration will be simpler, cheaper and more stable. One interesting characteristic is the fact that the excitation is in the UV range, thus expanding the wavelength range of STED microscopes.
In this chapter we present the steps we have made in the building process of the Single Source Dual Wavelength STED microscope. In the first part we present the configuration optimization concerning the development of the laser source, the objective selection, the choice of detection and scanning modes. In the second section we present the beam shaping device that creates the phase singularity with the zero intensity point in the center of the STED beam without changing the excitation beam. In the last section we present the final configuration we have used for imaging fluorescent samples.

4.1 Configuration optimization

4.1.1 Lasers

Our choice for the laser source was a diode pumped solid state (DPSS) laser, also called microchip lasers and more particularly, those based on passively Q-Switched YAG (or YVO4) Nd3+. These lasers have become very popular because of their robustness and compactness. In addition their temporal characteristics (sub-nanosecond pulse width and 10-150 kHz repetition rate) and high beam quality (a M^2 close to 1) [118] are favorable to produce, by second harmonic generation (SHG) and sum frequency (SFG), beams at 532 and 355 nm. These beams, by principle, are temporally synchronized and we will see that it is possible to have them perfectly collinear. Since these two wavelengths are perfectly matched (355 nm for excitation and 532 nm for stimulation) with many blue dyes all the criteria needed for a good STED source are met in these lasers. Unfortunately the commercial product designs optimize independently 532 nm or 355 nm and a misalignment occurs between them. In this section we will present the DPSS lasers and the SHG-SFG configuration we have used for our microscope.

Commercial UV Q-Switched Nd :YAG laser - 8 kHz

Our first laser source was a 8 kHz passively Q-Switched Nd :YAG laser (SNV-05P, Teem Photonics, France) built for emission at 355 nm. A schematic view is represented in Figure 4.1.

The main components of the laser are an infrared laser, two LBO non-linear crystals, two lenses and adequate chromatic wave-plates. The phase matching is type I for second harmonic generation ($\theta = 90°$, $\phi = 11°$, $\gamma(\theta)$= 7mrad = 0,4°) and type II for the sum frequency generation ($\theta = 42°$, $\phi = 90°$, $\gamma(\theta)$= 9mrad=0,53°). In order to obtain a two color source from this laser, we removed the filters which blocked the 532 nm emission.
As expected, since the laser was optimized for 355 nm, the 532 nm beam proved not to be of high quality as it can be clearly observed in the image of the 355 nm and 532 nm beam from Figure 4.2. In blue is depicted the 355 nm beam which has a profile close to Gaussian, and in green is the 532 nm beam that has a profile more similar to the TEM_{01} mode. Therefore, a first solution we have adopted was to filter the beams through a telescope with a pinhole. One problem was the need for pinholes that resist

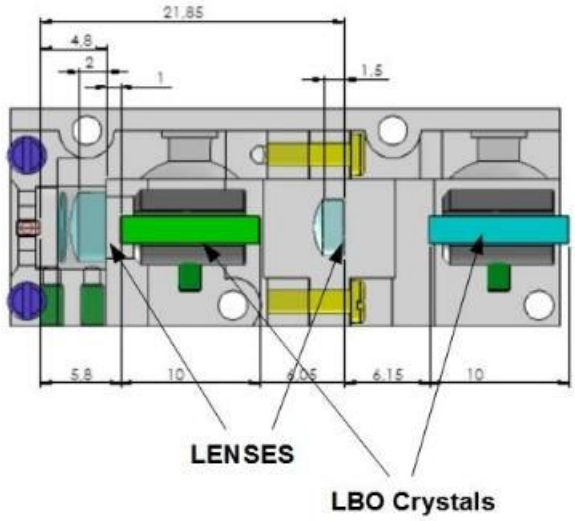

Model	SNV-05P
Wavelength (nm)	355
Peak Power (kW)	2
Average Power (mW)	6
Repetition rate (kHz)	8
Pulse Width (ps)	400
Energy/Pulse (µJ)	0.8

Figure 4.1: Schematic view of the SHG and SFG part of the commercial 8 kHz laser (left-hand side). Typical values for SNV-05P, Teem Photonics (right hand-side)

at high UV powers.
Since we found that the spatial filtering was not sufficient we chose to fiber couple the laser. The fiber coupling was done using a single-mode pure silica core optical fiber (S405-HP, Thor Labs, USA) and a focusing lens of focal length f=12.5 mm. The fiber had single mode transmission from 400 to 550 nm. At 355 nm the fiber is not single-mode and can transmit higher order modes. In order to eliminate these unwanted modes, the fiber was wound around a 2 cm-diameter cylinder: since losses are predominantly induced in the higher modes, only the TEM 00 mode was still present after a propagation length of around 1 meter. The disadvantage of this configuration was the power loss due to the fiber coupling. The maximum power obtained at the exit was less than 10% of the power at the entrance (5% for 532 nm beam and 3% for the 355 nm beam) .

Infrared Q-Switched Nd :YAG laser 20/150 kHz - Second Harmonic Generation(SHG) and Sum Frequency Generation (SFG)

A solution to the low beam quality was to build our own configuration of harmonic conversion and optimize the necessary parameters for our applications. Our goal was to obtain high quality Gaussian beams for the two wavelengths (355 and 532 nm) and the maximum power at 532 nm.

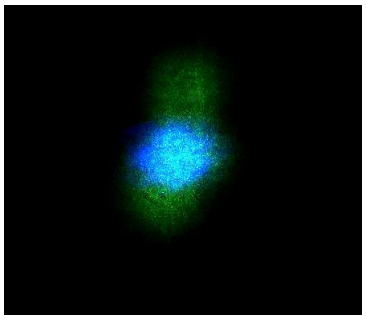

Figure 4.2: CCD image of 355 nm beam (blue) and 532 nm beam (green) projected onto a white paper at 1 m from the laser exit

The misalignment and elongated beam shape comes from the beam spatial walk-off inside non-linear crystals. Normally this effect is neglected since it keeps the parallelism between the beams and just translates the axis of the Gaussian beams. But in our case, the two beams, when injected in a microscope objective with a slight longitudinal chromatic aberration, always present, even with modern panchromatic objective, will induce a lateral mismatch near the focal point prohibitive for a perfect stimulation by the doughnut-shaped beam. Commercial SHG-SFG tandems are optimized for the best frequency conversion efficiency and therefore the walk-off effect is neglected, for this reason we have built a tandem for SHG and THG as shown on Figure 4.3 which is able to resolve the problems. It is based on a DPSS self Q-switched YAG:Nd3+ laser (SNP series, TEEM-Photonics, France) delivering 2μJ nanosecond pulses at a rate of 20 or 150 kHz corresponding to a 300 mW average power (for the 150 kHz laser). The beam waist inside the laser crystal was estimated to be 50 μm.
For the SHG non-linear crystal, instead of Lithium triborate (LiB_3O_5 or LBO), usually commercially used, we have employed a Potassium titanyl phosphate crystal ($KTiOPO_4$ or KTP) (EKSMA-Optics, Lithuania), with a moderate focusing of the fundamental beam on it in order to minimize the "gray tracking" effect . The crystal was cut for a Type II excitation ($\theta = 90°$ and $\phi = 23.5°$) which are very close to non-critical phase matching conditions at room temperature with still a good conversion efficiency. With a 1 cm crystal length and a 330 μm fundamental beam waist we obtained 20 mW of 532 nm Gaussian beam. The walk-off between the fundamental and the SHG beams was small so we were not able to measure it.
For the SFG obtained by mixing the fundamental and the SHG beams non-critical phase matching conditions cannot be reached. In addition the commercial choice is very restricted so we have to cope with a 1cm long type II LBO crystal ($\theta = 42,2°$ and $\phi = 90°$) and in order to enhance the conversion efficiency we focused the fun-

damental beam to a 100 μm waist. The beam at 355 nm has a power of 2 mW with a near Gaussian profile (M^2=1.1), and the power, profile and polarization of the 532 nm beam is not affected.

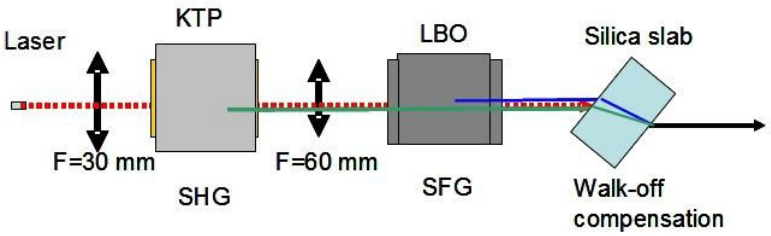

Figure 4.3: Harmonic generation by a KTP - LBO tandem. The dotted red line represents the 1.06 μm beam, the green and the blue lines respectively the 532 and 355 nm beams. Crystals are embedded in hermetic boxes to protect them from moisture. For the SHG box, the front window are is a half wave plate at 1.06 μm giving a polarization for a maximum of SHG on the KTP type II crystal, the back Windows is a Half wave plate at 1.06 μm and wave at 532 nm for a maximum efficiency of SFG. The walk off compensation is obtained by a 5 mm thick silica slab approximately at Brewster incidence.

Unfortunately this crystal introduces a small, but still measurable, lateral shift between the 355 and the 532 nm beams of 40 μm. which is prohibitive for our microscope objective. Hopefully, the large difference of wavelengths between the two beams and the spectral dispersion of refractive index of the silica allow the compensation of the lateral shift by a simple silica slab as shown in Figure 4.3. We calculated that, at Brewster incidence, a 5 mm thick slab is enough to compensate the 40 μm lateral shift between the 532 and 355 beams.

4.1.2 Dielectric mirror - an alternative to dichroic filters

In STED microscopy, the beam qualities are highly important and all the optical elements should be verified so that they introduce as little aberrations as possible. An important element of a microscope is the dichroic filter that separates the excitation and STED light from the fluorescence light. In STED microscopy the dichroics are generally 5 mm thick so that when mounted they bend as little as possible in order to avoid high order aberrations such as astigmatism.
In comparison to other STED microscopes where the excitation and the STED paths are separated and one can use a different dichroic for each path, in our particular case,

the excitation and the STED path is the same. Therefore we needed a dichroic that reflects at 45° the excitation and the STED beam and and has a good transmission in the range between these wavelengths (or the inverse). Finding such a dichroic proved to be difficult, the only option being to order a custom filter. The cost of such a custom dichroic filter were considerably high so we considered using dielectric mirros for this purpose. Dielectric mirrors are usually used in laser cavities and are optimized for certain wavelengths. The wavelengths used in our system are second and third harmonic of Nd-YAG lasers so we were able to find adequate dual-wavelength dielectric mirror called turning mirror by the producer. The reflectance spectra of the chosen dielectric mirror (Layertech, Germany) is depicted in Fig. 4.4. The reflectance at 45° for 355nm and 532nm is >99.5% and approximately 50% of the light is transmitted in the 400-480 nm band. Considering its spectral properties, the fact that it has a good flatness ($\lambda/10$) and does not change the beam properties makes it suitable for our application.

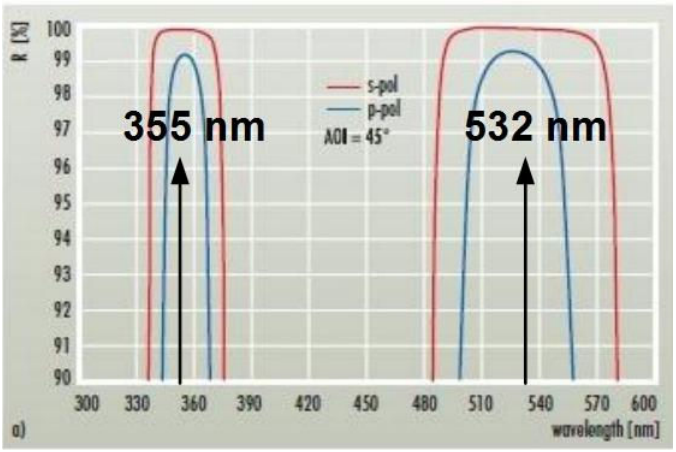

Figure 4.4: Reflectance spectra of a dual wavelength turning mirror for 355nm and 532nm, Layertec, Germany

4.1.3 Objective selection

Using excitation wavelengths in the UV range and STED wavelength in the visible implies the need of appropriate optical elements. On one side they need to have a good transmission in the UV and on the other not to cause chromatic aberrations. Among these elements, the most important in a microscope setup is the objective. The objective has to be apochromatic (corrected for three colors) and to be adapted

for the UV.
Therefore we tested several objectives by imaging onto a CCD camera the reflection on a cover slide of the two beams (355 nm and 532 nm) in order to measure the focal shift between the two wavelengths. We assumed that in the LBO crystal the waist of the two beams are in the same z position. We used the 8 kHz laser mentioned at the beginning of this chapter injected into the optical fiber. At the exit of the fiber, the laser was collimated using a F=25 mm UV-Vis lens. The adjustment in z direction was realized with the piezo-stage for a more precise measurement.
We have measured the z differences between the two wavelengths for several objectives. We will not mention the values of the z displacements since we have to keep in mind that the lenses used in the optical path are contributing as well either by increasing it or compensating it, and the entire configuration (laser and optical path) has changed several times.

In the end, our choice was the Olympus UPlanApo 60x/1.20 W with the smallest z shift among the tested objectives.

4.1.4 Detection mode - analog versus photon counting

There are two types of detectors which we could use in our set-up: photomultipliers (PMT) and photodiodes. PMTs are highly sensitive detectors of light in the ultraviolet, visible, and near-infrared ranges. Their working principle is based on the photoelectric effect and charge multiplication by secondary emission of electrons. In the multiple dynode stages of the PMT, the current produced by incident light is multiplied as much as 100 million times. The two main types of detection used with PMTs are photon-counting and analog. Our PMT (R6357, Hamamatsu, Japan) is not conceived to work in the photon counting mode (high dark count rate and slow time response). In our setup, the PMT is used in a configuration with a boxcar averager.
In the visible range, where our lasers work, the photodiodes have quantum yields 2 times higher that a PMT. Nevertheless, the photodiodes have no internal gain, except for avalanche photodiodes (APD) which have a gain of 10^2 - 10^3, which is considerably smaller than PMTs gain of 10^8. Therefore, in the case of photodiodes the only option remains the photon counting mode. For the photon counting we used an APD working in the Geiger mode (SPCM-AQRH-13-FC, Perkin Elmer, USA).
In the next paragraphs we will discuss the two possibilities. After testing the two methods we found that the best option for our application in terms of sensitivity and necessary electronics is the avalanche photodiode in the photon counting mode.

Boxcar averager

Boxcar averaging, or gated integration, is an analog measurement where the signal is averaged over a short time gate, and the results of many gates are averaged together. The boxcar averager is used for detection of noisy pulsed signals. The signal to noise ratio is improved by gating the detection and averaging over multiple pulses.
For the configuration with the 20 kHz laser it was possible to implement a commercial version of boxcar averager, whereas for the 150 kHz we have build a custom system based on sample and hold and an averaging amplifier.

The components of custom boxcar averager are the following:
- monostable multivibrator (SN7421, Analog Devices, USA) which transforms the pulse from the fast photodiode (reversed biased - used for synchronization) excited by the laser, into a TTL signal (5V) with a pulse duration close to the sampling duration (600 ns in the case of 20 kHz laser)
- sample-and-hold amplifier (AD781, Analog Devices, USA) that samples the voltage of the varying analog signal and holds its value at a constant level for a specified minimal period of time.
- operational amplifier (AD744, Analog Devices, USA) set to averaging (the cut-off frequency is set to be slightly inferior to the laser frequency, and superior to the inverse of the time between pixels) which averages several pulses.
In our case the measured fluorescence signal we detect from the sample is pulsed and has the same frequency as the excitation laser. The purpose of using the boxcar averager would be to average the fluorescence pulses in order to obtain a continuous signal with the amplitude equal to that of the averaged fluorescence signal over several pulses and connect it to an analog input of the acquisition board (E Series, National Instruments, USA).

Photon counting

Photon counting is a technique in which each individual photon is detected by a photodetector. As mentioned before, our choice of photodetector was a single photon counting module containing avalanche photodiode (SPCM-AQR-13-FC, Perkin Elmer, USA) operating in Geiger mode. The Geiger mode means that the diode is operated slightly above the breakdown threshold voltage. A single photon can trigger an avalanche current that is stopped by lowering the voltage for a short time interval, which determines the dead time. Our APD model has a dead time of 35 ns and a dark count of 250 counts/second. The quantum efficiency is around 5% at 400nm and 65%

at 650nm. The output signal of the single photon counting module is a 10 ns TTL signal that can be connected to the counter input of the acquisition board.

4.1.5 Scanning

Our choice for scanning was to use a XYZ piezo-stage (P-611.3 NanoCube®XYZ Piezo Stage, PI, USA) with the amplifier and servo-position controller E-664 NanoCube®Piezo Controller to scan the sample. The advantages of scanning the sample instead of the laser are the fact that the optical alignment is simplified since the beam does not move, no off-axis beam on the objective so that the effect of chromatic aberration is minimized. As principal disadvantage we can mention the fact that is slower compared to scanning the laser beam The resonance frequency at different loads of the piezo-stage are presented in Figure 4.10.
When choosing the type of scanning an important factor is the laser source we use. In order not to lose information we need to register a signal for each pulse, meaning every 120 μs for the 8 kHz laser source. If we assign a pulse per pixel, a 400 x 300 pixels image will take approximately 15 s. In this case, the scanning speed is limited by the laser frequency and not by the piezo stage.
For the 150 kHz laser, the repetition rate is higher, but since we cannot scan faster, we will make an acquisition every 100 μs, meaning accumulating 20 pulses for one pixel.

Unloaded resonant frequency X / Y / Z	350 / 220 / 250	350 / 220 / 250	Hz
Resonant frequency @ 30 g X / Y / Z	270 / 185 / 230	270 / 185 / 230	Hz
Resonant frequency @ 100 g X / Y / Z	180 / 135 / 200	180 / 135 / 200	Hz

Figure 4.5: Frequency response of the XYZ piezo-stage

The scanning pattern was a sawtooth wave with X the rapid axis and Y the slow one (Figure 4.6). For the Y axis we verified that the position servo-control worked good in closed-loop and the actual position was the same as the one it was set. For the X axis we had to make a compromise between the fidelity and speed as shown on Fig. 4.6. We observed a lack of linearity on the scan. Our solution was to select the

linear part for the image reconstruction.

In Figure 4.6 is represented the input scanning pattern fed to the stage (black line), the measured sensor signal without (red line) and with (blue line) the servo controller. For the X axis we have not used the servo controller since it significantly reduces the scan amplitude (thus the image size). The sensor signal was used in the image reconstruction to correct the position of the pixels in the image: we obtained at every time interval a signal assigned to a measured position but we observed in space they were not equally separated, therefore we made an interpolation to obtain a signal with equal spatial displacement corresponding to the pixel size.

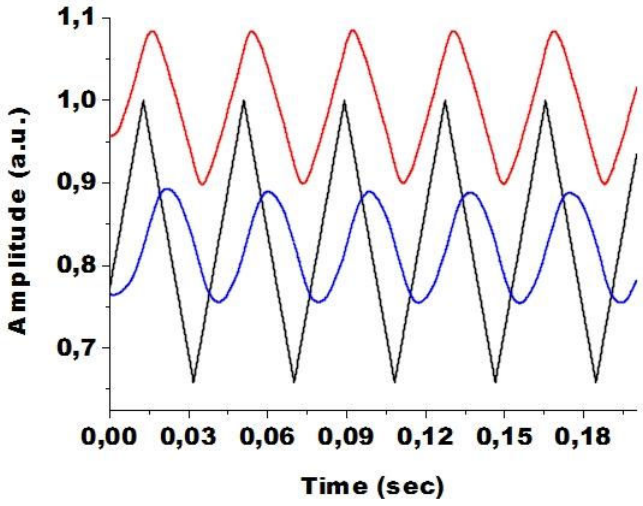

Figure 4.6: Measured stage responses:red line represents the measured sensor signal when using the piezo driver in open loop, blue line is the sensor signal when using the servo controller. Black line represents the signal fed to the stage

4.2 Segmented wave plate-beam shaping device for a simple STED setup

One of the specificity of STED microscopy is the ring/doughnut shape of the STED beam. It is known, that the resolution enhancement will strongly depend on the qualities of the beam shape, and more precisely the quality of the zero intensity point of the doughnut. In [119] it has been shown that the circularly polarized, lowest order

"dark "Gauss-Laguerre beams are the most efficient for STED microscopy.

4.2.1 Gauss-Laguerre beams

If we consider the wave equation for an electromagnetic field in free space or in a homogeneous dielectric medium:

$$\bigtriangledown^2 U = \frac{1}{c^2}\frac{\partial^2 U}{\partial t^2} \tag{4.1}$$

were U can be E_x, E_y, E_z, B_x, B_y *or* B_z. A solution for this equation can be written down :

$$U(x,y,z,t) = u(x,y,z)e^{-i(kz-\omega t)} \tag{4.2}$$

Using this solution in the wave equation will give us the paraxial approximation to the wave equation:

$$\frac{\partial^2 u}{\partial x^2} + \frac{\partial^2 u}{\partial y^2} = 2ik\frac{\partial u}{\partial z} \tag{4.3}$$

Gaussian beams are one solution to equation 4.3. When the problem has a cylindrical symmetry, the natural solutions to the wave equation are Laguerre-Gaussian beams (LG). LG beams (LG_p^l) describe a set of modes where the equation for the electric field is proportional to the product of a Gaussian and an associated Laguerre polynomial L_p^l. When l is greater than zero, the electric field has an azimuthal phase change of 2π l, which results in a phase singularity in the field and a zero point intensity in the center of the beam. They are written in cylindrical coordinates using Laguerre polynomials.

LG modes can be generated inside laser cavities [120]. Other approaches propose the generation of the LG modes outside the laser cavity: spiral phase plates (described in Section9.2), computer generated holograms-calculated interferogram between a plane wave and a Laguerre-Gaussian beam [121] [122], spatial light modulators and diffractive optics [123].

4.2.2 Beam shaping device for one source two-wavelength STED microscope

As mentioned before our goal was to build a STED microscope based on our laser source that delivers both excitation and depletion beams. Since the two beams are delivered by the same source, they are intrinsically aligned and synchronized. In order to maintain this important aspect, and not separate the two beams, we needed a beam shaping device that would create a doughnut shaped beam from the STED beam while maintaining the excitation beam unaffected.
Unfortunately, if we would use phase plates (described in Section9.2), which are most commonly used in STED microscopy to create the doughnut shape on the STED beam, it would generally have an impact on both wavelengths.
Several options have been developed to design an optical device that will act on the STED beam but will not modify the excitation beam. One method is based on diffractive optical elements [124], [125]. In an another approach annular optical elements [126] are used. The disadvantage of this method is that an important part of the STED beam is blocked.
Wildinger et al. propose in [127] a simplified STED setup with a common path for the excitation and STED beam. The wavelength selective beam shaping device is based on two optical glasses which refractive indexes match at the excitation wavelength but differ for the STED wavelength, thus creating a phase shift on the STED beam.
Another alternative is to use the polarization sensitivity of birefringent materials and change the linear or circular polarization of a laser beam into an azimuthal or radial polarization. A device working on this principle was first described in [128] and used in [129] in STED microscopy.
Our version is composed out of four segments of half-lambda wave plate for 532 nm and wave plate for 355 nm. The optical axis of the segments are oriented in a star configuration (Figure 4.7) so that the polarization of the beam is turned by 90° in neighboring segments, which will interfere destructively creating a phase singularity in the center.
This segmented low-order wave plate was fabricated by Optique de pr*é*cision J.Fichou, France. For the fabrication, a single bigger wave plate was used in order to have the same thickness for the whole assembly, the orientation of axes was $< 1°$, the distance between quadrants < 0.05 mm and the effective diameter ϕ=10 mm.

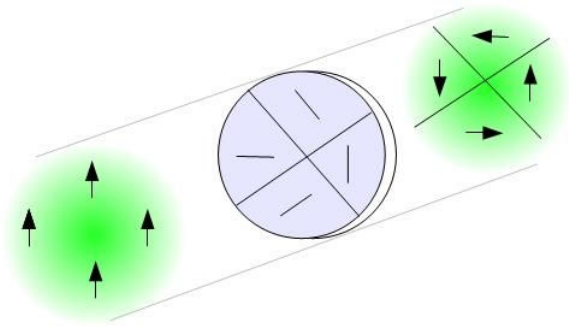

Figure 4.7: Schematic representation of the beam shaping device composed from four segments half-wave 532 nm and wave for 355 nm. Linear polarization of the beam before the segmented wave plate, azimuthal polarized LG mode

4.2.3 Direct beam imaging

Our first test of the segmented wave plate is shown in the Fig.4.8. The linearly polarized beam from a Q-switched Nd-YAG laser (Teem Photonics, France) lasing at 532 nm, was expanded and collimated through a telescope with a pinhole. The collimated beam passed the segmented wave plate and afterward was focused onto a CCD camera (Figure 4.8). A CCD image of the laser beam is represented in Figure 4.8(right). From the intensity profile we can observe that in the center of the doughnut the intensity is reduced at 1% .

The CCD images show a similar result in reference [128], where it is predicted a 75% overlap of the transmitted field with the ideal doughnut mode. It is predicted that by increasing the number of quadrants to 8 we could obtain a 87% overlap.

4.3 Single source STED microscope - final configuration

Figure 4.9 is a top view photograph of our home build Single Source Two Wavelength STED microscope. As seen from the image, the microscope's stand was custom build so that it allows the maximum flexibility in terms of optical design.

The laser source developed in our laboratory and described in Section 4.1.1 represents the basis of our STED microscope. In Figure 4.10 is represented the optical

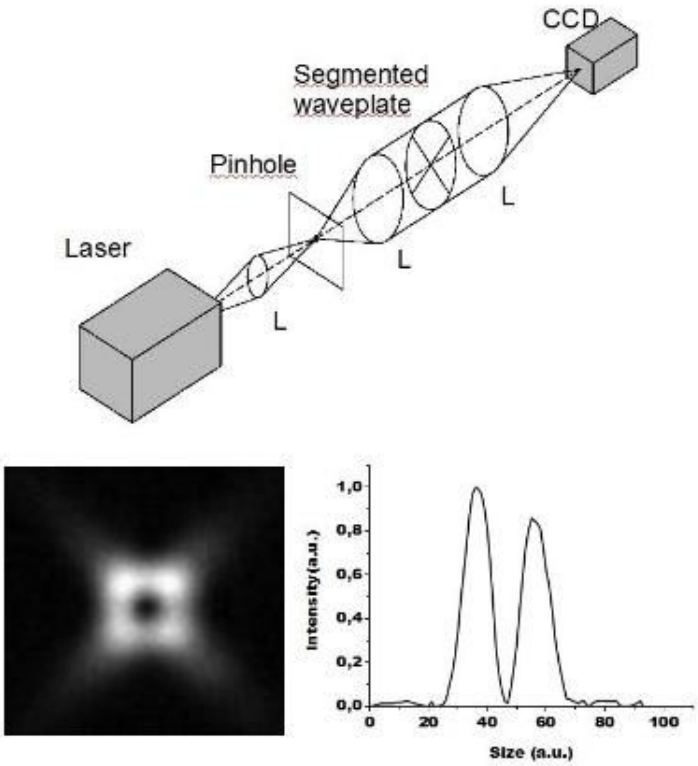

Figure 4.8: Experimental setup for laser beam imaging (top). CCD image of the laser beam and the corresponding intensity profile

design of this microscope. Its basic principle is that of a confocal object scanning microscope.
The two beams are reflected by a dual wavelength dielectric mirror for 355 and 532 nm (Layertech, Germany). To avoid any aberration caused by lack of flatness of the mirror, we chose to keep a beam of small size until after the dichroic mirror.

After the dielectric mirror, a telescope with two near-UV achromats of focal lengths 100 mm and 125 mm (L1 and L2, respectively) is inserted in the beam path to serve two purposes: first, the beams are collimated and expanded to fill the entrance pupil of the microscope objective; second, the mirror M2, on a gimbal mount, is conjugated with the pupil plane, so that it could act as a tip-tilt mirror to correct any misalignment of the beams with the optical axis of the objective. This fine adjustment proved necessary, since we observed that an angle between the beam propagation axis and the objective axis results in spatial separation of the 355 nm and 532 nm spots in

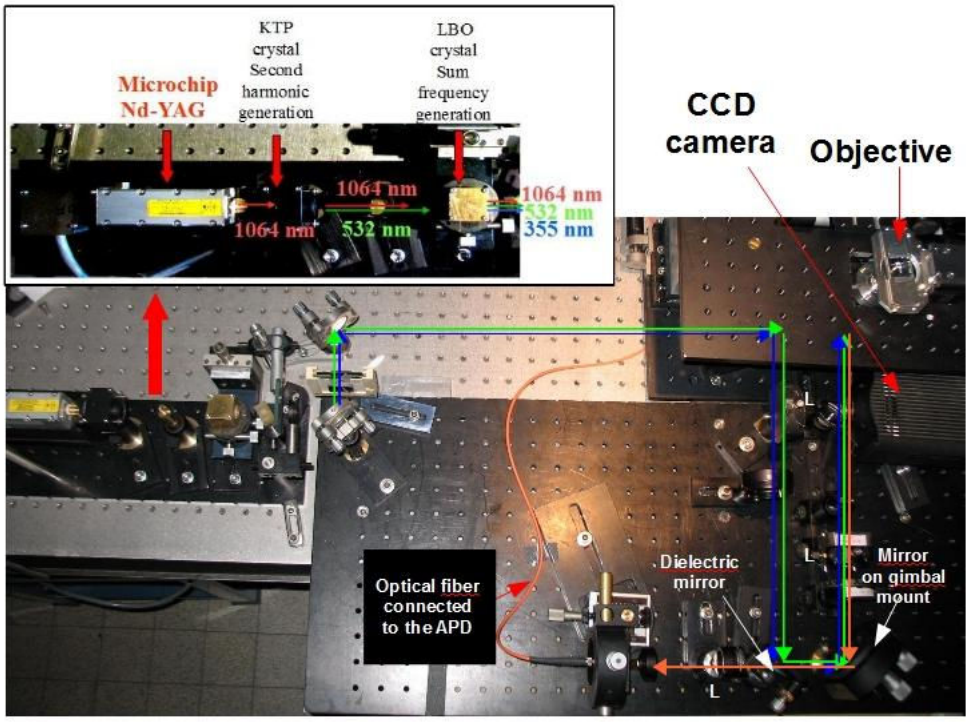

Figure 4.9: Top view of the final STED microscope setup. The home build laser source is magnified in the inset. The two beams are reflected by the dielectric mirror, afterward expanded and collimated by a 2 lens telescope and injected into the objective. Fluorescence is focused onto a multimode fiber coupled to a APD (L-lens).

the object plane. The collimated beams were focused into the sample through a water immersion objective (UPLSAPO 60XW, 1.2N.A., Olympus, Japan). The fluorescence signal from the sample is transmitted by the dielectric mirror and focused by a 150 mm focal length lens onto a multi-mode fiber serving as the confocal pinhole. The fiber diameter was chosen to be 80% of the diameter of the Airy disk. The fiber was connected to an avalanche photodiode (APD) (SPCM-AQR-13-FC, Perkin Elmer Opto Electronics Europe, Germany) operating in the counting mode. In order to discard non-fluorescent light we placed a suitable band pass filter in front of the fiber (470/100 Brightline®, Semrock, Germany) which reject both the excitation (355nm) and the STED (532 nm) wavelengths.

The laser power was controlled with a combination of half lambda wave plates (one $\lambda/2$ for 355 nm and λ for 532 nm and one $\lambda/2$ for 532 nm and λ for 355 nm) and a polarizer which renders the two beams polarizations parallel . Circular polarization

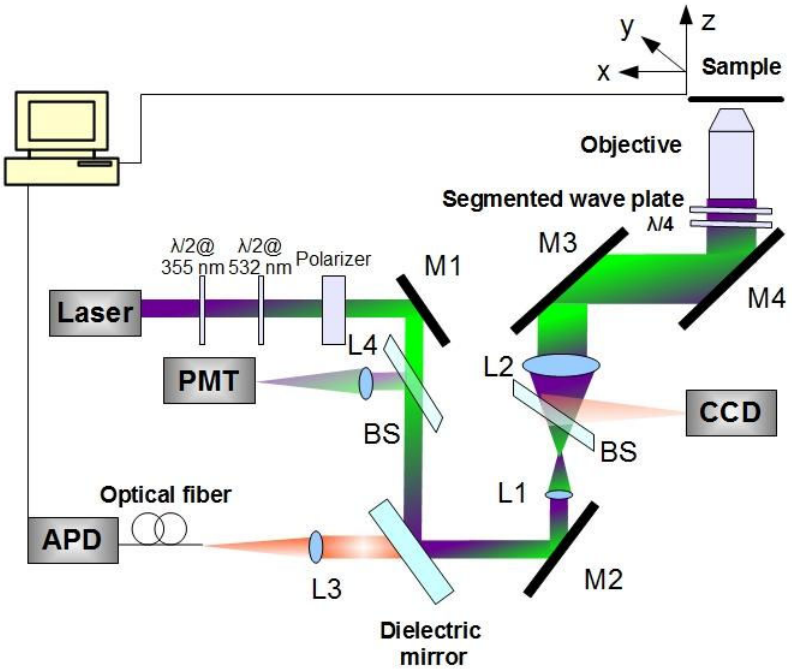

Figure 4.10: STED microscope with dual wavelength single laser source. L-lens, M-mirror, BS-beam splitter

of the beams is ensured by a quarter wave-plate placed close to the objective.

The sample was scanned with the XYZ piezo-stage across the fixed beams. The option of scanning the sample was made because the alignment of the beams with the axis of the objective is preserved. More details about scanning can be found in Section 4.1.5.

For a larger field of view we implemented a wide-field configuration based on a CCD camera. For this we placed a removable 90/10 pellicle beamsplitter between the two lenses of the telescope. The sample was illuminated with transmitted light from above from a orange-red Light emitting Diode (LED). For the fluorescence wide field imaging we illuminated the sample from below with a Xenon lamp (not shown in the scheme) with the desired dichroic mirrors and filters. Considering that the home build system was not equipped with eyepieces, the wide-field configuration was essential for focusing purposes and positioning on the desired point within the sample.

A PMT was used to detect the light scattered when scanning the gold beads. This was necessary because the signal from the gold beads was reflected by the dielectric mirror and could not be detected by the APD. Therefore, we have used another 90/10 pellicle beamsplitter on the optical path to detect the light scattered from the gold beads. A scanning image of a 80 nm gold nanobead is shown in Section 5.1.2.

A key element in the set-up is the beam shaping device which leaves the excitation beam unaffected and changes the polarization of the STED beam in such a way that it forms a doughnut shaped beam with a zero intensity point in the center [129]. Using this device allowed us not to separate the beams, so they were aligned and synchronized in all the optical path. Unlike other beam shaping devices used in STED microscopy, the device presented in this setup uses polarization engineering instead of phase engineering. This beam shaping device is described in Section 4.2. We placed the segmented wave plate into a custom holder which we fixed between the objective holder and objective so that it should be close to the objective back pupil (ensuring that the interstice between the segments would not affect the beam shape in the focal plane).

Chapter 5

Results

5.1 Fluorescent and gold bead imaging

One of the methods to determine the resolution of a microscope is to image gold/fluorescent beads with a smaller size than the theoretical resolution of the microscope so that they can be considered as point objects. We used this method to determine the microscope PSF at 355 nm and 532 as well.

5.1.1 Sample preparation

In this paragraph we present the steps we followed to prepare the fluorescent bead sample.
1. Dilute the bead solution (2% solid) to the desired concentration and sonicate 15 minutes. The typical dilution factor we used was $1 : 10^3$.
2. On a 24x24 mm coverslip put 70 μl of Poly-L-Lysine (4707, Sigma Aldrich), leave it for 2 minutes, wash it off and dry it.
3. Put 70 μl bead solution on the functionalized coverslip, leave it for 2 minutes, wash it off and dry it.
4. Mount with the required embedding medium: Mowiol or Glycerol in our case.

5.1.2 Gold bead imaging

The gold beads sample was prepared following the protocol described in 5.1.1. The STED-PSF was measured using the scattering of 80 nm gold beads [130]. In order to perform this measurement we have placed the segmented wave plate in the back aperture of the objective and scan our sample of gold beads. A confocal scanning image of the light scattered by gold beads is shown in Figure 5.1. The intensity at the center of the doughnut is reduced to 2%

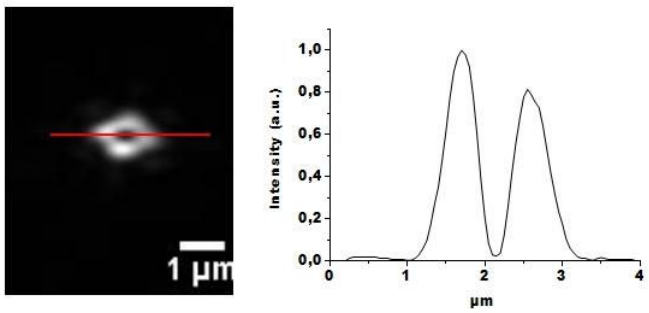

Figure 5.1: Scanning image of a 80 nm gold bead and the corresponding intensity profile

The four leaf shape of the STED-PSF is due to the four segments. A more symmetrical distribution could be obtained by increasing the number of segments but it is considered that this would not improve the resolution enhancement in STED microscopy since only the black hole in the center is important.
The 80 nm gold beads do not act as point scatterers at 355 nm, the scattering cross sections being wavelength dependent [131]. Therefore we could not obtain scanning images at this wavelength and observe the superposition of the two beams with gold beads.

5.1.3 Alignment of the excitation and STED beams

The 100 nm diameter PD-Chromeo 494 Carboxylated Nanoparticles (Chromeon GmbH, Germany), could be excited both at 355 nm and 532 nm (absorption and emission spectra shown in Figure 5.2). Chromeo 494 fluorescent beads are good objects to test the superposition of the two beams. They are have a good fluorescence efficiency both for 355 nm and 532 nm, and show a weak photobleaching. They are based on a novel polymer, which forms lattices similar to polystyrene, but with a highly reduced

oxygen permeability. Therefore the decay time and the intensity of the incorporated dye molecules are nearly independent of the oxygen concentration in the sample. For these reasons, we used these nanoparticles to verify if the two beams are correctly aligned.
We prepared the samples as described in Section 5.1.1 and used the setup described in 4.3.

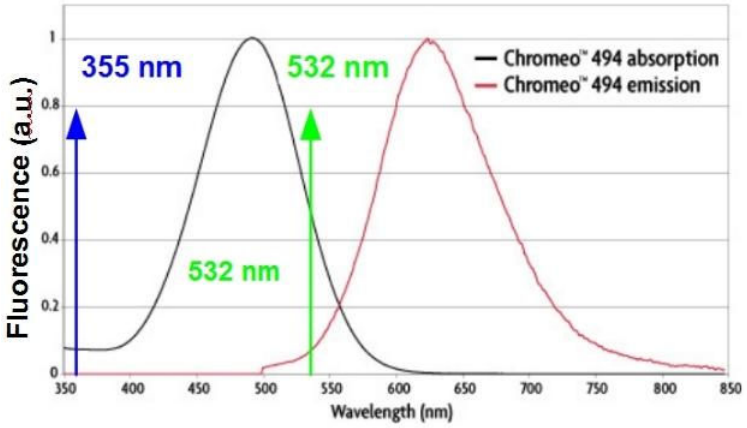

Figure 5.2: Absorption and emission spectra of *Chromeo*^{TM} 494

Before using the silica slab described in 4.1.1 for the walk-off compensation, we obtain the results presented in Figure 5.3a, where we can observe a $\approx$ 200 nm displacement between the position of the beads excited with the 355 nm beam and the position when excited with the 532 nm beam. As we can observe in Figure 5.3b, after mounting the silica slab we obtained a good superposition between the excitation beam and the STED beam.

5.1.4 Resolution improvement with Blue fluorescent beads

The Blue fluorescent FluoSpheres®beads (Invitrogen, Molecular Probes, USA) will be used for the quantification of the resolution enhancement of our STED microscope. The blue FluoroSpheres have a excitation/emission maxima of 350/440 nm and contain a blue fluorescent dye that has a high brightness and stability. We estimate that the stimulated emission cross section at 532 nm is weaker than for Coumarin 490. Nevertheless, since they exhibit a high brightness, we chose these fluorescent nanobeads as test objects for excitation at 355 nm and stimulated emission depletion

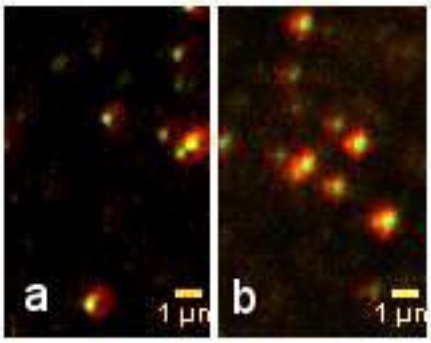

Figure 5.3: Scanning image of PD-*Chromeo*^{TM} 494 Carboxylated fluorescent beads. a) Before walk off compensation. b) After walk off compensation

at 532 nm. In confocal mode, we achieved a 200 nm resolution using these beads (Figure 5.4) which is close to the theoretical resolution (≈150nm). We observed that the actual physical size of the beads can vary (due to fabrication process and aggregation), which can complicate the analysis of the images.

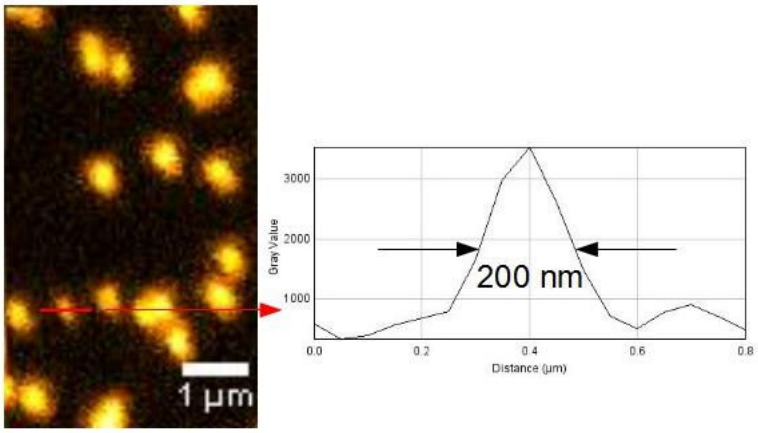

Figure 5.4: Scanning image of Blue fluorescent FluoSpheres®beads

As observed in Figure 5.4, obtaining a 200 nm resolution requires a sample without aggregates and a monolayer of fluorescent beads. Since the development of a chemical protocol to manufacture custom fluorescent nanobeads with a desired chromophore and with precise dimensions is a long and laborious process, our first purpose was to observe if we can obtain stimulated emission depletion with the commercial blue beads and resolution improvement (not necessarily "superresolution ").
With the STED microscope setup described in Section 4.3 we scanned a 6.4x6.4 μm area, with 0.05 μm per pixel and 100 μs dwell time. The average powers used: ≈0,5

μW for excitation beam, ≈5 mW for STED beam. First, we imaged the beads in the STED mode, and afterward in confocal mode, which are shown in Figure 5.5.

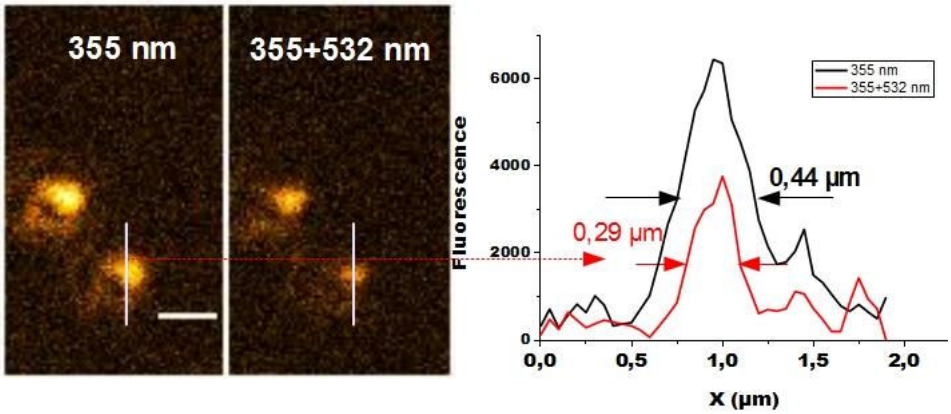

Figure 5.5: Confocal and STED images of Blue fluorescent FluoSpheres®beads and the corresponding intensity profiles of the beads. The scale bar corresponds to 1 μm. Scanned area is 6.4×6.4 μm with 100 μs pixel dwell time. The average powers used: ≈0.5 μW for excitation beam, ≈5 mW for STED beam

In Figure 5.5 we can observe a resolution improvement when using both lasers. From the intensity profiles we deduce a 20% reduction of the lateral resolution. Nevertheless, we do not obtain a resolution that overcomes the diffraction limit. Several reasons will be discussed further.

The two lenses used to expand and collimate the beam in the Single source STED microscope are Near-UV (NUV) Achromatic Lenses (Edmund Optics, USA) with >90% transmission from 360-700nm, >50% transmission at 334nm and feature a simple cemented design. Despite their achromatic design, these lenses have a focal shift of 40 -80 μm between 355 nm and 532 nm. A more important contribution to the difference in the focal point for the two wavelengths has proven to be due to the objective lens (≈2 μm).
Therefore, the chromatism of the lenses accumulated with the important chromatism of the objective (in some cases the lenses can slightly compensate the objective's focal shift), will induce a shift of the focus point of the two wavelengths. Due to this fact, the axial PSF of the excitation and STED beam will not be perfectly superposed which will affect the resolution improvement.

An example of focal shift of the two wavelengths and the effect on the resolution improvement is shown in Figure 5.6. At z=0 μm we measure the best resolution im-

provement, but the excitation image seems not to be at the focal point. If we change the z position by 0.2, then by 0.6 μm we can observe that the excitation image seems to be at a better focus but the resolution improvement in the STED image is weaker.

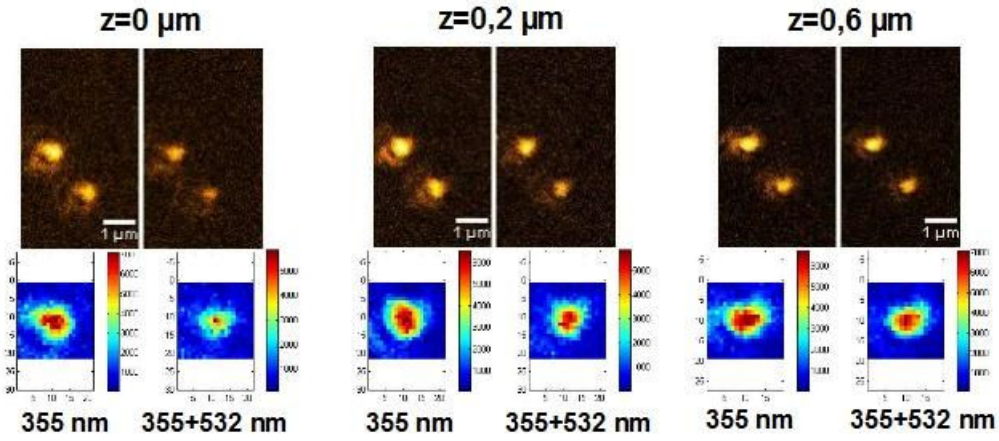

Figure 5.6: Scanning images of Blue fluorescent beads taken at different z positions in the confocal (355nm) and STED mode (355+532 nm)

Future work

We believe that the best solution for solving the problem of the focal shift is to build the setup without using lenses and possibly reflective objectives [1] which are well suited for applications that require chromatic correction over broad spectral ranges. Our future work will consist in optimizing the fiber coupling of the laser and using off-axis parabolic mirror on the optical path instead of achromatic lenses.

5.2 Fluorescence Correlation Spectroscopy (FCS) and STED

In this section we present our Fluorescence Correlation Spectroscopy (FCS) measurements made with the set-up described in Chapter 4. The purpose of these measurements was to have a confirmation of the microscope performances and another way to quantify the volume reduction when applying the STED beam.

[1] $http://www.edmundoptics.com/microscopy/reflective-objectives/$

5.2.1 Principle

FCS is a sensitive technique that analyzes the small fluctuations of the fluorescence intensity. In most cases FCS is used in confocal microscopes as shown in the left hand-side of Figure 5.7.
FCS has numerous applications since an important number of processes can be interpreted with the help of intensity fluctuations. It is a very sensitive technique used to describe diffusion, transport, photo-physical processes quantitatively [132]. The most important applications are in biology, because FCS can provide information about the smallest functional units in biological units such as proteins and nucleic acids. FCS measurements are used in the study of biomolecular associations and dissociations [133], [134], [135], studies of cell membranes [136], [137] offering information about protein concentrations and dynamics. The two results provided by FCS are roughly the concentration (or number of molecules N) and the mobility (diffusion time). Both are contained in the autocorrelation function G. The normalized autocorrelation function is described by:

$$G(\tau)=1+\frac{\langle \delta F(t)\delta F(t+\tau)\rangle}{\langle F(t)\rangle^2} \tag{5.1}$$

where F is the fluorescence signal and $\delta F(t)$=F(t)-$\langle F(t)\rangle$ is the fluorescence fluctuation

If we consider that the observation volume has a 3D Gaussian geometry with lateral width ω_r and axial waist ω_z (depicted in the left hand side of Fig. 5.7), G can be expressed by 5.2 for the free 3D diffusion.

$$G(\tau) = 1 + \frac{1}{N}\left[\left(1+\frac{\tau}{\tau_D}\right)\sqrt{1+\frac{\tau}{S^2\tau_D}}\right]^{-1} \tag{5.2}$$

where

$$\tau_D = \omega_r^2/4D \tag{5.3}$$

where D is the diffusion coefficient.

Therefore, when changes in the fluorescence are measured in time, these data provide information that can be used to determine diffusion coefficients, rate constants and sample concentrations; aggregation and dynamics linked to rotation and translation are also of interest and can be studied in this manner [138].

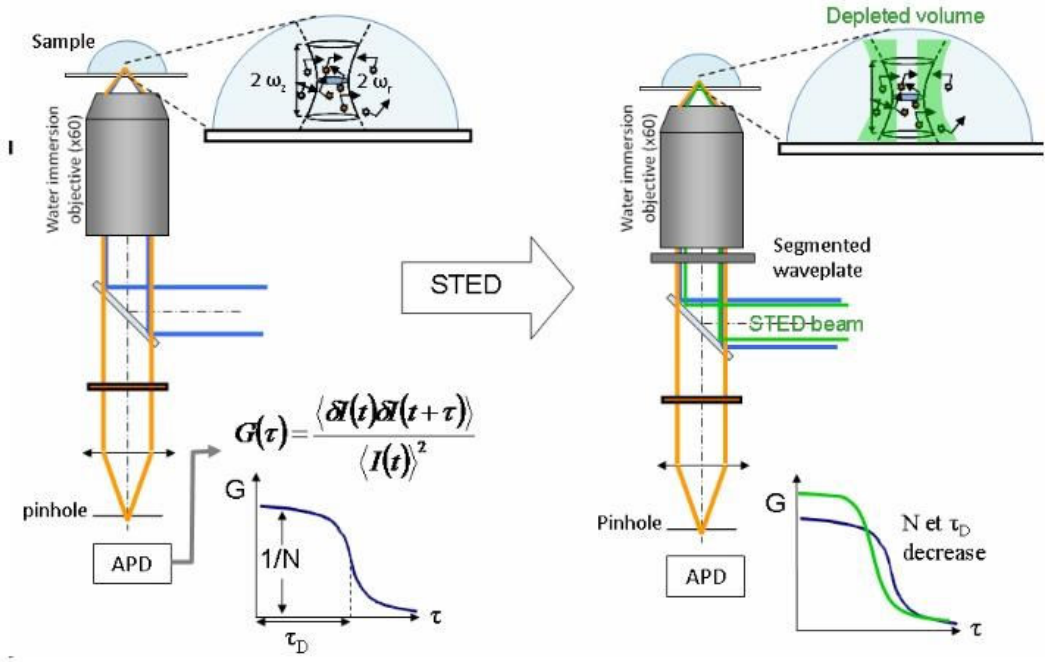

Figure 5.7: Experimental setup for FCS confocal (right) and FCS-STED (left)

The combined method FCS-STED has been reported for the first time in 2005 by Kastrup et al. in [139].
Our main purpose in this section was to do FCS measurements on our single source dual-wavelength STED microscope in order to observe the modification of the excitation volume. The principle is shown in Figure 5.7.
From equation 5.2 we deduce that at constant fluorophore concentration, N scales linearly with the size of the observation volume. In STED microscopy the excitation volume is reduced and it is no longer diffraction limited, therefore N should decrease as well. When using the STED beam, the observation volume along the lateral directions is reduced. Consequently τ_D will decrease.

5.2.2 Constraints

When doing FCS measurements on the microscope set-up described in Chapter 4 we will have to take into account a series of parameters.
i) The diffusion time τ_D must have a higher value than the time interval between laser pulses 1/150 kHz=6 μs which defines the maximum temporal resolution of the fluctuations that can be detected.
ii) The UV power at the back aperture of the objective is maximum 0.5 μW. If we calculate the brightness of a a small molecule such as Coumarine 490 at this power (count rate per molecule (CRM)=count rate/number of molecules) we notice that it is less than 0.1 kHz. Since in FCS the CRM determines the signal to noise ratio, we deduce that such a value is not sufficient for FCS measurement. Brighter objects are required. Therefore, for the measurements done with this set-up we need to use "objects" such are particles concentrating many molecules.

The best option was to use the 0.1 μm blue (350/440) fluorescent beads (Invitrogen, FluoSpheres Microsphere) which we have used in the microscopy applications and have a good absorption around 355 nm and 20% emission at 532 nm. They combine the advantage of a slow diffusion (due to their large size) and a high brightness.

5.2.3 Results

We have made a 20x dilution of the stock solution of FluoSpheres Carboxylate-Modified Microspheres, 0.1 μm, Blue Fluorescent (350/440), 2% solids.

We recorded five traces of the fluorescence signal lasting 10 s each. The autocorrelation of these five measurements was calculated, then averaged to yield a mean autocorrelation function and the associated SEM (standard error of the mean) was calculated for the five acquisitions. By doing so, the data points with large uncertainties are not as much considered in the fit as data points with small ones. In Figure 5.8 are presented the average of the autocorrelation curves obtained: with the 355 beam (black line) and with the 355 and 532 nm (blue line) and the corresponding fits.

From the autocorrelation curves we have deduced a $\sim$ 28% decrease of the diffusion time τ_D when applying the two beams simultaneously. We further used the expression 5.3 to obtain the radial waist ω_r^2. In the case when we applied at the same time the 355 nm and the 532 nm beam we calculated a $\sim$ 15% reduction of the radial

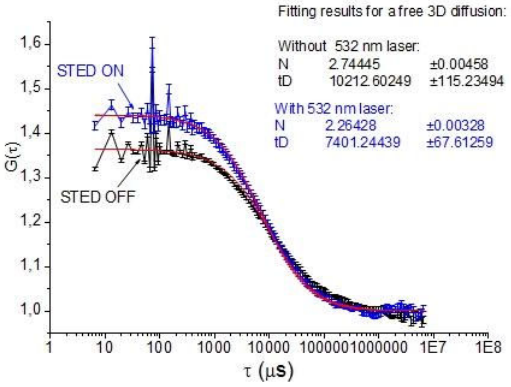

Figure 5.8: Autocorrelation functions resulting from an FCS-STED experiment with(blue) and without (black) the STED beam. The corresponding fit parameters N and τ_D are given in the inset

waist ω_r^2.

As a conclusion we can say that in our first test of FCS-STED we obtained a volume reduction of the focal waist which indicates that with our STED set-up we could obtain smaller excitation spots when using the two beams. However, the volume reduction is limited, probably due to chromatic aberrations, as already observed for imaging (5.1). Therefore, the waist ω_r does not decrease much since the intensity of the depletion beam is not high enough.
As we can observe from Fig. 5.8, the quality of the fits to the measured autocorrelation functions is good, but the reproducibility of the autocorrelation curves is limited by the aggregation of the beads. As a conclusion, FCS measurements confirm that in the STED configuration the size of the PSF is reduced, by a factor that is in agreement with the results obtained in the imaging experiments.

Chapter 6

Conclusions and perspectives

6.1 Achieved results

In this part of the thesis we have presented the process of development of a simplified STED scheme based on an original laser source that emits simultaneously 355 and 532 nm sub-ns pulses. The UV beam is used for excitation of the fluorophores and the green beam shaped as a doughnut with a zero intensity point in the center induces stimulated emission depletion.
We have started our work by describing the processes of excitation and stimulated emission depletion using sub-nanosecond lasers. In our case, the laser source is particular, by the fact that the two pulses are intrinsically synchronized and aligned, the pulse length is not common for STED application and there is no temporal delay between the excitation and the STED beam. Taking into account these differences, we have made an analytical description and performed numerical calculations to describe the excitation and stimulated emission using our custom laser source. We observed that in the case of our nanosecond pulsed laser the depletion efficiency does not follow the exponential law described in most STED configurations. As described in Chapter 2, for a moderate STED power, the depletion efficiency follows a power law. One important point is that compared to CW lasers, when using our laser source the average power required is lower by a factor of 5.10^4. Therefore, considering the characteristics of our laser and the corresponding calculations, we can say that our laser represents an interesting laser source for STED microscopy.

We further continued our study to find the most suitable dyes that can be used in combination with our custom laser source. In order to accomplish this, in Chapter 3 we have developed a method that allowed us to compare different compounds in terms of STED efficiency in a concentration-independent manner. We have tested different dyes such as Coumarin 490, Hoescht 33342, BF3 and NADH.
In Chapter 4 we describe the experimental microscopy setup we have built. We describe all the important steps we have followed until we found the best configuration presented in the last section of the chapter. In principle the optical design of our setup is that of a confocal scanning microscope with a custom stand which allowed the maximum of flexibility concerning the optical path. The microscope we have built is adapted to the use in the UV range and in confocal mode with 355 nm excitation we obtained a 200 nm spatial resolution. One important aspect we describe in this chapter is the beam shaping device that allowed us not to separate the two beams creating the doughnut shape only on the STED beam and not on the excitation beam.
The last chapter is the Results part and it is divided into two main sections: in the first section we present our microscopy results and the second part presents the FCS results. In the microscopy part we have not obtained a resolution that exceeds the diffraction limit due to chromatic aberration. Nevertheless we have obtained a volume reduction when applying the STED beam, which indicates that if the chromatic issues are solved the microscope has real potential of obtaining superresolution. In the FCS part we had a confirmation of the results obtained in the microscopy section, obtaining the same $\approx$20% reduction of the excited volume.
In this part of the thesis we presented the entire process of the development of a simplified STED microscope based on a original bi-color laser source. We believe that even though the superresolution has not been proven in this present work, microchip dual color lasers are promising sources for STED microscopy. The simple optic design and the low-cost of the microscope setup make this setup an interesting option in microscopy. One interesting point is the particular wavelengths for excitation and stimulated emission which match the spectral properties of the coenzyme NADH that is of particular biological interest since this endogenous molecule has essential roles in cell metabolism and is frequently imaged with 350 nm-excitation.
The present setup would need to be modified to achieve superresolution.
In the microscope part the next step is to remove all the lenses in the optical path and use parabolic off-axis mirrors. Also in the place of the objective lens, we will test the reflective objectives which is said to be high magnification solutions to applications in the ultraviolet, visible, or infrared. These objectives are used in microscopy applications that require chromatic correction over broad spectral ranges.

The most important development we plan is to build a STED-Selective plane illumination microscope (SPIM) based on our laser source. The details of this concept and preliminary tests are presented in the next section.

6.2 Possible developments

During our studies and measurements of fluorescence quenching in dye solution we have developed an idea of a potential demonstration of resolution improvement by the STED effect. We aim at improving the axial resolution in a SPIM experiment [140] using our two-color microchip laser source. In SPIM (a more general term is Light Sheet Fluorescence Microscopy-LSFM), the sample is illuminated along a separate optical path orthogonal to the detection axis [141]. The light sheet is either produced by a cylindrical lens or by scanning the beam in one direction. The working principle of SPIM is depicted in Fig.6.1. The light sheet thickness determines the axial resolution and can be improved by tightly focusing the excitation beam. But this is at the cost of a narrower field of view, since, according to light diffraction laws, the beam Rayleigh length dramatically decreases with focusing power. In [142] the best lateral resolution obtained in a SPIM microscope with a 700 nm laser was $\approx$0,6 μm and 2 μm for the axial. An improved resolution of SPIM has been reported by using structured illumination techniques (SIM) [143]. SPIM can also be combined with techniques, like FCS to allow spatially resolved mobility measurements of fluorescing particles inside living biological samples [144, 145]. In [146] the authors have designed a widefield frequency domain Fluorescence Lifetime Imaging Microscopy (FLIM) setup, which is based on a SPIM.

The integration of STED in a SPIM was first reported in 2011 [147] where a 60% improvement in axial resolution was obtained. Also the STED-SPIM concept is presented in a patent from 2012 [148]. The STED-SPIM method is at its beginning and we believe that further improvements are possible.
We believe that our laser source could be interesting for a STED-SPIM setup since the fluorescence quenching is obtained at low average powers compared to CW STED as shown in a previous paragraph. Therefore, the axial resolution improvement is expected to be larger than the one obtained in [147] where a CW laser was used. Also since SPIM does not require laser scanning to acquire an image the low repetition frequency of the laser is no longer a limitation for the imaging speed.
The experimental set-up we have built to make the proof of principle of this method

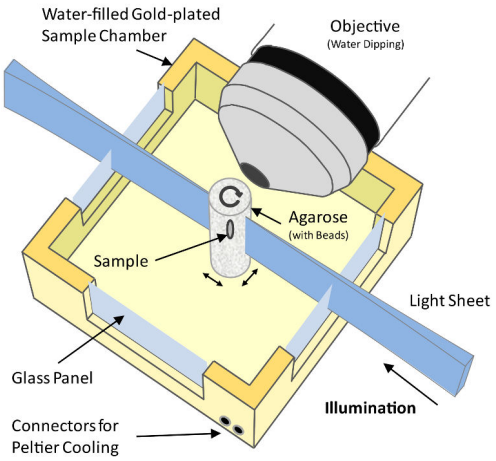

Figure 6.1: Schematic drawing of a Selective Plane Illumination Microscope. Source:http://www.en.wikipedia.org/wiki/Wiki

is showed in Fig.6.2. The scheme of the setup is similar to the one used for measurements in dye solution in Chapter 3. The main difference is that we added the segmented plate that creates the doughnut shape on the 532 nm (Section 4.2) and a quarter wave-plate to render the polarization of the beams circular. The used fluorophore was a solution of Coumarin 490 in ethanol.

The first results are showed in Fig.6.3. In one image only the UV pulse is focused in the spectrometer cell (Fig.6.3a) and in the second we added the green pulse (Fig.6.3b). One thing we notice is that in our setup the Rayleigh length is bigger due to spherical aberrations, so we will use the term "pseudo-Rayleigh length" to refer at the propagation distance.

We plotted the profile (red line) in the two cases (Fig.6.3c) and we could clearly observe the thinning of the waist of the beam in the case when using both laser pulses. A reduction of approximately a factor 3 of the beam waist is obtained by the STED effect. This is very encouraging since the best result obtain in [147] was a 60% improvements in axial resolution. Another important aspect is the Rayleigh length which define the field of view in SPIM: we measured how the "pseudo Rayleigh length" is affected by STED by plotting profiles at different distances from the beam entrance into the cell (Fig.6.3d). We notice that despite the thinning of the waist of the beam, the "pseudo-Rayleigh length" is not shortened, as it would have been if the beam had been focused more tightly. On the contrary, the STED effect extends the usable range of the beam. This is advantageous for SPIM applications since both the axial resolution and the

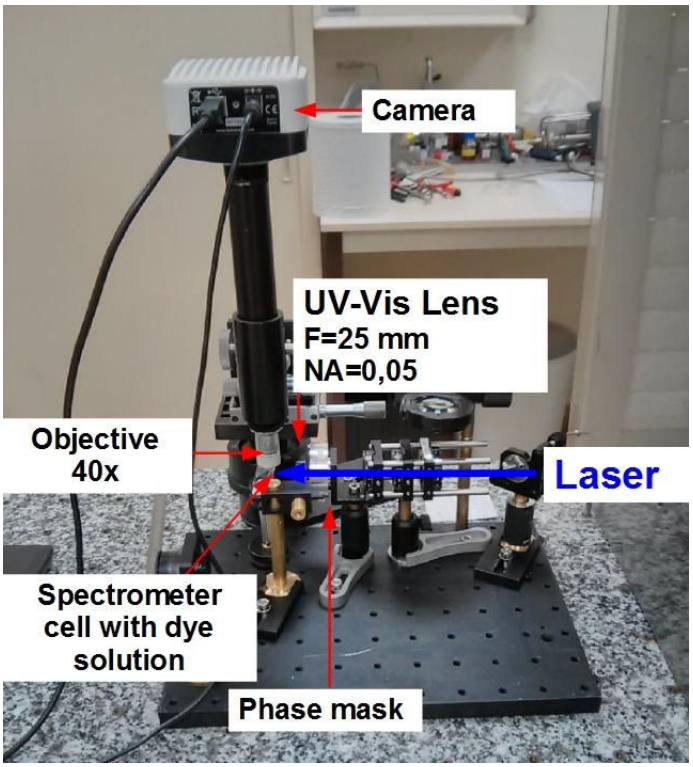

Figure 6.2: Photograph of the experimental setup for the STED-SPIM demonstration of the proof of principle

field of view are improved.

As in the case of microscopy we noticed that the system is affected by chromatic aberrations in the focusing lens. Nevertheless, we think that they will be less important that in the case of microscopy applications since the beams do not need to be focused as tightly. As mentioned in Section 5.1 a solution to avoid the chromatic aberrations will be to use parabolic off-axis mirrors.
With this preliminary results we show that combining STED with SPIM result in significant improvement of two aspects: the STED beam causes the thickness of the fluorescent region to be reduced and maintained constant over a longer propagation distance ("pseudo-Rayleigh length"). Therefore, SPIM-STED microscopy offers a better optical sectioning and a wider field of view and our microchip laser seems to be a promising choice for this application.

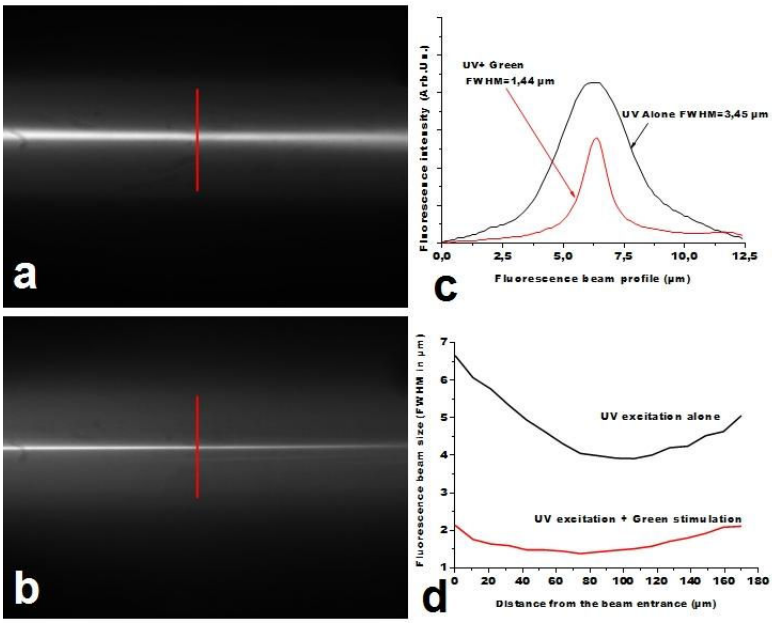

Figure 6.3: CCD images of the fluorescence obtained by with the setup from Fig.6.2 focusing the UV pulse (a) and both UV and green pulses (b). Corresponding intensity profiles of the beam waists (Fig.6.2c): UV pulse (black line) and UV and green pulse (red line). Plot fluorescence FWHM size as a function of axial position (showing the pseudo Rayleigh length) in the case of UV excitation (black line) and in the case of UV excitation and green fluorescence quenching (red line)

Part II

Single wavelength for two-photon excitation and stimulated emission depletion in STED microscopy

Chapter 7

Principle

7.1 Introduction

The principle of STED microscopy has been well explained and detailed in the first part of the thesis from where we have understood the main advantages of the method as well as its drawbacks. It is discussed that, in STED microscopy the main difficulties arise from the complexity of the experimental setup that requires in most cases two laser sources that need to be perfectly aligned and synchronized. As we have underlined and observed experimentally in the first part of this work, a major issue related to the laser sources is the fact that they have different wavelengths that could cause chromatic aberrations which makes it difficult to focus and perfectly overlap all the beams in the microscope focal plane. In microscopy, the objective lens is the most important optical unit that determines the basic performance of the microscope. Despite the advancement in their design, objectives are susceptible to chromatic aberration. The best objectives are the apochromat objectives for which the axial chromatic aberration of three colors are corrected. Nevertheless, in STED microscopy we use two to several wavelengths, and no objective lens can correct for all wavelengths. As we have observed in the first part the chromatism of the objective lens can greatly influence the performance of the microscope.
As a consequence, in this work we present our idea and its practical implementation that could avoid these problems and in the same time simplify the setup. The main idea is to use only one wavelength originating from the same laser source for both

two photon excitation and for one photon depletion. In this configuration the laser source is a femtosecond pulsed Ti-Sapphire laser that is split into two optical paths: one for two photon excitation and the other for stimulated emission after the pulse is stretched. This technique will be named SW-STED, for single wavelength stimulated emission depletion. We believe that such a concept implemented in a Two Photon Excitation (TPE) microscope will bring the higher resolution afforded by STED without having to add another laser source

TPE microscopy is now a widely used microscopy technique used in particular in biological applications. In comparison to confocal microscopy, the excitation light is red-shifted, which allows deeper penetration into scattering tissues. TPE is a non-linear process, where the excitation depends on the square of the light intensity , therefore confining fluorescence to the focal spot. This reduces photobleaching and phototoxicity outside the focal plane and allows optical sectioning. Therefore, TPE is a high resolution three dimensional microscopy technique with reduced photodamage.

The combination of TPE and STED techniques has already been reported [60], [149], [150]. However, till the moment our results have been published, the studies reporting TPE-STED combination use two laser sources to produce different wavelengths. As mentioned in [60], the merging of TPE with STED microscopy limits the choice of suitable light sources for applications, due to the high peak-power required for both excitation and depletion. For the moment the best choice is a mode-locked fs laser for excitation and an Optical Parameter Oscillator (OPO) for the STED beam. This combination of light sources is not only costly but also difficult to operate. As it has been pointed out in a recent patent [151], by using a single wavelength for both two-photon excitation and stimulated emission depletion, SW-STED would provide a significant simplification to the technique. It would solve the problems related to laser pulse synchronization, thermo-mechanical drifts of independent sources and achromatism of microscope objectives and wave-plates, since the two laser beams come from the same laser and have the same wavelength. Moreover, as only one wavelength has to be filtered out prior to detection, fluorescence signal collection is also simplified.

After the publication of this work, an article by Diaspro and al. [61] using the same principle as ours has shown subdiffraction resolution images of microtubules immunostained with the dye ATTO647N. Therefore, it confirms the real interest of this type of microscope.

In the first phase of this work we explained the principle of SW-STED. The next phase was to make the proof of principle in a dye solution. The dye we have chosen is called DCM (4-dicyanomethylene-2-methyl-6-p-dimethylaminostyryl-4H-pyran) [152] and it is a known laser dye with quantum yield of 0.80, high two-photon absorption cross-

section and a large Stokes-shift. Using the experimental data we have obtained in solution, we have performed numerical simulations to determine the efficiency of the fluorescence quenching and to predict the performances of a microscope based on this concept. We further continued our work in making the first attempts in microscopy applications.
Part of this work has been published in [153].

7.2 Theory

For a better understanding of the working principle of SW-STED, in this section we make an introduction into the photophysics of two photon excitation and stimulated emission depletion. In Fig. 7.2 is represented the Jablonski diagram in the case of two-photon absorption and STED process. The dye molecule is excited from the low vibrational levels in the S_0 ground state by the simultaneous absorption of two photons, followed by rapid relaxation to lower vibrational levels in excited singlet state S_1. Without external perturbations, the population in S_1 decays by spontaneous emission and fluorescence can be observed. Here a second laser pulse is sent to induce stimulated emission and dump the population in S_1 to the upper vibrational levels of S_0 before fluorescence emission can occur.

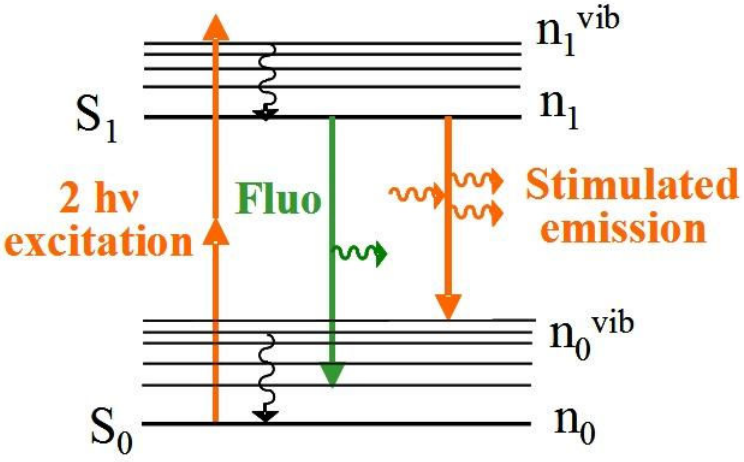

Figure 7.1: Energy levels and optical transitions involved in SW-STED.

This configuration arises two issues.
One issue is whether the fs pulse that is used for two photon excitation of the fluorophore, could cause stimulated emission. This event is highly improbable because

stimulated emission can only occur from the low vibrational levels of S_1 and a delay of ≈1 ps (represented by τ_{vib}) is needed for an excited molecule to relax to these levels. Therefore the fs pulse is too short to induce stimulation. That is the reason why we wrote only I_{pico} in Eq.7.2 and 7.3.
The second issue is the probability that the picosecond pulse used for stimulated emission could cause two photon excitation. This is the reason for the presence of the term I_{pico} in Eq.7.1 and 7.4. In order to avoid as much as possible the excitation caused by the ps pulse we will increase the duration of the pulse which will cause a decrease of the two photon excited probability (which depends on the instantaneous intensity). By stretching the pulse duration the rate of the stimulated depletion will not change.
In this study we will ignore the anisotropy of the population created by the polarized excitation and depletion pulses, which will considerably complicate the problem. The polarization effect has been studied in [106] and [154] and it is known that it affects the depletion efficiency. As we have mentioned in the first part, the depletion efficiency depends on: a) the viscosity of the solvent, which controls the speed of reorientation of excited molecules; b) the delay between the excitation and stimulation pulses and c) the angle between the polarizations of the excitation and STED beams. The best efficiency is obtained when the polarizations of exciting and depleting beams are parallel and when the delay is short and the viscosity sufficiently high to prevent molecular reorientation.
Equations 7.1-7.4 are describing the population evolution in the four levels depicted in Fig.7.2. We have made the following notations: n_0 and n_1 are the populations of the low lying vibrational levels of S_0 and S_1 respectively; n_0^{vib} and n_1^{vib} refer to the upper vibrational levels of the same states; σ_{TPA} and σ_{STED} are the two photon absorption (TPA) and the stimulated emission cross section respectively; τ_{rad} and τ_{NR} are the radiative and non radiative relaxation times of the emitting singlet state; τ_{vib} is the rapid vibrational relaxation time which is assumed to be the same for the ground state and the excited state (this assumption is justified by the fact that it is much faster than the other considered processes). Finally I_{femto} and I_{pico} are the intensities of the fs pulses and the stretched pulses respectively. These two pulses are not temporally overlapped: the stretched pulse arrives on the sample approximately 100 ps after the fs pulse.

$$\frac{dn_1^{vib}}{dt} = \sigma_{TPA}(I_{femto}^2 + I_{pico}^2)(n_0 - n_1^{vib}) - \frac{n_1^{vib}}{\tau_{vib}} \tag{7.1}$$

$$\frac{dn_1}{dt} = \sigma_{STED} I_{pico}(n_0^{vib} - n_1) - n_1(\frac{1}{\tau_{rad}} + \frac{1}{\tau_{NR}}) + \frac{n_1^{vib}}{\tau_{vib}} \tag{7.2}$$

$$\frac{dn_0^{vib}}{dt} = \sigma_{STED} I_{pico}(n_1 - n_0^{vib}) + n_1(\frac{1}{\tau_{rad}} + \frac{1}{\tau_{NR}}) - \frac{n_0^{vib}}{\tau_{vib}} \tag{7.3}$$

$$\frac{dn_0}{dt} = -\sigma_{TPA}(I_{femto}^2 + I_{pico}^2)(n_0 - n_1^{vib}) - \frac{n_0^{vib}}{\tau_{vib}} \tag{7.4}$$

These equations are similar to the formulation in [40]. However, since the excitation is induced by a two photon absorption process, its probability depends on the square of the intensity. Nevertheless, our configuration is particular since both excitation and depletion are produced by the same laser source and there is a probability that the STED (femto) pulse would induce two-photon excitation.. Taking into account all the aspects mentioned above and assuming that the stimulated emission is much more efficient than spontaneous emission and if we assume that the depleting pulses are sufficiently stretched in order to avoid any two photon excitation (this assumption will not be made in the numerical simulation), as in [155] equation 7.2 is reduced to:

$$\frac{dn_1}{dt} = \sigma_{STED} I_{pico} n_1 \tag{7.5}$$

Therefore, as in the majority of STED studies the quenching of fluorescence follows an exponential law:

$$n_1 \propto e^{-\sigma_{STED} I_{pico} \Delta t} \tag{7.6}$$

where Δt is the duration of the picosecond pulse.

Later in this work we present numerical calculations in order to better understand the fluorescence quenching behavior in our case and in particular, determine from which level of intensity, it is no longer valid to neglect reabsorption effects caused by the stretched STED pulse.

Chapter 8

Experimental setup

The principle of SW-STED and its advantages compared to other systems has been detailed in the previous chapter. A microscope based on this idea would be highly interesting by combining the advantages of TPE microscopy with the superresolution of STED microscopy. In this chapter we present the experimental setup and the various issues we have considered when building it. At the beginning we present the characteristics of the dye we have chosen to use in our demonstration. Afterwards we describe the experimental setup we have used to determine the depletion efficiency in dye solution. In the end we describe the custom microscope we have built.

8.1 DCM dye

In STED microscopy the use of highly fluorescent dyes with a large Stokes-shift is one important condition in order to ensure that the stimulation beam does not induce one-photon absorption. Besides, we have to take into account the efficiency with which the dye molecules are de-excited when the STED beam is applied. In our particular case, larger Stokes-shifts are required since the same wavelength is used to generate two-photon transitions, so the stimulation wavelength should be close to twice that of the linear absorption peak. Moreover, efficient two-photon absorption cross-sections are desirable. Therefore, the choice of dyes for our system will be more difficult. With the system described in this chapter we have tested several dyes from

Exciton from the pyridine family: Pyridine 1 (LDS 698)), Pyridine 2 (LDS 722)), styryl family: Styryl 8 (LDS 751)) and pyran: DCM (LC-6500). The results we have obtained with all the above mentioned dyes, except DCM, were not very promising, therefore the majority of our experiments were performed with the DCM dye.
DCM (4-dicyanomethylene-2-methyl-6-p-dimethylaminostyryl-4H-pyran) is a very efficient dye used as a lasing medium because of its high efficiency, large Stokes shift and wide tuning range [152]. This is the reason why its photophysical properties have been widely studied [156]. The chemical structure and formula of DCM are shown in Fig. 8.1.

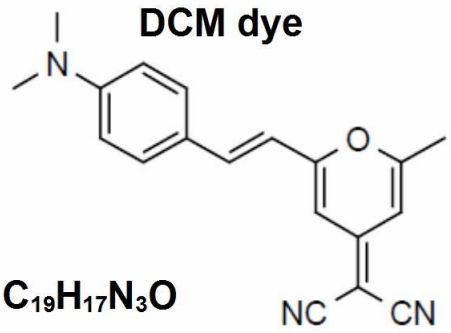

Figure 8.1: DCM laser dye: chemical formula and structure

DCM is a small molecule with a donor-acceptor structure and high capacity of photoisomerisation [156]. As we can observe from the absorption and emission spectra in Fig. 8.2 DCM has a big Stokes shift ($\approx$ 150 nm) and in [157] it is shown that fluorescence is red shifted in solvents of increasing polarity of DCM. The best solvent for DCM is Dimethyl sulfoxide (DMSO) with a quantum yield of 0.80 and a fluorescence lifetime of 2.18 ns [152]. In Methanol it has a quantum yield of 0.43 and a fluorescence lifetime of 1.31 ns [152]. We have generally used DMSO as a solvent. DMSO was a good choice also because it has no absorption band in the range of our excitation wavelengths, preventing thus thermal lensing effect.

The TPA cross section spectrum for DCM was determined in the spectral range from 680 nm to 1000 nm by upconversion fluorescence measurements using a Ti:Sapphire fs laser. The fluorescence, collected at 90° to the excitation beam, was focused into an optical fiber connected to an Ocean Optics S2000 spectrometer. The incident beam power was adjusted to 50 mW. We checked that, at this power level, the fluorescence signal depends on the square of the intensity over the whole spectral range, confirming that two-photon excitation is the dominant process. Calibration of the

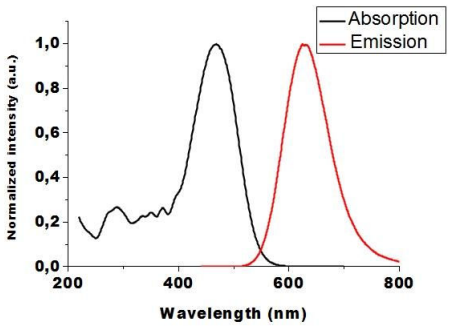

Figure 8.2: DCM absorption (black line) and emission (red line) spectra in Methanol

two-photon absorption cross section value was performed by comparison with the published Coumarin-307 and Rhodamine TPA spectra [158].
The measured two-photon absorption and fluorescence emission spectra of the DCM dye are shown in Fig. 8.3. Our experiments were performed at 680 nm and 700 nm, near the edge of the tuning range of our laser(mode-locked Ti:Sapphire laser, tunning range:680-1080 nm). The two-photon cross-section was measured to be 27 GM (GM stands for Goeppert-Mayer, 1 GM=10^{-50}cm^4.s) and 30 GM at 680 nm and 700 nm respectively.

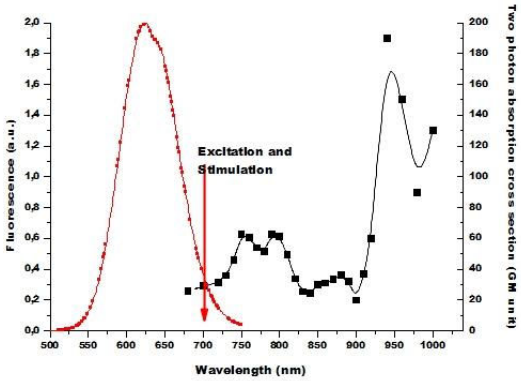

Figure 8.3: DCM two-photon absorption cross section (straight line and squares) and fluorescence (dotted line) spectra in DMSO. The arrow indicates the excitation and stimulation wavelength.

Taking into consideration all the properties described above, we can conclude that DCM represents a very promising dye to make the proof of principle for our setup and be used further in microscopy applications.

8.2 Pulse stretching

In the introduction section we have underlined that the basic idea of our setup is to use the same laser for two-photon excitation and one photon depletion. In order to do so, we will divide the main laser beam into two optical paths. One will be devoted to two photon excitation of the dye, without further modification, since femtosecond pulses exhibit high peak powers and are well-suited for nonlinear excitation. The second will be used for stimulated emission depletion of the excited state. Since stimulated emission is a linear process, its efficiency only depends on the total energy of the pulse. Therefore, to favor stimulated emission and avoid non-linear processes, the second pulse will be temporally stretched [159]. Our source is a fs Ti-Sapphire laser with broad spectral bandwidth which makes the pulse stretching achievable using dispersive elements that introduce wavelength dependent optical delays. In this case the different spectral components are separated in time and so the pulse is broadened.
For a better understanding of how femtosecond pulses are broadened we will start by a short description of ultrashort pulses. In the ideal case of a mode-locked laser where all oscillating modes have equal amplitude and are equally spaced, the pulse duration Δt is approximately:

$$\Delta t \approx \frac{2\pi}{(2n+1).\Delta\omega} = \frac{1}{\Delta\nu} \tag{8.1}$$

where $\Delta\omega$ is the frequency spacing between modes, 2n+1 is the number of equally spaced modes , $\Delta\nu$ is a full width of the generation band.
In the more general case of oscillating modes with non-equal amplitude distribution, in principle, the relation between the pulse duration and the width of oscillating spectra is:

$$\Delta t = \frac{k}{\Delta\nu} \tag{8.2}$$

where k is a factor of the spectrum shape. In this case generated pulses are called "transform limited pulses" [160].

The real electric field corresponding to an ultrashort pulse is oscillating at an angular frequency ω_0 corresponding to the central wavelength of the pulse. The complex

electrical field is defined (ψ is the time-dependent phase of the electric field):

$$E(t) = \sqrt{I(t)}.e^{i\omega_0 t}.e^{i\psi(t)} \tag{8.3}$$

In order to obtain the expression of the complex electric field in the frequency domain we make the Fourier transform of E(t):

$$\tilde{E}(\omega) = FT(E(t)) \tag{8.4}$$

In the frequency domain we define an intensity and a phase function

$$\tilde{E}(\omega) = \sqrt{S(\omega)}.e^{i\varphi(\omega)} \tag{8.5}$$

S(ω) is the spectral density of the pulse, and $\varphi(\omega)$ is the spectral phase. The spectral phase function $\varphi(\omega)$ can be a constant, in which case the pulse is called a bandwidth-limited pulse, or where $\varphi(\omega)$ can be a quadratic function, in which case the pulse is called a chirped pulse because of the presence of an instantaneous frequency sweep. Such a chirp may be acquired as a pulse propagates through materials (like glass) and is due to their dispersion. It results in a temporal broadening of the pulse.
The first derivative $\varphi'(\omega)$ is called the group delay (GD). GD leads to a shift of the pulse envelope in the time domain. The second derivative $\varphi''(\omega)$ is the group delay dispersion (GDD). Since GDD describes the frequency dependence of the GD it is responsible for dispersive effects.

Pulse stretching with diffraction gratings
Pulse stretching can be realized with dispersive elements such as diffraction gratings, prisms and fibers with non-zero dispersion. For our system we have used a pair of diffraction gratings in the configuration depicted in Fig. 8.4.

Diffraction grating is an optical component with a periodic structure, which splits and diffracts light into several beams traveling in different directions. The diffraction gratings we have used are plane holographic Newport Richardson Gratings with 1500 grooves/mm. Equation 8.6 is the grating equation and it is the relationship between

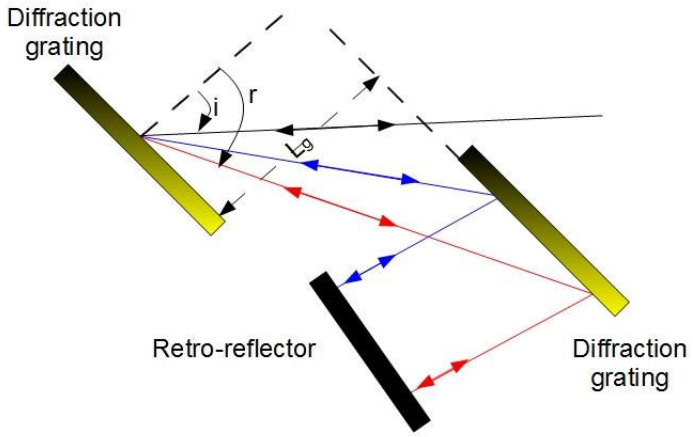

Figure 8.4: Dispersive pulse stretcher with diffraction gratings.

the grating spacing and the angles of the incident and diffracted beams of light.

$$m.N.\lambda = \sin i + \sin r \tag{8.6}$$

where m is the diffraction order, N is the groove frequency in grooves/mm, λ is the wavelength, i is the incident angle and r is the diffraction angle.

In the dispersive pulse stretcher, shown in Fig. 8.4 the spectral components of the pulse are separated by the first grating. The beams of different wavelengths propagate along different directions in the space between the two gratings. After diffraction by the second grating and the retro-reflector, the beams of different wavelengths become parallel but they have traveled different distances. The pulses of longer wavelengths have traveled longer distances in comparison to pulses of shorter wavelengths. Thus the pulses of higher frequency arrive earlier than lower frequency pulses in this configuration of parallel gratings.

In [161] the group delay dispersion for the grating configuration described above is :

$$GDD = \frac{\lambda^3.L_g.N^2}{2\pi c^2}.\frac{1}{[1-(mN\lambda - \sin i)^2]^2} \tag{8.7}$$

where L_g is the distance between the gratings, c the speed of light

The duration of the stretched pulse is:

$$\Delta t_d = GDD.\Delta\omega \tag{8.8}$$

Considering

$$\Delta\omega = \frac{2\pi c\Delta\lambda}{\lambda^2} \tag{8.9}$$

It yields

$$\Delta t_d = \frac{\lambda.\Delta\lambda.L_g.N^2}{c}.\frac{1}{[1-(mN\lambda-\sin i)^2]^2} \tag{8.10}$$

In our configuration we have chosen the parameters L_g=1 m and the incident angle i=40° in order to obtain a pulse of around 40-50 ps. The spectral bandwidth of the laser output was measured using a fiber spectrometer and found to be 2.7 nm at 680 nm and 3.5 nm at 700 nm. Using Eq. 8.10 and the above mentioned values we deduced the duration of the stretched pulse which is 32 ps and 45 ps at 680 and 700 nm respectively.

At the beginning of this section we stated that the pulse stretching is done using dispersive elements. Beside diffraction gratings, other dispersive elements are optical fibers. This method was used in [45], where it is recommended to use a glass bar to pre-stretch the pulse to avoid non-linear effects inside the fiber and afterwards inject the laser into a 100 m long optical fiber. We consider this an interesting option that could be implemented in our system. Its main advantage compared to gratings is that one can tune the laser wavelength without causing the beam to completely change direction in the stretcher.

8.3 Time correlated single photon counting (TCSPC)

In the first part of this work we have described in more detail the characteristics and photophysics of fluorophores. One important characteristic is the fluorescence lifetime. The lifetime of a dye is the time the molecule spends in the excited state before returning to the ground state. Fluorescence lifetimes are in the order of tens of ns. The lifetime determines the time available for the fluorophore to interact with or diffuse in its environment [5].
TCSPC technique was developed in the 1970's and a reference book dedicated to this

method is [162]. Our purpose in this work is to make a short introduction of this method and why we have chosen it for our experiments. In this study we have used the TCSPC technique because it is a sensitive technique that allowed us register the fluorescence lifetimes and make sure that the observed effects are due to stimulated emission. Compared to the CCD intensity measurements, TCSPC records a photon distribution versus the time in a fluorescence decay.

The principle of TCSPC is depicted in Fig. 8.5 [163]

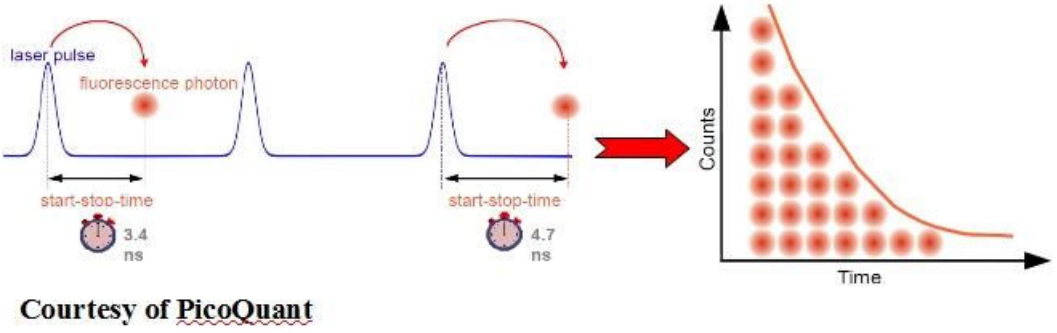

Figure 8.5: Principle of TCSPC method (left). Typical Fluorescence lifetime histogram: exponential decay (right).

In this method single photons from a fluorescence signal and their arrival time are precisely registered. The reference for the arrival time is the corresponding excitation pulse. Briefly, a pulsed light source excites a fluorophore. Synchronously, a trigger starts the timing process that is stopped at the arrival of the first photon. The measured time is stored in the memory and the excitation process is repeated several times. The typical result is a histogram with an exponential drop of counts towards later times. If the cumulative histogram of the fluorescence emission is analyzed, the fluorescence lifetime of the fluorophore can be estimated. The main condition is that less than one photon per laser pulse period needs to be detected in a given signal period, with a photon arrival time distribution built up over many pulses.

In Fig. 8.6 is showed our setup for TCSPC measurements.The fs laser pulse is focused through a 40x microscope objective into a spectrometer cell containing a dye solution. The fluorescence signal is collected through a lens and detected on a PMT. The electrical signal obtained from the detector is fed to the TCSPC electronics. The complete TCSPC electronics are contained on a single PC board (TimeHarp 200). In

the same time a small fraction of the laser is focused onto a photodiode. The signal from the photodiode is also fed to the TCSPC electronics.

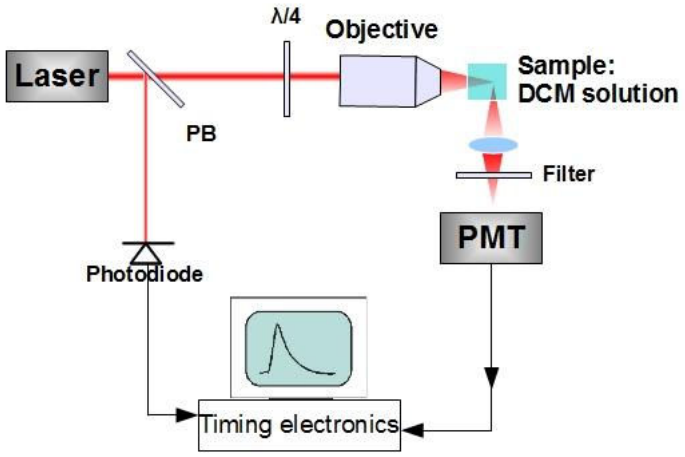

Figure 8.6: Setup scheme for TCSPC measurements.

By registering fluorescence decays with our TCSPC system we were able to adjust the delay between the two pulses in order to determine and optimize the depletion of the excited states and observe the polarization effects.

8.4 Optical setup

Our first purpose before performing microscopy experiments, was to test the validity of SW-STED concept by measurements in solution and numerical simulations. In this section we present the optical setup we have built for this purpose which is shown in Fig. 8.7.

The laser pulses for two-photon excitation and for stimulated emission of the dye, both come from a widely tunable (680-1080 nm), mode-locked Ti:Sapphire laser (Chameleon CoherentTM , Ultra II) delivering linearly polarized pulses with a typical duration of 140 fs and a repetition rate of 80 MHz.
The main fs pulse is split in two paths by a polarizing cube and the power distribution between the two paths can be adjusted by a half-wave plate. The first beam is used to excite the dye by two-photon absorption and the second beam is used to deplete the excited state by stimulated emission.
The beam intended for stimulated emission is passed through a pulse stretcher com-

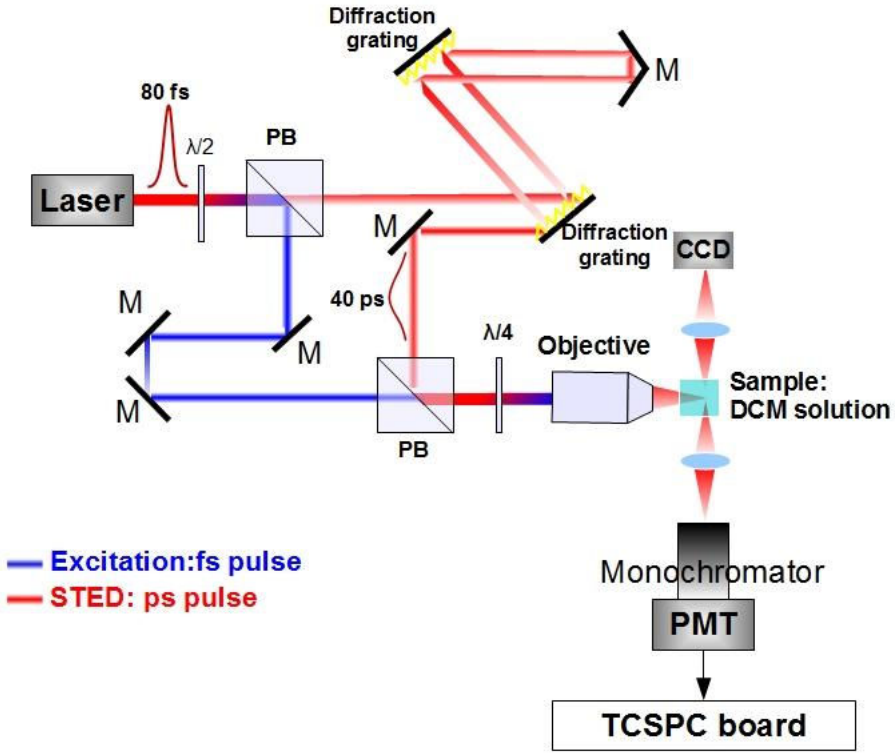

Figure 8.7: Experimental setup for depletion measurements in dye solution

posed of two diffraction gratings and described in detail in Section 8.2. As mentioned, the pulse duration is around 40 ps. In the further discussions we will refer to this beam as the STED beam.

We will refer to the other beam as the excitation beam, which is passed through a delay line in order to adjust the temporal delay between the two pulses. No other synchronization tools are necessary because the exciting and the depleting pulses are provided by the same laser source.

The two beams are recombined by a second polarizing cube and then their polarization is made circular by a quarter wave-plate, in order to produce a more efficient depletion compared to a configuration with crossed polarizations. The polarization aspect will be discussed further in the Results section. The two beams are attenuated and focused by a 40x objective (Olympus LUMPlanFL/IR, N.A.=0.80, working distance 3.3 mm) into a 1 cm-deep quartz cell containing the chosen dye. The back aperture of the objective lens was partially covered, therefore the effective N.A. was 0.5. Fluorescence was collected perpendicularly to the excitation and depletion beam by two 10x objectives (N.A.= 0.3). On one side the fluorescence spot was imaged

on a CCD camera (PixelInk Megapixel FireWire Camera). On the other side of the cell, the signal was focused on a monochromator (Jobin Yvon H20) equipped with a GaAs photocathode micro-channel plate (R3809U-61, Hamamatsu, Japan) connected to a time correlated single photon counting board (TCSPC PicoHarp 200, PicoQuant, GmbH, Berlin, Germany). A 50 μm slit was placed at the monochromator entrance, which allows rejection of the out-of-focus fluorescence caused by small residual one-photon fluorescence in the dye.

Chapter 9

Results

9.1 Stimulated emission depletion of two photon excited states

The results presented in this chapter have been obtained with the setup presented in Section 8.4. As mentioned before, the fluorophore with which we have realized most of the experiments was DCM dissolved in DMSO or Methanol. In Fig. 8.2 we have observed that around 680-700 nm the two-photon absorption and fluorescence emission spectra have the best overlap. Therefore, our experiments were performed at 680 nm and 700 nm, near the edge of the tuning range of our laser. These wavelengths are sufficiently red shifted compared to the linear absorption spectrum of DCM to avoid important one-photon excitation and two photon excitation by the STED beam was prevented by stretching the pulse.
In our experimental procedure we have simultaneously recorded the fluorescence traces with the CCD camera and the fluorescence decays with our TCSPC system. Fig. 9.1 shows the typical result we obtain with our system: a)the CCD image of a two photon fluorescence spot obtained with the excitation pulse (the STED pulse is blocked)and b) is represented the corresponding fluorescence decay. A fluorescence lifetime of τ=2.18 ns has been determined using a linearly polarized excitation beam. This value is in perfect agreement with previous measurements [164].

We further recorded successive images of the fluorescent focal spot of the focused

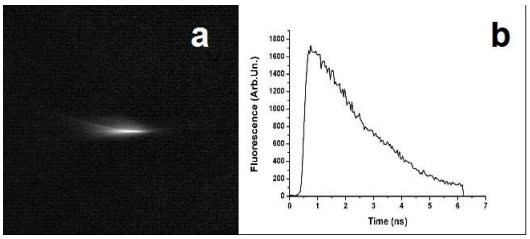

Figure 9.1: CCD image of the fluorescence spot in a DCM solution (a) and the corresponding fluorescence decay (b)

excitation beam alone (Fig 9.2a), of the focused STED beam (Fig.9.2b)(we observe that it does not cause significant two-photon excitation), and finally of the two overlapped beams, focused together into the dye cell (Fig. 9.2c). We can clearly observe an important fluorescence quenching at the focal spot when the two beams overlap.
Complementary to the CCD images we made TCSPC measurements. In this way, we were able to adjust the delay between the two pulses in order to optimize the depletion effect. In Fig. 9.2d, 9.2e and 9.2f, the fluorescence decays corresponding to the pictures above are presented. When only the excitation beam is focused in the sample, we observe a typical fluorescence decay as the one presented in 9.1. With the STED beam alone, almost no fluorescence signal can be detected (Fig. 9.2e). When the two beams overlap, the fluorescence signal created by the excitation beam was quenched to less than 10% (Fig. 9.2f).

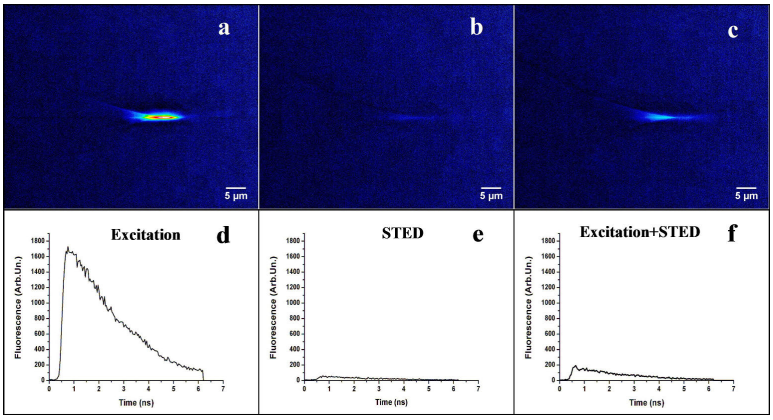

Figure 9.2: Images and time evolutions of fluorescence emission in the DCM cell. Upper part: images taken with a CCD camera on the side of the sample cell inside which either the excitation beam (fs pulse) alone (a), or the STED beam (ps pulse) alone (b) are focused, or the two beams are overlapped (c). Lower part: fluorescence decays recorded with TCSPC device: (d), (e) and (f) correspond to images (a), (b) and (c) respectively. Average powers: 25 mW for excitation beam, 80 mW for STED beam

9.1.1 Photothermal effects

It is important to check that the observed fluorescence quenching is not due to a parasitic phenomenon such as thermal lensing, but is really caused by stimulated emission. The thermal lens effect was discovered by Gordon, et al. and it is presented in [165]. It is a photothermal effect and results when energy from a laser beam passing through a sample is absorbed, causing heating of the sample along the beam path. The lens is created through the temperature dependence of the sample refractive index. The lens usually has a negative focal length since most materials expand upon heating and the refractive index is proportional to the density. The thermal lens effect can cause a defocusing effect which as described in [166] in the case of TPE can cause a reduction of the fluorescence signal.
Therefore, in order to rule out the possibility of thermal lensing, we have intentionally delayed the STED beam by a small lapse of time (0.5 ns) as shown in Fig. 9.3. It can clearly be observed that fluorescence quenching occurs only when the STED pulse is applied. No cumulative effect from one pulse to the following was observed. Therefore we could exclude the occurrence of undesired thermal effects. Moreover, after quenching, the fluorescence decay remains a single exponential with an unchanged time constant, only the signal amplitude is affected. This is a signature of stimulated emission depletion, and has been observed previously [154] [167].

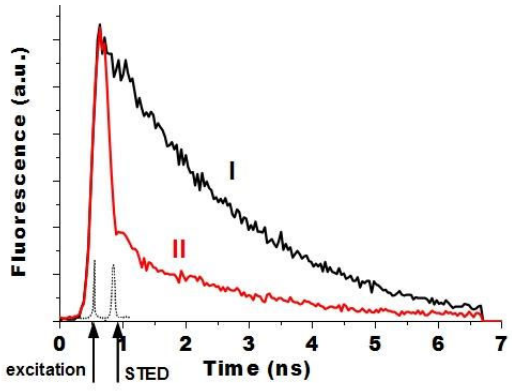

Figure 9.3: Two-photon excited fluorescence quenched by a STED pulse delayed of 0.5 ns: (I) fluorescence decay without STED pulse; (II) fluorescence decay in presence of the STED pulse.

9.1.2 Polarization effects

In previous chapters we have mentioned the importance of the relative polarization between the two beams in fluorescence quenching by stimulated emission. It is stated that the best quenching effect is obtained when the two beams have the same polarization. Therefore, in the following experiment we have compared the depletion effect obtained using two beams with crossed polarizations (Fig.9.4a) and circular polarization (Fig. 9.4b) at the same power.

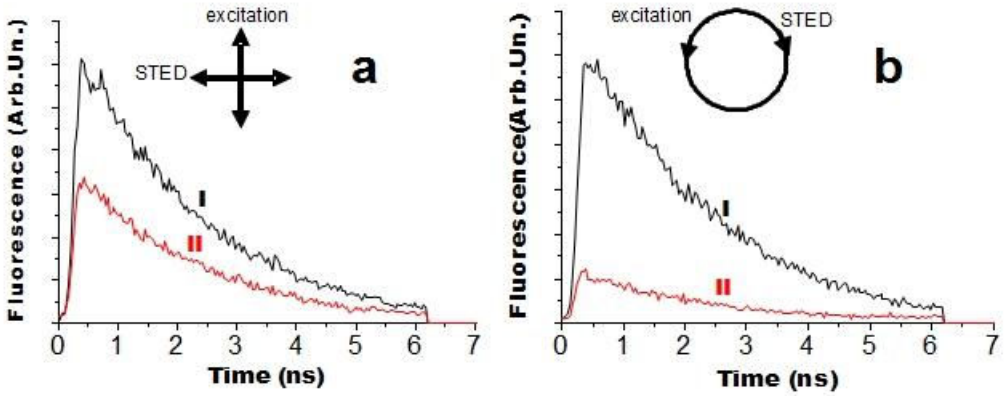

Figure 9.4: Comparison between fluorescence quenching in the case of crossed polarizations (a) and circular polarizations (b). For both graphs the black curve (I) is the fluorescence decay with no STED beam and the red curve (II) is the fluorescence decay when the fluorescence is quenched by the STED beam

We can observe that the quenching effect is less efficient in the case of crossed polarizations. This is explained by the fact that only the molecules that have the transition dipole parallel to the polarization of the excitation pulse could be excited. If the STED beam has a perpendicular polarization, only the molecules that have rotated in the solvent could be depleted. Since the delay between the two pulses is short, only few molecules have had time to rotate, therefore the depletion efficiency is low. This effect is in agreement with previous theoretical work. When circularly polarized beams are used, a more efficient quenching can be observed as shown on Fig. 9.4b, since this reorientation problem is not present. Therefore, all the results presented hereafter are obtained using circularly polarized beams.

9.1.3 Fluorescence depletion: Experimental and numerical results

At the beginning of this part of the thesis, in Chapter 7 we have introduced the rate equations for SW-STED. We have observed that, as in other STED systems, the depletion of the excited states by stimulated emission increases exponentially with the STED power. In this section our goal was to carry out experiments to validate the model, more precisely the exponential law and determine the stimulated emission cross section. We have also performed numerical simulations to estimate the resolution we could obtain with a SW-STED microscope.

In order to estimate the behavior of the fluorescence quenching and the stimulated emission cross-section we have realized the following experiment in DCM dye solution in DMSO: the excitation pulse power was kept constant at 25 mW and the STED pulse power was varied from 10 mW to 80 mW at 680 nm, and from 10 mW to 200 mW at 700 nm. The experiments were carried out both at 680 nm and 700 nm for comparison reasons, since at 680 nm we estimated the fluorescence depletion would be more efficient, while at 700 nm we could obtain higher laser power.
The results we have obtained are shown in Fig.9.5. As predicted, fluorescence quenching increases exponentially with the STED beam intensity. The curve measured at 680 nm decreases more sharply than that measured at 700 nm, which indicates a more efficient depletion. This is in agreement with Eq.7.6: since the spectral dependence of stimulated emission cross-section σ_{STED} is similar to the fluorescence emission spectrum (shown on Fig.8.2) as it has been experimentally demonstrated in previous studies [168] [51], when changing the wavelength of excitation-stimulation from 680 nm to 700 nm, σ_{STED} is reduced by close to a factor of 2.

More precisely, following Eq.7.6, the exponential fit of the two curves of Fig. 9.5 (the offset will be discussed later), and the STED pulse duration which is 32 ps and 44 ps for 680 nm and 700 nm respectively, we deduce the following cross sections for stimulated emission (σ_{STED}): at 680 nm σ_{STED}=7.10^{-18} cm^{-2} and at 700 nm σ_{STED}=3.10^{-18}.
We can observe that these values are close to the typical cross sections of allowed transitions in dye molecules and previous data for DCM molecule [169].
As mentioned before, in Fig. 9.5, the curves present an offset that it is not predicted by the simple model of Eq.7.6. Approximately 10% of the fluorescence signal could not be depleted. One reason of this offset could be the imperfect overlapping between

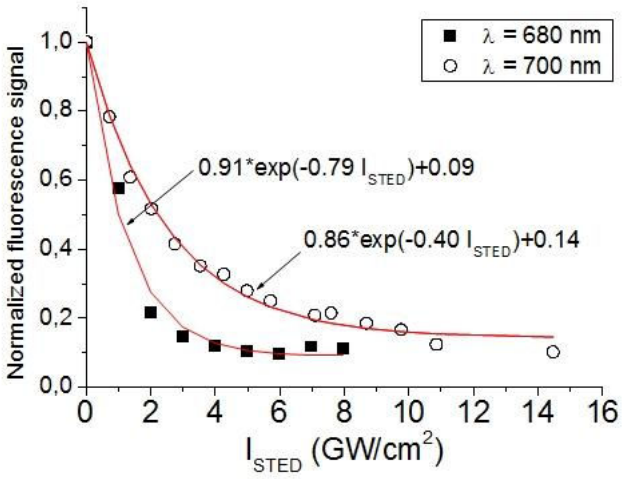

Figure 9.5: Fluorescence depletion as function of the peak intensity of the focused STED beam for excitation/stimulation at 680 nm (filled squares) and 700 nm (circles)

the two focused beams. Another possible reason is the polarization dependence of the depletion efficiency as shown in Fig. 9.4: since our experiment needs a minimum delay between the excitation and depletion beams a small amount of rotational depolarization could occur reducing the quenching efficiency. A reason which we have not verified might be the distortions of the STED beam wavefront introduced by the gratings. These distortions could affect the focusing power of the microscope objective, and therefore the profile of the STED beam at the focal point. In addition, as we will show in the following paragraphs, the fraction of population that can be depleted is intrinsically limited in the SW-STED method.

Numerical calculation

Fluorescence quenching

The following numerical calculations have been realized for a better understanding of how the excited states are depleted in the SW-STED scheme. In the calculations we can go further and predict what we should expect at higher powers, what size the PSF will have in a SW-STED microscope and what the limitations of the system are. In order to do so we used the coupled rate equations presented in the Chapter 7. We assumed that all the molecules are initially in the ground state low vibrational levels, the populations of the four levels were evolved step by step (time interval of 20 fs) according to the rate equations. The fluorescence signal is supposed to be proportional

to the time-averaged population (n_1) of the excited state low vibrational levels. In the calculations, photophysical constants have values close to our experimental conditions at 680 nm. The two photon absorption cross-section σ_{TPA} was set to 27 GM as determined experimentally.
The radiative τ_{rad} and non radiative τ_{NR} relaxation time were deduced from the fluorescence lifetime we have measured (τ=2.18 ns), assuming a quantum yield of ϕ=0.8 [152]: we obtain $\tau_{rad} = \tau/\phi$ = 2.7 ns and $\tau_{NR} = \tau/(1-\phi)$=11 ns.
We used the stimulated emission cross-section value estimated above. The fast vibrational relaxation was supposed to be 1 ps, in agreement with previous work on molecular dyes [154] [170]. Laser pulse durations and delay are the same as in our experiments.

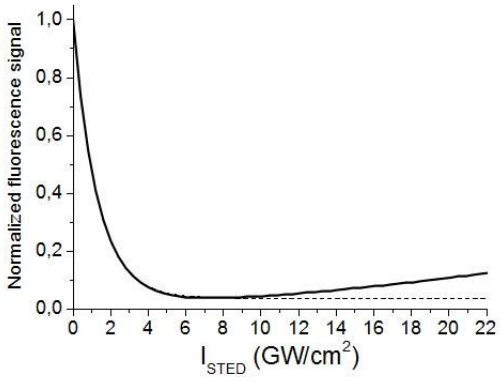

Figure 9.6: Calculated fluorescence depletion as a function of STED beam intensity in the single wavelength scheme (solid line). The beginning of the curve was fitted by an exponential decay (dashed line).

First we calculated the fluorescence depletion as a function of the STED instantaneous intensity. The result for the wavelength of 680 nm is shown in Fig.9.6. For low STED intensity, the fluorescence signal decreases exponentially, in agreement with our experimental measurements. This behavior is similar to the one observed previously for two wavelengths depletion measurements [155]. However, as the STED intensity is increased, the intensity signal no longer follows this exponential decay but increases again. This is due to two-photon transitions induced by the STED beam. Two-photon excitation probability varies as the square of the intensity, whereas stimulated emission increases linearly. Therefore, if the STED intensity is increased beyond a certain level, two-photon absorption will become dominant and generate significant fluorescence signal. The cross-over intensity level depends on the ratio between the

cross-sections of two-photon absorption versus stimulated emission. The minimum residual fluorescence signal should be 3% in our experimental conditions. This value can be reduced by further stretching the STED pulse duration. When comparing with the experimental curve at 680 nm in Fig. 9.5, we can see a good agreement in the order of magnitude of I_{STED}: the experimental data being limited to the region below 8 GW/cm^2 (limited by our laser power), the rise of fluorescence was not observed, in agreement with the calculated curve. Moreover, part of the offset in the experimental curve (9% of the initial fluorescence signal) can be accounted for by the onset of two-photon excitation induced by the STED beam which leads to a residual fluorescence of 3% as shown in Fig.9.5. The remaining 6% should be attributed to other factors such as non-perfect overlapping of the two beams or orientational relaxation of the molecules in the time lapse between the two pulses, which may reduce the depletion efficiency [171].

Theoretical point spread function(PSF) and optical transfer function (OTF) of a SW-STED microscope

The final purpose of work is to apply the SW-STED concept to microscopy applications. The experiments and numerical simulations we have realized and described above can help us make estimations of the PSF and OTF of a microscope based on the SW-STED principle.

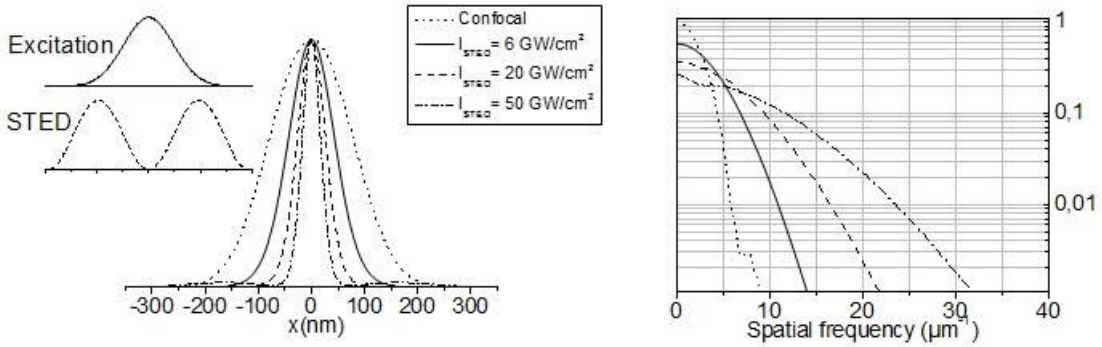

Figure 9.7: Calculated point spread function (PSF) and optical transfer function (OTF) for a SW-STED microscope with increasing peak intensity in the STED beam (the case I_{STED}=0 corresponds to a conventional two-photon microscope with a pinhole). The excitation and STED beam profiles are shown in the inset. The calculations are based on a NA=1.4 microscope objective, a laser wavelength of 680 nm and a configuration with a pinhole in the image plane.

To calculate the PSF we assumed the excitation beam has a Gaussian profile of the form $\exp(-2.x^2/\omega^2)$ where $\omega = \lambda/2NA$ (λ is the wavelength and NA is the numerical aperture of the microscope) and the STED beam exhibits zero intensity in the center. For simplification, the STED profile was supposed to be that of a standing wave: $sin^2(\pi.x.NA/\lambda)$. The excitation and STED beam profiles are depicted in the inset of Fig. 9.7.
For the calculations we considered 680 nm the working wavelength and a microscope objective with NA=1.4. We supposed that a pinhole is present in the image plane in front of the detector like in a confocal microscope, although many two-photon microscopes use large area detectors. This pinhole is useful to reject unwanted fluorescence from either one-photon or two-photon absorption of the STED beam.
In this case, the overall PSF is given by the product of the excitation PSF by the detection PSF. For a confocal microscope these two functions are similar in width. When fluorescence depletion occurs, the excitation PSF is changed but not the detection PSF. To take into account the depletion effect, the fluorescence profile was calculated for each abscissa x by solving the rate equation numerically using the same parameters as in Fig. 9.6. Then, it was multiplied by the detection PSF which is supposed to be a Gaussian similar to the excitation profile. This was done for different values of the maximum intensity in the STED profile I_{STED}, and the resultant normalized PSF is shown on Fig. 9.7. As the STED intensity is increased, we observe a sharp narrowing of the central peak of the PSF, which indicates a better resolution. However, for high values of I_{STED}, side lobes can be seen to grow on each side of the central peak, due to two-photon absorption of the STED beam. This is the same phenomenon as the rise of fluorescence in the curve on Fig. 9.6. Although the presence of side lobes will cause each bright spot to be surrounded by a ring in the images, we believe it does not fundamentally limit the resolution enhancement, since a better image could be recovered by deconvolution.
A reliable way to assess the intrinsic resolution of an optical system is to use the OTF (Chapter 1) which describes the strength with which each spatial frequency of the object is transferred to the image. The resolution is given by the highest spatial frequency that can be passed above noise level. We obtained the OTF by calculating the Fourier transform of the PSF. They are shown on Fig. 9.7 for different values of I_{STED} (the same normalization factor is used for all four curves). When the STED intensity increases, the amplitude of the OTF decreases since the fluorescence signal is quenched, but the bandwidth is significantly enlarged which clearly indicates an improvement of the resolution of the microscope. Therefore, in the SW-STED approach, although reabsorption of the STED beam will have an impact on the shape of the PSF

for high depletion power, it does not impair the capacity of this technique to fundamentally improve the resolution.

9.1.4 Conclusion

In this section, we have presented an experimental proof of SW-STED in solution. We believe that this concept could be applied to super-resolved microscopy by making it possible to turn a standard TPE microscope into STED microscope at low cost, since the Ti:Sapphire laser that is commonly used as an excitation source in TPE microscope could also supply the STED beam. By employing one wavelength from a single laser, the problems caused by chromatic aberrations of the optics and accurate synchronization of different sources can be avoided. Moreover, since the incident wavelength can only generate two-photon absorption, photo-bleaching and photo-toxicity should be restricted to the focal spot, even at higher powers.
Finding the best dye for a STED microscope is a challenging task, and even more for our particular setup. We would like to extend the list of dyes to be used in a SW-STED microscope. In order to do so, we will have to change the pulse stretching method to a fiber based system that will allow us to change the wavelength more easily. Using this method we will also be able to stretch the pulses to longer duration than with the grating without the need of a larger optical table.
This stage in the development of a SW-STED microscope allowed us to test the validity of the concept and in the same time discover the possible problems and what we can change in order to improve the setup.
The results obtained in this section convinced us that the SW-STED concept would be interesting for application to microscopy, therefore the next natural step was to build the image acquisition part of the microscope. This work and preliminary results will be presented in the next section.

9.2 SW-STED microscope - Optical setup and first images

The purpose of the work presented in Section 9.1 and published in [153] was carried out mainly to prove the interest of the SW-STED concept and its applications in microscopy. We believe that this concept could be applied to super-resolved microscopy by making it possible to turn a standard TPE microscope into a STED mi-

croscope. One would only need to add a device to stretch the STED pulse and adjust the delay between the two pulses. Therefore, the next step after this proof of principle is to use this concept in a microscope. In this section we present our work in building a custom microscope (Fig.9.8) and the preliminary results obtained with it.

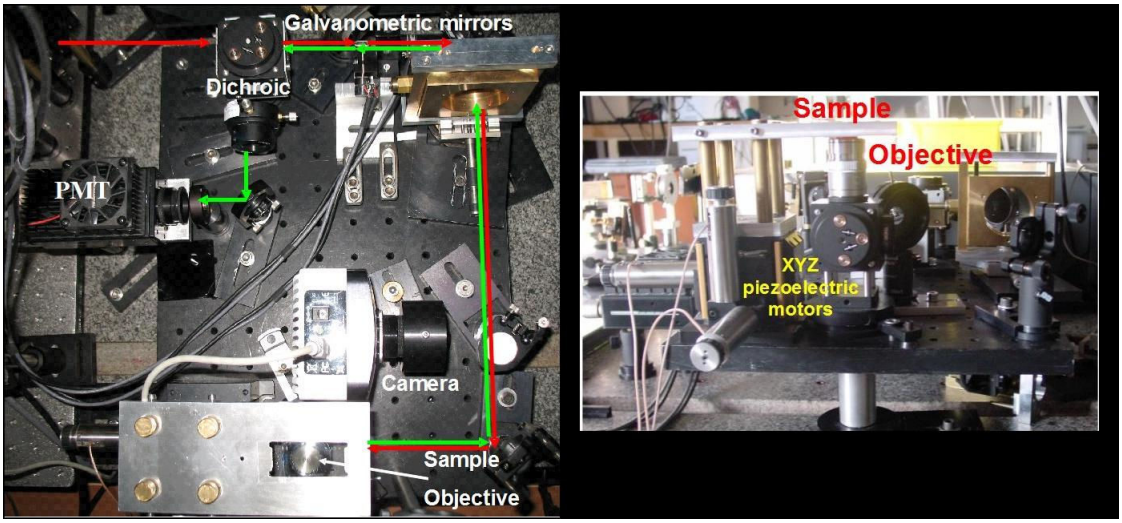

Figure 9.8: Photograph of the custom microscope setup : top view (left hand side image), side view (right hand side)

Optical setup The optical scheme of the microscope is shown in Fig. 9.9. The optical path of the laser beam before entering the microscope is the one shown in Fig.8.7: the laser beam is split into two optical paths: one for excitation (fs pulse) and the other for stimulated emission depletion (ps pulse). The STED beam is passed through a vortex phase plate (VPP-1, RPC Photonics, NY, USA). The vortex phase plate imprints a helical 0-2π phase ramp on the beam's wavefront [172]. When the beam is focused in such a way, it creates a Gauss-Laguerre beam (described in Section 4.2.1). When used to deplete the excited state population, molecules can stay excited only in the region around the zero intensity point and this region becomes narrower.
The two beams are recombined by a polarising cube (identical to the one used for beam-splitting), and injected into the setup represented in Fig.9.9. The beam is transmitted by a dichroic filter (BrightLine Multiphoton 680/SP Semrock, USA) on two computer controlled galvanometric mirrors. The two mirrors are arranged orthogonally to generate the laser beam scanning pattern in the X-Y plane. Although, scanning with this kind of mirrors is slower than with resonant scanners, the systems based on galvanometric mirrors provides finer control of the pixel dwell time and gives the possibility to scan arbitrary regions of interest or to localize the laser beam at a particular spot [173]. Two lenses (not represented in the optical scheme) are

mounted to expand the beam in order to cover the back aperture of the objective lens and conjugate it with the galvanometric mirrors.
The laser beam is collimated and focused in the sample through a 100x oil immersion objective with NA=1,45 (HCX PL APO, Leica, Germany).
The fluorescence was collected by the objective and after de-scanning it was separated from the excitation and STED beams by the dichroic mirror and focused on a PMT (Photosensor module H7422P-40,Hamamatsu,Japan). An adequate bandpass filter was positioned in front of the detector to remove scattered light. The signal from the PMT is fed to an analog input of the acquisition board.
For wide-field imaging using the CCD camera we placed a foldable mirror which directs the signal from the sample towards the CCD camera. The sample was illuminated with transmitted light from above from a red emitting diode.
The microscope stand was custom built in order to make the microscope setup as flexible as possible in terms of optical design. The sample holder was equipped with a XYZ piezoelectric motor(MDE125, Elliot Gold Series XYZ Flexure Stage, United Kingdom) used for positioning the sample.

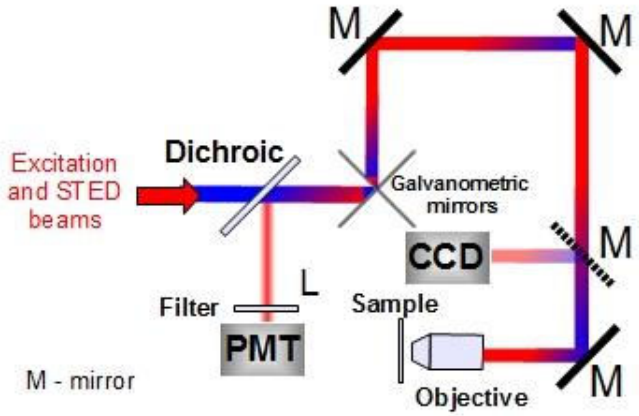

Figure 9.9: Optical layout of the SW-STED microscope

Gold bead imaging

In STED microscopy experiments the most used method for alignment of the excitation and the STED beams and for PSF measurement is to scan gold nanobeads smaller than the theoretical resolution of the microscope, which act as point scatterers. In this section we present the scanning images of the 80 nm gold beads obtained with the setup shown in Fig.9.9. In the case of gold nanobeads we detect the scattering of gold particles, not the fluorescence.

We prepared the samples by depositing 70 μl of a 1000x diluted solution of 80 nm gold nanobeads (BB international, UK) on a Poly-Lysine coated coverslip. The coverslip was washed, dried and mounted in Mowiol medium. The protocol is described in more detail in Section 5.1.1.
The critical point in STED microscopy is the superposition of the two beams that have to be collinear and overlapped. Therefore, before scanning the gold beads we roughly aligned the beams in a two step protocol. First the two beams were roughly aligned by projecting them at 5 m on a white surface. Secondly, the beams were injected into a 20x microscope objective and the beams were aligned at 20 cm from the objective's exit. This two steps were repeated until the beams overlapped.
Finally, the gold bead sample was scanned separately with the two beams. 3D stacks consisting of 10 XY images separated by 100 nm in Z direction were recorded in order to find the best focus. The Z scan was done with the piezoelectric motor. The pixel size was 7.6 nm in the X and Y direction. After establishing the best Z position we aligned the excitation and the STED beam by scanning on a series of gold beads. An example of the merged images obtained with the excitation beam (green) and STED beam (red) is shown in Fig. 9.10.

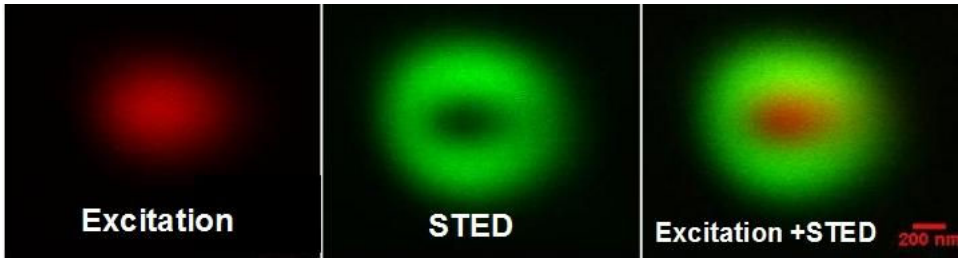

Figure 9.10: Scanning images of gold beads with the excitation and STED beam and the merged image

Fluorescent bead imaging

In order to continue the work presented in Section 9.12, ideally it would be to test the resolution improvement of our SW-STED microscope with DCM doped nanobeads. Unfortunately we could not find commercially available beads (size 100 nm or less) containing the DCM dye. For this reason we have tried several alternative solutions to test the resolution but the results were not conclusive.
One solution we tested was to image negatively stained silica beads immersed in DCM fluorescent solution [155]. Due to sample preparation issues and the poor wide-field system performance we were not able to visualize the silica beads.
Another approach was to stain with the DCM dye gold nanorods (GNR) (length=50

nm, width=15 nm) [174]. A solution of GNRs- PolyStyrene Sulfonate-Bovine Serum Albumin was incubated for 24 hours with a 10^{-3} M DCM (DMSO) solution [175]. From the emission spectrum of the doped GNR (Fig. 9.11) we observe that compared to a DCM-DMSO solution we can obtain a fluorescence enhancement. The premise of fluorescence enhancement is provided by the fact that the PSS-BSA layer plays the role of spacer and linker by fixing the DCM molecule at the optimal distance to enhance the fluorescence intensity [176]. Therefore we consider these objects good candidates for resolution testing of the SW-STED microscope. Unfortunately, in the images of DCM doped GNR we were not able to image isolated GNR because of the formation of aggregates. This work was realized in collaboration with the group of Prof. Simion Astilean from the Center for Nanobiophotonics and Laser Microspectroscopy, Cluj-Napoca, Romania.

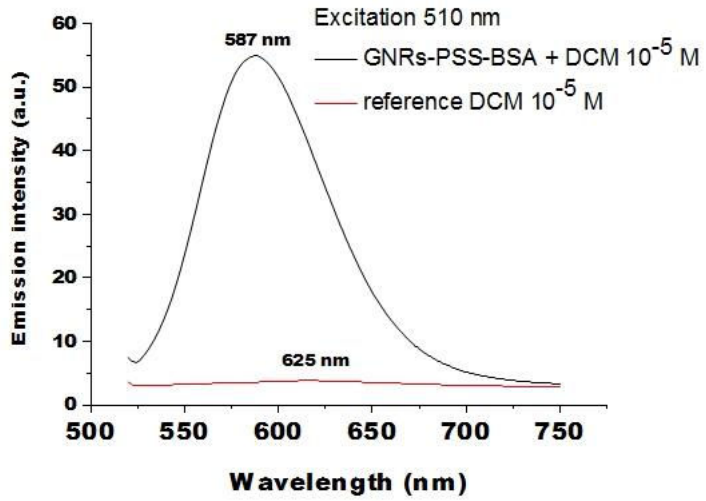

Figure 9.11: Emission spectrum of DCM 10^{-5} M solution (red line) and of GNR doped with 10^{-5} M DCM solution (black line) at 515 nm excitation

Since the previous approaches to test the microscope's resolution were not conclusive we chose the commercial fluorescent 100 nm diamter PD-Chromeo 494 Carboxylated Nanoparticles (Chromeon GmbH, Germany) as objects for resolution testing. The absorption and emission spectra of Chromeo beads are shown in Fig. 5.2. The images in Fig.9.12 were taken in the presence of the STED pulse then without it (due to photobleaching the second image is dimmer). In the two-photon image without STED (right hand side) the diameter of the beads is around 310 nm. When the STED pulse is on (left hand side), we can observe a reduction of the bead diameter of ≈ 30 nm for all the beads in the field of view.

In this first imaging test of the beads we could observe a resolution improvement in the case of SW-STED image compared to two-photon image. Obviously, the bead diameter we obtain in the image is far from the real size of the bead (100 nm). An important problem is the bad signal-to-noise ratio due to several reasons. One is the fact that the fluorophore is diffusing out from the beads. Another reason is that we do not know the absorption cross-section of the dye at 700 nm and we cannot easily change the excitation/depletion wavelength. A solution to this problem is to change the pulse stretching system with one based on optical fibers.
The PMT is not the best option when detecting weak signals, so we intend, in the future, to replace it with a photon counting module containing an avalanche photodiode.

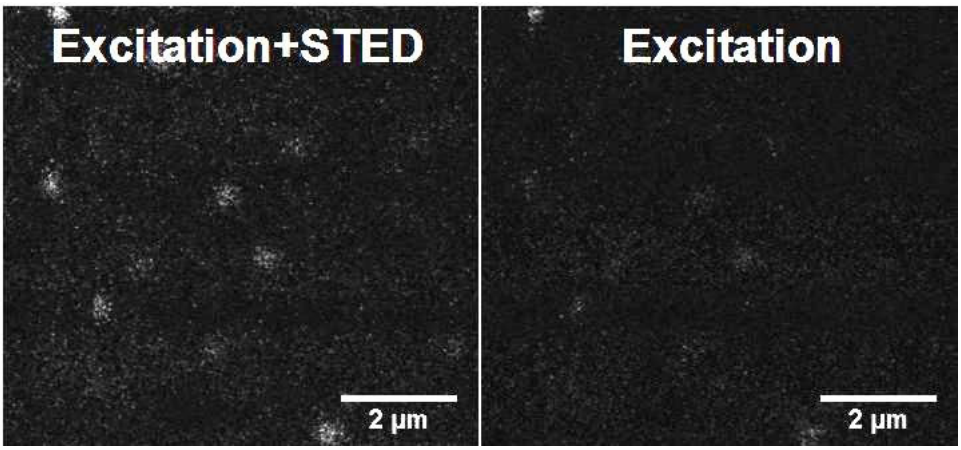

Figure 9.12: Fluorescence images of PD-Chromeo nanobeads when both pulses are on (left) and only the excitation pulse in on (right)

Chapter 10

Conclusions

In this part of the thesis we have introduced an alternative scheme for STED microscopy that we have named SW-STED (Single Wavelength STimulated Emission Depletion). In our approach, two photon excitation and stimulated emission are induced using a unique wavelength from a single laser source (a Ti:Sa laser oscillator). We have demonstrated the possibility to quench two-photon excited fluorescence by stimulated emission with a single wavelength. Time-resolved fluorescence intensity measurements were used to ascertain that the observed quenching is due to stimulated emission and not thermal or other photochemical effects since fluorescence extinction and recovery are in the ps range, in addition the effect is perfectly reversible. The amount of quenching as a function of the STED intensity follows an exponential law, as predicted and seen in previous literature [155]. In our experiment, the intensity necessary for depletion was relatively high (approximately 1 GW/cm^2 for 50% fluorescence depletion). This could certainly be improved by further stretching the duration of the STED beam: it was only 32 ps long in our experiment. Since stimulated emission only depends on the pulse energy, if the STED pulse is stretched to 200 ps, the same depletion efficiency would be obtained with an intensity level divided by 6 (meaning 160 MW/cm^2 for 50% fluorescence depletion). Another option would be to better match the fluorophore emission spectrum and the laser wavelength.
In SW-STED, the wavelength used for depletion is the same as the one inducing two-photon excitation. Therefore, we have to face the potential problem of fluorescence excitation by the STED beam. Since two-photon absorption increases as the square of the STED intensity whereas stimulated emission probability varies linearly, the first

process will become dominant for high intensity levels. We have examined this problem using numerical simulations and found that it is not a fundamental obstacle to resolution improvement. A good microscope configuration would include a pinhole in the image plane in order to reject fluorescence signal outside the focused spot. This pinhole would also reject any one photon excited fluorescence generated by the STED beam.
Even for high depletion powers, we have observed a small fraction of residual fluorescence that is not explained by the theory. This can probably be attributed to the imperfect overlap between excitation and STED beams. For example, the distortions of the STED beam wavefront introduced by the gratings may affect the profile of the STED beam at the focal point. This could be easily corrected by using a spatial filter to clean the wavefront. However, we believe this residual fluorescence will not affect the imaging capabilities of SW-STED microscopy since highly resolved cell imaging has already been performed with a higher fluorescence offset [149].
Although in the fluorescence depletion measurements and the numerical calculations we have used DCM dye, this fluorophore is not the only good candidate. The SW-STED method can be extended to other fluorophores, the main requirements being a large Stokes-shift and sufficient overlap between fluorescence emission and two-photon absorption spectra. For example, Pyridines [3] and Styryl [177] dye families exhibit large Stokes-shifts and two-photon absorption cross-sections and have already been used successfully in STED microscopy. For live cell imaging, interesting options include large Stokes-shift red fluorescent proteins [178].

In the first part of this work we have presented an experimental proof of SW-STED in solution. The results we have obtained encouraged us to continue this work and apply the SW-STED principle to a TPE microscope. Therefore in the second part we have built a scanning microscope and used the fs pulse for excitation and the ps pulse for stimulated emission depletion. The microscope was custom build and has the configuration of a typical TPE microscope. The fine alignment of the two beams was realized using gold nanobeads. When scanning fluorescent beads in the STED mode we observed a 30-40 nm resolution improvement compared to the TPE mode. This a preliminary result and the microscope is a work in progress. One problem is the stability of the alignment which is not very good due to the long optical path. We also encountered problems in finding the most suitable fluorophores and fluorescent objects. In the microscopy part one issue was the low signal which was not easily detected with our analogical system.
The next steps involve changing the detection mode to photon counting and improve

the enclosure of the setup. Changing the pulse stretching method to a fiber system will allow us to change more easily the wavelength we want to use, so we can better chose and test different dyes. The beam quality (TEM00) at the exit of the fiber is better than when using gratings that introduce aberrations. Using the fiber pulse stretching method will make the setup more compact (for a 200 ps pulse there we will not need a 5m table) and more mechanically stable. One disadvantage is that we will have to synchronize one pulse with the next pulse delivered by the laser 12 ns later. Due to the low jitter of the Ti:Sa oscillator, it should be possible to obtain a stable synchronization.

Bibliography

[1] E. Abbe. Beitrage zur teorie des mikroskops unde der mikroskopischen wahrnehmung. *Archiv fur mikroscopische Anatomie*, 9 (1):413–418, 1873.

[2] Stefan W. Hell and Jan Wichmann. Breaking the diffraction resolution limit by stimulated emission: stimulated-emission-depletion fluorescence microscopy. *Opt. Lett.*, 19(11):780–782, June 1994.

[3] T. A. Klar and S. W. Hell. Subdiffraction resolution in far-field fluorescence microscopy. *Optics Letters*, 24(14):954–956, 1999.

[4] A.Jablonski. Uber den mechanisms des photolumineszenz von farbstoffphosphoren. *Z Phys*, 94:38–46, 1935.

[5] Dr. Joseph R. Lakowicz. *Principles of Fluorescence Spectroscopy*. Springer, 2006.

[6] H. H. Jaffe and Albert L. Miller. The fates of electronic excitation energy. *J. Chem. Educ.*, 43 (9):469, 1966.

[7] Fluorescent probes. Technical report, Thermo scientific, 2013.

[8] A. Einstein. Kinetic equilibrium of absorption and emission of blackbody radiation by an atom. *Physik Z.*, 18 (121), 1917.

[9] W.L. Barnes, R. Laming, E.J. Tarbox, and P.R. Morkel. Absorption and emission cross section of er3+ doped silica fibers. *Quantum Electronics, IEEE Journal of*, 27(4):1004–1010, 1991.

[10] B.P. Straughan and S. Walker. *Spectroscopy, Vol.3*. Chapman and Hall, London, 1976.

[11] Alun T. Rhys Williams, Stephen A. Winfield, and James N. Miller. Relative fluorescence quantum yields using a computer-controlled luminescence spectrometer. *Analyst*, 108:1067–1071, 1983.

[12] P. Pringsheim. *Fluorescence and phosporescence*. Interscience, New York, 1949.

[13] L. Song, E.J. Hennink, I.T. Young, and H.J. Tanke. Photobleaching kinetics of fluorescein in quantitative fluorescence microscopy. *Biophysical Journal*, 68(6):2588 – 2600, 1995.

[14] L. Song, C.A. Varma, J.W. Verhoeven, and H.J. Tanke. Influence of the triplet excited state on the photobleaching kinetics of fluorescein in microscopy, June 1996.

[15] M. Minsky. Microscopy apparatus. US Patent 3013467, 1957.

[16] C. Cremer and T. Cremer. Considerations on a laser-scanning-microscope with high resolution and depth of field. *MICROSCOPICA ACTA*, 81:31–44, 1978.

[17] W. Denk, J. H. Strickler, and W. W. Webb. Two-photon laser scanning fluorescence microscopy. *Science*, 248:73–76, 1990.

[18] M. Goppert Mayer. Uber elemenelement mit zwei quantensprungen. *Ann Phys*, 5:273–94, 1931.

[19] PA Franken, AE Hill, CW Peters, and Weinreich G. Generation of optical harmonics. *Phys. Rev. Lett.*, 7:118–119, 1961.

[20] Callis PR. Two-photon-induced fluorescence. *Ann Rev Phys Chem*, 48:271–297, 1997.

[21] Nicolas Olivier, Miguel A. Luengo-Oroz, Louise Duloquin, Emmanuel Faure, Thierry Savy, Israel Veilleux, Xavier Solinas, Delphine Debarre, Paul Bourgine, Andres Santos, Nadine Peyrieras, and Emmanuel Beaurepaire. Cell lineage reconstruction of early zebrafish embryos using label-free nonlinear microscopy. *Science*, 329(5994):967–971, 2010.

[22] Jasmin Herz, Bernd H. Zinselmeyer, and Dorian B. McGavern. Two-photon imaging of microbial immunity in living tissues. *Microscopy and Microanalysis*, 18:730–741, 8 2012.

[23] P. Bousso and H. D. Moreau. Functional immunoimaging: the revolution continues. *Nat Rev Immunol*, 12:858–64, 2012.

[24] SethW. Perry, RyanM. Burke, and EdwardB. Brown. Two-photon and second harmonic microscopy in clinical and translational cancer research. *Annals of Biomedical Engineering*, 40(2):277–291, 2012.

[25] Karel Svoboda and Ryohei Yasuda. Principles of two-photon excitation microscopy and its applications to neuroscience. *Neuron*, 50(6):823 – 839, 2006.

[26] Giuseppe Chirico, Fabio Cannone, Sabrina Beretta, Giancarlo Baldini, and Alberto Diaspro. Single molecule studies by means of the two-photon fluorescence distribution. *Microscopy Research and Technique*, 55(5):359–364, 2001.

[27] Fritjof Helmchen and Winfried Denk. Deep tissue two-photon microscopy. *Nature Methods*, 2(12):932 – 940, 2005.

[28] B.-G. WANG, K. KONIG, and K.-J. HALBHUBER. Two-photon microscopy of deep intravital tissues and its merits in clinical research. *Journal of Microscopy*, 238(1):1 – 20, 2010.

[29] Michiel Mueller. *Introduction to Confocal Fluorescence Microscopy*. SPIE PRESS BOOK, 2005.

[30] S. W. Hell and M. Kroug. Ground-state-depletion fluorescence microscopy - a concept for breaking the diffraction resolution limit. *Applied Physics B-Lasers and Optics*, 60(5):495–497, 1995.

[31] Rainer Heintzmann, Thomas M. Jovin, and Christoph Cremer. Saturated patterned excitation microscopy—a concept for optical resolution improvement. *J. Opt. Soc. Am. A*, 19(8):1599–1609, Aug 2002.

[32] M. G. Gustafsson. Nonlinear structured-illumination microscopy: wide-field fluorescence imaging with theoretically unlimited resolution. *Proc Natl Acad Sci U S A*, 102(37):13081–6, 2005.

[33] Mark Bates, Bo Huang, MichaelJ. Rust, GrahamT. Dempsey, Wenqin Wang, and Xiaowei Zhuang. Sub-diffraction-limit imaging with stochastic optical reconstruction microscopy. In Astrid Graslund, Rudolf Rigler, and Jerker Widengren, editors, *Single Molecule Spectroscopy in Chemistry, Physics and Biology*, volume 96 of *Springer Series in Chemical Physics*, pages 399–415. Springer Berlin Heidelberg, 2010.

[34] Eric Betzig, George H. Patterson, Rachid Sougrat, O. Wolf Lindwasser, Scott Olenych, Juan S. Bonifacino, Michael W. Davidson, Jennifer Lippincott-Schwartz, and Harald F. Hess. Imaging intracellular fluorescent proteins at nanometer resolution. *Science*, 313(5793):1642–1645, 2006.

[35] S. T. Hess, T. P. Girirajan, and M. D. Mason. Ultra-high resolution imaging by fluorescence photoactivation localization microscopy. *Biophys J*, 91(11):4258–72, 2006.

[36] L. Schermelleh, R. Heintzmann, and H. Leonhardt. A guide to super-resolution fluorescence microscopy. *J Cell Biol*, 190(2):165–75, 2010.

[37] V. Westphal, S. O. Rizzoli, M. A. Lauterbach, D. Kamin, R. Jahn, and S. W. Hell. Video-rate far-field optical nanoscopy dissects synaptic vesicle movement. *Science*, 320(5873):246–249, 2008.

[38] Rainer Heintzmann and Christoph G. Cremer. Laterally modulated excitation microscopy: improvement of resolution by using a diffraction grating, 1999.

[39] M. G. Gustafsson. Surpassing the lateral resolution limit by a factor of two using structured illumination microscopy. *J Microsc*, 198(Pt 2):82–7, 2000.

[40] Stefan W. Hell. Increasing the resolution of far-field fluorescence light microscopy by point-spread-function engineering. *Topics In Fluorescence Spectroscopy*, 5, 1997.

[41] T. A. Klar, S. Jakobs, M. Dyba, A. Egner, and S. W. Hell. Fluorescence microscopy with diffraction resolution barrier broken by stimulated emission. *Proc Natl Acad Sci U S A*, 97(15):8206–10, 2000.

[42] V. Westphal and S. W. Hell. Nanoscale resolution in the focal plane of an optical microscope. *Physical Review Letters*, 94(14), 2005.

[43] M. Dyba and S. W. Hell. Focal spots of size lambda/23 open up far-field florescence microscopy at 33 nm axial resolution. *Physical Review Letters*, 88(16), 2002.

[44] G. Donnert, J. Keller, R. Medda, M. A. Andrei, S. O. Rizzoli, R. Lurmann, R. Jahn, C. Eggeling, and S. W. Hell. Macromolecular-scale resolution in biological fluorescence microscopy. *Proceedings of the National Academy of Sciences of the United States of America*, 103(31):11440–11445, 2006.

[45] B. Harke, J. Keller, C. K. Ullal, V. Westphal, A. Schoenle, and S. W. Hell. Resolution scaling in sted microscopy. *Optics Express*, 16(6):4154–4162, 2008.

[46] B. Harke, C. K. Ullal, J. Keller, and S. W. Hell. Three-dimensional nanoscopy of colloidal crystals. *Nano Letters*, 8(5):1309–1313, 2008.

[47] Marcel A. Lauterbach, Marc Guillon, Asma Soltani, and Valentina Emiliani. Sted microscope with spiral phase contrast. *Scientific Reports*, 3:–, 2013.

[48] V. Westphal, C. M. Blanca, M. Dyba, L. Kastrup, and S. W. Hell. Laser-diode-stimulated emission depletion microscopy. *Applied Physics Letters*, 82(18):3125–3127, 2003.

[49] Jinendra K. Ranka, Robert S. Windeler, and Andrew J. Stentz. Visible continuum generation in air-silica microstructure optical fibers with anomalous dispersion at 800 nm. *Opt. Lett.*, 25(1):25–27, Jan 2000.

[50] E. Auksorius, B. R. Boruah, C. Dunsby, P. M. P. Lanigan, G. Kennedy, M. A. A. Neil, and P. M. W. French. Stimulated emission depletion microscopy with a supercontinuum source and fluorescence lifetime imaging. *Optics Letters*, 33(2):113–115, 2008.

[51] E. Rittweger, B. R. Rankin, V. Westphal, and S. W. Hell. Fluorescence depletion mechanisms in super-resolving sted microscopy. *Chemical Physics Letters*, 442(4-6):483–487, 2007.

[52] D. Wildanger, E. Rittweger, L. Kastrup, and S. W. Hell. Sted microscopy with a supercontinuum laser source. *Optics Express*, 16(13):9614–9621, 2008.

[53] Michael D. Lesoine, Sayantan Bose, Jacob W. Petrich, and Emily A. Smith. Supercontinuum stimulated emission depletion fluorescence lifetime imaging. *The Journal of Physical Chemistry B*, 116(27):7821–7826, 2012.

[54] Johanna Bückers, Dominik Wildanger, Giuseppe Vicidomini, Lars Kastrup, and Stefan W. Hell. Simultaneous multi-lifetime multi-color sted imaging for colocalization analyses. *Opt. Express*, 19(4):3130–3143, Feb 2011.

[55] Silvia Galiani, Benjamin Harke, Giuseppe Vicidomini, Gabriele Lignani, Fabio Benfenati, Alberto Diaspro, and Paolo Bianchini. Strategies to maximize the performance of a sted microscope. *Opt. Express*, 20(7):7362–7374, Mar 2012.

[56] Susanne Schrof, Thorsten Staudt, Eva Rittweger, Nina Wittenmayer, Thomas Dresbach, Johann Engelhardt, and Stefan W. Hell. Sted nanoscopy with mass-produced laser diodes. *Opt. Express*, 19(9):8066–8072, Apr 2011.

[57] B. R. Rankin and S. W. Hell. Sted microscopy with a mhz pulsed stimulated-raman-scattering source. *Optics Express*, 17(18):15679–15684, 2009.

[58] G. Moneron, R. Medda, B. Hein, A. Giske, V. Westphal, and S. W. Hell. Fast sted microscopy with continuous wave fiber lasers. *Optics Express*, 18(2):1302–1309, 2010.

[59] K. I. Willig, B. Harke, R. Medda, and S. W. Hell. Sted microscopy with continuous wave beams. *Nature Methods*, 4(11):915–918, 2007.

[60] G. Moneron and S. W. Hell. Two-photon excitation sted microscopy. *Optics Express*, 17(17):14567–14573, 2009.

[61] Paolo Bianchini, Benjamin Harke, Silvia Galiani, Giuseppe Vicidomini, and Alberto Diaspro. Single-wavelength two-photon excitation - stimulated emission depletion (sw2pe-sted) superresolution imaging. *Proceedings of the National Academy of Sciences*, 109(17):6390–6393, 2012.

[62] Giuseppe Vicidomini, Gael Moneron, Kyu Y Han, Volker Westphal, Haisen Ta, Matthias Reuss, Johann Engelhardt, Christian Eggeling, and Stefan W Hell. Sharper low-power sted nanoscopy by time gating. *Nature Methods*, 8:571–573, 2011.

[63] Jeffrey R. Moffitt, Christian Osseforth, and Jens Michaelis. Time-gating improves the spatial resolution of sted microscopy. *Opt. Express*, 19(5):4242–4254, Feb 2011.

[64] Giuseppe Vicidomini and Gael Moneron. Gated sted microscopy with cw-sted lasers. Technical report, Leica Microsystems, 2012.

[65] A. Honigmann, C. Eggeling, M. Schulze, and A. Lepert. Super-resolution sted microscopy advances with yellow cw opsl. *Laser Focus World*, 48(1):75–79, 2012. cited By (since 1996)1.

[66] Giuseppe Vicidomini, Andreas Schonle, Haisen Ta, Kyu Young Han, Gael Moneron, Christian Eggeling, and Stefan W. Hell. Sted nanoscopy with time-gated detection: Theoretical and experimental aspects. *PLoS ONE*, 8(1):e54421, 01 2013.

[67] Giuseppe Vicidomini, Ivan Coto Hernandez, Marta d'Amora, Francesca Cella Zanacchi, Paolo Bianchini, and Alberto Diaspro. Gated cw-sted microscopy: A versatile tool for biological nanometer scale investigation. *Methods*, (0):–, 2013.

[68] E. Rittweger, K. Y. Han, S. E. Irvine, C. Eggeling, and S. W. Hell. Sted microscopy reveals crystal colour centres with nanometric resolution. *Nature Photonics*, 3(3):144–147, 2009.

[69] M. Dyba, S. Jakobs, and S. W. Hell. Immunofluorescence stimulated emission depletion microscopy. *Nature Biotechnology*, 21(11):1303–1304, 2003.

[70] V. Westphal, J. Seeger, T. Salditt, and S. W. Hell. Stimulated emission depletion microscopy on lithographic nanostructures. *Journal of Physics B-Atomic Molecular and Optical Physics*, 38(9):S695–S705, 2005.

[71] K. I. Willig, R. R. Kellner, R. Medda, B. Hein, S. Jakobs, and S. W. Hell. Nanoscale resolution in gfp-based microscopy. *Nature Methods*, 3(9):721–723, 2006.

[72] S. E. Irvine, T. Staudt, E. Rittweger, J. Engelhardt, and S. W. Hell. Direct light-driven modulation of luminescence from mn-doped znse quantum dots. *Angewandte Chemie-International Edition*, 47(14):2685–2688, 2008.

[73] R. Kasper, B. Harke, C. Forthmann, P. Tinnefeld, S. W. Hell, and M. Sauer. Single-molecule sted microscopy with photostable organic fluorophores. *Small*, 6(13):1379–1384, 2010.

[74] Nagaraj D. Halemani, Ioanna Bethani, Silvio O. Rizzoli, and Thorsten Lang. Structure and dynamics of a two-helix snare complex in live cells. *Traffic*, 11(3):394–404, 2010.

[75] Ulf Geumann, Christina Schafer, Dietmar Riedel, Reinhard Jahn, and Silvio O. Rizzoli. Synaptic membrane proteins form stable microdomains in early endosomes. *Microscopy Research and Technique*, 73(6):606–617, 2010.

[76] Harpreet Singh, Rong Lu, Pedro Felipe Gardeazabal Rodriguez, Yong Wu, Jean Chrisostome Bopassa, Enrico Stefani, and Ligia Toro. Visualization and quantification of cardiac mitochondrial protein clusters with {STED} microscopy. *Mitochondrion*, 12(2):230 – 236, 2012.

[77] C. A. Wurm, D. Neumann, R. Schmidt, A. Egner, and S. Jakobs. Sample preparation for sted microscopy. *Methods Mol Biol*, 591:185–99, 2010.

[78] B. Hein, K. I. Willig, and S. W. Hell. Stimulated emission depletion (sted) nanoscopy of a fluorescent protein-labeled organelle inside a living cell. *Proceedings of the National Academy of Sciences of the United States of America*, 105(38):14271–14276, 2008.

[79] Jorgen Kleine-Vehn, Krzysztof Wabnik, Alexandre Martiniere, Lukasz Langowski, Katrin Willig, Satoshi Naramoto, Johannes Leitner, Hirokazu Tanaka, Stefan Jakobs, Stephanie Robert, Christian Luschnig, Willy Govaerts, Stefan W. Hell, John Runions, and Friml Jiri. Recycling, clustering, and endocytosis jointly maintain pin auxin carrier polarity at the plasma membrane. *Molecular Systems Biology*, 7(1):–, 2011.

[80] C. Eggeling, C. Ringemann, R. Medda, G. Schwarzmann, K. Sandhoff, S. Polyakova, V. N. Belov, B. Hein, C. von Middendorff, A. Schonle, and S. W. Hell. Direct observation of the nanoscale dynamics of membrane lipids in a living cell. *Nature*, 457(7233):1159–U121, 2009.

[81] U. V. Nagerl, K. I. Willig, B. Hein, S. W. Hell, and T. Bonhoeffer. Live-cell imaging of dendritic spines by sted microscopy. *Proceedings of the National Academy of Sciences of the United States of America*, 105(48):18982–18987, 2008.

[82] James A. J. Fitzpatrick, Qi Yan, Jochen J. Sieber, Marcus Dyba, Ulf Schwarz, Chris Szent-Gyorgyi, Carol A. Woolford, Peter B. Berget, Alan S. Waggoner, and Marcel P. Bruchez. Sted nanoscopy in living cells using fluorogen activating proteins. *Bioconjugate Chemistry*, 20(10):1843–1847, 2009.

[83] Patrina A. Pellett, Xiaoli Sun, Travis J. Gould, James E. Rothman, Ming-Qun Xu, Ivan R. Corrêa, and Joerg Bewersdorf. Two-color sted microscopy in living cells. *Biomed. Opt. Express*, 2(8):2364–2371, Aug 2011.

[84] V. Westphal, M. A. Lauterbach, A. Di Nicola, and S. W. Hell. Dynamic far-field fluorescence nanoscopy. *New Journal of Physics*, 9, 2007.

[85] M. A. Lauterbach, J. Keller, A. Schonel, D. Kamin, V. Westphal, S. O. Rizzoli, and S. W. Hell. Comparing video-rate sted nanoscopy and confocal microscopy of living neurons. *Journal of Biophotonics*, 3(7):417–424, 2010.

[86] Sebastian Berning, Katrin I. Willig, Heinz Steffens, Payam Dibaj, and Stefan W Hell. Nanoscopy in a living mouse brain. *Science*, 335 (6068):551, 2012.

[87] Linjie Li, Rafael R. Gattass, Erez Gershgoren, Hana Hwang, and John T. Fourkas. Achieving ČÉ/20 resolution by one-color initiation and deactivation of polymerization. *Science*, 324(5929):910–913, 2009.

[88] Timothy F. Scott, Benjamin A. Kowalski, Amy C. Sullivan, Christopher N. Bowman, and Robert R. McLeod. Two-color single-photon photoinitiation and photoinhibition for subdiffraction photolithography. *Science*, 324(5929):913–917, 2009.

[89] Joachim Fischer and Martin Wegener. Three-dimensional direct laser writing inspired by stimulated-emission-depletion microscopy. *Opt. Mater. Express*, 1(4):614–624, Aug 2011.

[90] Joachim Fischer, Georg von Freymann, and Martin Wegener. The materials challenge in diffraction-unlimited direct-laser-writing optical lithography. *Advanced Materials*, 22(32):3578–3582, 2010.

[91] Joachim Fischer and Martin Wegener. Ultrafast polymerization inhibition by stimulated emission depletion for three-dimensional nanolithography. *Advanced Materials*, 24(10):OP65–OP69, 2012.

[92] Joachim Fischer and Martin Wegener. Three-dimensional optical laser lithography beyond the diffraction limit. *Laser & Photonics Reviews*, 7(1):22–44, 2013.

[93] Richard Wollhofen, Julia Katzmann, Calin Hrelescu, Jaroslaw Jacak, and Thomas A. Klar. 120 nm resolution and 55 nm structure size in sted-lithography. *Opt. Express*, 21(9):10831–10840, May 2013.

[94] Benjamin Harke, Paolo Bianchini, Fernando Brandi, and Alberto Diaspro. Photopolymerization inhibition dynamics for sub-diffraction direct laser writing lithography. *ChemPhysChem*, 13(6):1429–1434, 2012.

[95] Benjamin Harke, William Dallari, Giulia Grancini, Daniele Fazzi, Fernando Brandi, Annamaria Petrozza, and Alberto Diaspro. Polymerization inhibition by triplet state absorption for nanoscale lithography. *Advanced Materials*, 25(6):904–909, 2013.

[96] S. Chattopadhyay, Y.F. Huang, Y.J. Jen, A. Ganguly, K.H. Chen, and L.C. Chen. Anti-reflecting and photonic nanostructures. *Materials Science and Engineering: R: Reports*, 69:1–35, 2010.

[97] Fei Wang, HongYu Yu, Junshuai Li, Xiaowei Sun, Xincai Wang, and Hongyu Zheng. Optical absorption enhancement in nanopore textured-silicon thin film for photovoltaic application. *Opt. Lett.*, 35(1):40–42, Jan 2010.

[98] Hung-Chun Lo, Hsin-I Hsiung, Surojit Chattopadhyay, Hsieh-Cheng Han, Chia-Fu Chen, Jih Perng Leu, Kuei-Hsien Chen, and Li-Chyong Chen. Label free sub-picomole level {DNA} detection with ag nanoparticle decorated au nanotip arrays as surface enhanced raman spectroscopy platform. *Biosensors and Bioelectronics*, 26(5):2413 – 2418, 2011.

[99] Cees Dekker. Solid-state nanopores. *Nature Nanotechnology*, 2:209–215, 2007.

[100] Miao Yuqing, Chen Jianrong, and Fang Keming. New technology for the detection of ph. *Journal of Biochemical and Biophysical Methods*, 63(1):1 – 9, 2005.

[101] G. Donnert, J. Keller, C. A. Wurm, S. O. Rizzoli, V. Westphal, A. Schonle, R. Jahn, S. Jakobs, C. Eggeling, and S. W. Hell. Two-color far-field fluorescence nanoscopy. *Biophysical Journal*, 92(8):L67–L69, 2007.

[102] M. Dyba, J. Keller, and S. W. Hell. Phase filter enhanced sted-4pi fluorescence microscopy: theory and experiment. *New Journal of Physics*, 7, 2005.

[103] G. Donnert, C. Eggeling, and S. W. Hell. Major signal increase in fluorescence microscopy through dark-state relaxation. *Nature Methods*, 4(1):81–86, 2007.

[104] Marcel Leutenegger, Christian Eggeling, and Stefan W. Hell. Analytical description of sted microscopy performance. *Opt. Express*, 18(25):26417–26429, Dec 2010.

[105] C. Kuang, W. Zhao, and G. Wang. Far-field optical nanoscopy based on continuous wave laser stimulated emission depletion. *Rev Sci Instrum*, 81(5):053709, 2010.

[106] J. Kusba, V. Bogdanov, I. Gryczynski, and J. R. Lakowicz. Theory of light quenching: effects of fluorescence polarization, intensity, and anisotropy decays. *Biophys J*, 67(5):2024–40, 1994.

[107] E.J. Schimitschek, J.A. Trias, P.R. Hammond, and R.L. Atkins. Laser performance and stability of fluorinated coumarin dyes. *Optics Communications*, 11(4):352 – 355, 1974.

[108] Jose Portugal and Michael J. Waring. Assignment of dna binding sites for 4',6-diamidine-2-phenylindole and bisbenzimide (hoechst 33258). a comparative footprinting study. *Biochimica et Biophysica Acta (BBA) - Gene Structure and Expression*, 949(2):158 – 168, 1988.

[109] Mocharla R, Mocharla H, and Hodes ME. A novel, sensitive fluorometric staining technique for the detection of dna in rna preparations. *Nucleic Acids Res*, 15(24):10589–10589, December 1987.

[110] W. Sterzel, P. Bedford, and G. Eisenbrand. Automated determination of {DNA} using the fluorochrome hoechst 33258. *Analytical Biochemistry*, 147(2):462 – 467, 1985.

[111] Thomas R. Downs and William W. Wilfinger. Fluorometric quantification of {DNA} in cells and tissue. *Analytical Biochemistry*, 131(2):538 – 547, 1983.

[112] Roger V. Lebo. Chromosome sorting and dna sequence localization. *Cytometry*, 3 (3):145–154, 1982.

[113] Ali Hayek, Frederic Bolze, Jean-Francois Nicoud, Patrice L. Baldeck, and Yves Mely. Synthesis and characterization of water-soluble two-photon excited blue fluorescent chromophores for bioimaging. *Photochem. Photobiol. Sci.*, 5:102–106, 2006.

[114] Weihai Ying. Nad+ and nadh in cellular functions and cell death. *Front Biosci.*, 11:3129–48, 2006.

[115] Marina R. Kasimova, Jurgita Grigiene, Klaas Krab, Peter H. Hagedorn, Henrik Flyvbjerg, Peter E. Andersen, and Ian M. Moller. The free nadh concentration is kept constant in plant mitochondria under different metabolic conditions. *The Plant Cell Online*, 18(3):688–698, 2006.

[116] Melissa C. Skala, Kristin M. Riching, Annette Gendron-Fitzpatrick, Jens Eickhoff, Kevin W. Eliceiri, John G. White, and Nirmala Ramanujam. In vivo multiphoton microscopy of nadh and fad redox states, fluorescence lifetimes, and cellular morphology in precancerous epithelia. *Proceedings of the National Academy of Sciences*, 104(49):19494–19499, 2007.

[117] J R Lakowicz, H Szmacinski, K Nowaczyk, and M L Johnson. Fluorescence lifetime imaging of free and protein-bound nadh. *Proceedings of the National Academy of Sciences*, 89(4):1271–1275, 1992.

[118] L. Fulbert, J. Marty, B. Ferrand, and E. Molva. Passively q-switched monolithic microchip laser. *Proc. of Conference on Laser and Electro Optics*, 15:176, 1995.

[119] P. Torok and P.R.T. Munro. The use of gauss-laguerre vector beams in sted microscopy. *Optics Express*, Vol. 12:3605–361, 2004.

[120] M. Harris, C.A. Hill, and J.M. Vaughan. Optical helices and spiral interference fringes. *Optics Communications*, 106:161, 1994.

[121] E.G. Churin, J. Hossfeld, and T. Tschudi. Polarization configurations with singular point formed by computer generated holograms. *Optics Communications*, 99:13 – 17, 1993.

[122] Alicia V. Carpentier, Humberto Michinel, Jose R. Salgueiro, and David Olivieri. Making optical vortices with computer-generated holograms. *American Journal of Physics*, 76(10):916–921, 2008.

[123] Sharon A. Kennedy, Matthew J. Szabo, Hilary Teslow, James Z. Porterfield, and E. R. I. Abraham. Creation of laguerre-gaussian laser modes using diffractive optics. *Phys. Rev. A*, 66:043801, Oct 2002.

[124] Hsin-Yu Tsai, Henry I. Smith, and Rajesh Menon. Reduction of focal-spot size using dichromats in absorbance modulation. *Opt. Lett.*, 33(24):2916–2918, Dec 2008.

[125] Rajesh Menon, Paul Rogge, and Hsin-Yu Tsai. Design of diffractive lenses that generate optical nulls without phase singularities. *J. Opt. Soc. Am. A*, 26(2):297–304, Feb 2009.

[126] Nandor Bokor, Yoshinori Iketaki, Takeshi Watanabe, and Masaaki Fujii. Compact fluorescence depletion microscope system using an integrated optical element. *Optics Communications*, 281(7):1850 – 1854, 2008. Optics in Life Sciences.

[127] D. Wildanger, J. Buckers, V. Westphal, S. W. Hell, and L. Kastrup. A sted microscope aligned by design. *Opt Express*, 17(18):16100–10, 2009.

[128] S. Quabis, R. Dorn, and G. Leuchs. Generation of a radially polarized doughnut mode of high quality. *Applied Physics B*, 81(5):597–600, 2005.

[129] M. Reuss, J. Engelhardt, and S. W. Hell. Birefringent device converts a standard scanning microscope into a sted microscope that also maps molecular orientation. *Optics Express*, 18(2):1049–1058, 2010.

[130] James Pawley, editor. *Handbook of Biological Confocal Microscopy*. Springer, 2006.

[131] H. C. van de Hulst. *Light Scattering by Small Particles*. Dover Publications, 1981.

[132] Nadine Gröner, Jérémie Capoulade, Christoph Cremer, and Malte Wachsmuth. Measuring and imaging diffusion with multiple scan speed image correlation spectroscopy. *Opt. Express*, 18(20):21225–21237, Sep 2010.

[133] A Koltermann, U Kettling, J Bieschke, T Winkler, and M Eigen. Rapid assay processing by integration of dual-color fluorescence cross-correlation spectroscopy: high throughput screening for enzyme activity. *Proc Natl Acad Sci U S A*, 95(4):1421–1426–, February 1998.

[134] Kinjo MasataNa, Goro Nishimura, Tomiyasu Koyama, Ulo Mets, and Rudolf Rigler. Single-molecule analysis of restriction {DNA} fragments using fluorescence correlation spectroscopy. *Analytical Biochemistry*, 260(2):166 – 172, 1998.

[135] Rigler R Kinjo M. Ultrasensitive hybridization analysis using fluorescence correlation spectroscopy. *Nucleic Acids Res*, 23:1795–1799, 1995.

[136] Jonas Korlach, Petra Schwille, Watt W. Webb, and Gerald W. Feigenson. Characterization of lipid bilayer phases by confocal microscopy and fluorescence correlation spectroscopy. *Proceedings of the National Academy of Sciences*, 96(15):8461–8466, 1999.

[137] Petra Schwille, Jonas Korlach, and Watt W. Webb. Fluorescence correlation spectroscopy with single-molecule sensitivity on cell and model membranes. *Cytometry*, 36(3):176–182, 1999.

[138] S. R. Aragon and R. Pecora. Fluorescence correlation spectroscopy as a probe of molecular dynamics. *J. Chem. Phys.*, 64:1791–1803., 1976.

[139] L. Kastrup, H. Blom, C. Eggeling, and S. W. Hell. Fluorescence fluctuation spectroscopy in subdiffraction focal volumes. *Physical Review Letters*, 94(17), 2005.

[140] Jan Huisken, Jim Swoger, Filippo Del Bene, Joachim Wittbrodt, and Ernst H. K. Stelzer. Optical sectioning deep inside live embryos by selective plane illumination microscopy. *Science*, 305(5686):1007–1009, 2004.

[141] A. H. VOIE, D. H. BURNS, and F. A. SPELMAN. Orthogonal-plane fluorescence optical sectioning: Three-dimensional imaging of macroscopic biological specimens. *Journal of Microscopy*, 170(3):229–236, 1993.

[142] Christoph J. Engelbrecht and Ernst H. Stelzer. Resolution enhancement in a light-sheet-based microscope (spim). *Opt. Lett.*, 31(10):1477–1479, May 2006.

[143] Jim Swoger, Peter Verveer, Klaus Greger, Jan Huisken, and Ernst H. K. Stelzer. Multi-view image fusion improves resolution in three-dimensional microscopy. *Opt. Express*, 15(13):8029–8042, Jun 2007.

[144] Jeremie Capoulade, Malte Wachsmuth, Lars Hufnagel, and Michael Knop. Quantitative fluorescence imaging of protein diffusion and interaction in living cells. *Nature Biotechnology*, 29(9):835–839, 2011.

[145] Thorsten Wohland, Xianke Shi, Jagadish Sankaran, and Ernst H.K. Stelzer. Single plane illumination fluorescence correlation spectroscopy (spim-fcs) probes inhomogeneous three-dimensional environments. *Opt. Express*, 18(10):10627–10641, May 2010.

[146] Klaus Greger, Manuel J. Neetz, Emmanuel G. Reynaud, and Ernst H.K. Stelzer. Three-dimensional fluorescence lifetime imaging with a single plane illumination microscope provides an improved signal to noise ratio. *Opt. Express*, 19(21):20743–20750, Oct 2011.

[147] Mike Friedrich, Qiang Gan, Vladimir Ermolayev, and Gregory S. Harms. Sted-spim: Stimulated emission depletion improves sheet illumination microscopy resolution, April 2011.

[148] Werner Knebel and Wolfgang Oestreicher. Spim microscope with a sted light sheet, Apr 26, 2012.

[149] J. B. Ding, K. T. Takasaki, and B. L. Sabatini. Supraresolution imaging in brain slices using stimulated-emission depletion two-photon laser scanning microscopy. *Neuron*, 63(4):429–37, 2009.

[150] Qifeng Li, Sherry S.H. Wu, and Keng C. Chou. Subdiffraction-limit two-photon fluorescence microscopy for gfp-tagged cell imaging, December 2009.

[151] S. C. Baer. Single wavelength stimulated emission depletion microscopy. *US 20090121153 A1*, 2009.

[152] Michael Lesiecki and Federico Asmar. Photoproperties of dcm. *Journal of Luminescence*, 31-32:546–548, 1984.

[153] Teodora Scheul, Ciro D'Amico, Irène Wang, and Jean-Claude Vial. Two-photon excitation and stimulated emission depletion by a single wavelength. *Opt. Express*, 19(19):18036–18048, Sep 2011.

[154] R. J. Marsh, D. A. Armoogum, and A. J. Bain. Stimulated emission depletion of two-photon excited states. *Chemical Physics Letters*, 366(3-4):PII S0009–2614(02)01538–5, 2002.

[155] T. A. Klar, S. Jakobs, M. Dyba, A. Egner, and S. W. Hell. Fluorescence microscopy with diffraction resolution barrier broken by stimulated emission. *Proceedings of the National Academy of Sciences of the United States of America*, 97(15):8206–8210, 2000.

[156] D.J.S. Birch, G. Hungerford, R.E. Imhof, and A.S. Holmes. The fluorescence properties of {DCM}. *Chemical Physics Letters*, 178 (Issues 2-3):177 – 184, 1991.

[157] M. Meyer and J. C. Mialocq. Ground state and singlet excited state of laser dye dcm: dipole moments and solvent induced spectral shifts. *Optics Communications*, 64(3):264–8, 1987.

[158] Chris Xu and Watt W. Webb. Measurement of two-photon excitation cross sections of molecular fluorophores with data from 690 to 1050 nm. *JOSA B*, 13 (3):481–491, 1996.

[159] Rajeev Khare and Paritosh K. Shukla. *Coherence and Ultrashort Pulse Laser Emission*. InTech, 2010.

[160] O. Svelto. *Principles of lasers*. Springer, 1989.

[161] E Treacy. Optical pulse compression with diffraction gratings. *Quantum Electronics*, 5, Issue 9:454 – 458, 1969.

[162] Phillips D O'Connor DV, editor. *Time-correlated single-photon counting.* Academic Press, New York., 1984.

[163] Michael Wahl. Time-correlated single photon counting. Technical report, PicoQuant GmbH, 2009.

[164] J.M. Drake, Michael L. Lesiecki, and Donald M. Camaioni. Photophysics and cis-trans isomerization of {DCM}. *Chemical Physics Letters*, 113(6):530 – 534, 1985.

[165] J. P. Gordon, R. C. C. Leite, R. S. Moore, S. P. S. Porto, and J. R. Whinnery. Long-transient effects in lasers with inserted liquid samples. *Journal of Applied Physics*, 36(1):3–8, 1965.

[166] Marc Fischer and Chieu D. Tran. Thermal-lens-induced anomalous solvent's effect on fluorescence produced by two-photon continuous-wave laser excitation. *APPLIED OPTICS*, 39, Number 33:6257–6262, 2000.

[167] Ignacy Gryczynski, Valery Bogdanov, and JosephR. Lakowicz. Light quenching of tetraphenylbutadiene fluorescence observed during two-photon excitation. *Journal of Fluorescence*, 3(2):85–92, 1993.

[168] I. Gryczynski, V. Bogdanov, and J. R. Lakowicz. Light quenching and depolarization of fluorescence observed with laser pulses. a new experimental opportunity in time-resolved fluorescence spectroscopy. *Biophys Chem*, 49(3):223–32, 1994.

[169] P.R. Hammond. Laser dye dcm, its spectral properties, synthesis and comparison with other dyes in the red. *Optics Communications*, 29, Issue 3:331–333, 1979.

[170] A. J. Bain, R. J. Marsh, D. A. Armoogum, O. Mongin, L. Porres, and M. Blanchard-Desce. Time-resolved stimulated emission depletion in two-photon excited states. *Biochem Soc Trans*, 31(Pt 5):1047–51, 2003.

[171] M. Dyba, T. A. Klar, S. Jakobs, and S. W. Hell. Ultrafast dynamics microscopy. *Applied Physics Letters*, 77(4):597–599, 2000.

[172] J. Keller, A. Schonle, and S. W. Hell. Efficient fluorescence inhibition patterns for resolft microscopy. *Optics Express*, 15(6):3361–3371, 2007.

[173] Quoc-Thang Nguyen, Jonathan Driscoll, Earl M. Dolnick, and David . Kleinfeld. *In Vivo Optical Imaging of Brain Function. 2nd edition*. CRC Press, 2009.

[174] Xiaohua Huang, Svetlana Neretina, and Mostafa A. El-Sayed. Gold nanorods: From synthesis and properties to biological and biomedical applications. *Advanced Materials*, 21 (48):4880–4910, 2009.

[175] M. Iosin, F. Toderas, P.L. Baldeck, and S. Astilean. Study of protein-gold nanoparticle conjugates by fluorescence and surface-enhanced raman scattering. *Journal of Molecular Structure*, 924-926:196–200, 2009.

[176] Ana M. Gabudean, Monica Focsan, and Simion Astilean. Gold nanorods performing as dual-modal nanoprobes via metal-enhanced fluorescence (mef) and surface-enhanced raman scattering (sers). *The Journal of Physical Chemistry C*, 116(22):12240–12249, 2012.

[177] X. Guo and A. Xia. Ultrafast excited states relaxation dynamics in solution investigated by stimulated emission from a styryl dye. *Journal of Luminescence*, 122-123:532–535, 2007.

[178] Kiryl D. Piatkevich, James Hulit, Oksana M. Subach, Bin Wu, Arian Abdulla, Jeffrey E. Segall, and Vladislav V. Verkhusha. Monomeric red fluorescent proteins with a large stokes shift. *Proceedings of the National Academy of Sciences*, 2010.

Acknowledgements

Je voulais remercie de tout mon coeur à mes directeurs de thèse, Irène Wang et Jean Claude-Vial, pour m'avoir donné la chance de faire cette thèse, pour leur disponibilité, leur implication, leur compréhension et pour me faire découvrir le monde fascinante de l'optique.
Merci beaucoup a mes amis : Rachel, Mathieu, Richard, Luca.
Un grand merci à Philippe que m'as beaucoup aide dans tous les domaines.
Merci à Patrice que a été un très bon directeur de stage de master et a Olivier qui m'as aide toujours avec les problèmes de chimie et avec de bonnes blagues.
Et un très grand merci a tout l'équipe MOTIV pour m'accueillir et pour la très bonne ambiance.

Multumesc...
Familiei mele care a fost tot timpul cu mine la bine si la greu
Lui Vlad care a suportat cu rabdare toate nebuniile mele si m-a sustinut in toata perioada
Si prietenilor dragi : Ancuta, Geta, Petruta, Flo, Ruxandra, Anca si Radu.